Coupled CFD and CSM Simulation of a Plate Fin Heat Exchanger

Determination of local and global effects due to dynamic operation.

by

Ahmed Ibrahim

in partial fulfilment of the requirements for the degree of Master of Science
in Mechanical Engineering
at the Delft University of Technology.

Student number: 4585356
Project Submitted May 1, 2019
Thesis Supervisors: Dr.-ir. Rene Pecnik, TU Delft
Dr.-Ing. Sebastian Ulmer, The Linde Group- Engineering Division
Dino Mehanovic, The Linde Group- Engineering Division

TU Delft Delft University of Technology

THE LINDE GROUP

Abstract

Heat exchangers of any kind are exposed to thermal loading which have the potential to cause severe stresses on the equipment. The magnitude of these loads are far more pronounced when temperature differences occur. These may be during plant start-up or shut-down due to the transient nature of the temperature profiles or even imbalances that originate from improper steady-state operation. Failure of the heat exchanger may cause the complete shut-down of a plant depending on the service provided by the heat exchanger. For this reason it is of great importance that the location and magnitudes of these stresses are investigated such that both manufacturing methods and operation of the equipment can be optimised thus preventing failures. In an effort to investigate the structural integrity of the heat exchanger this thesis develops a workflow in which a computational fluid dynamics (CFD) solver is coupled with a computational structural mechanics (CSM) solver in order to identify key stress regions. As a case study to trial this method a test-rig of a plate fin heat exchanger (PFHE) used to investigate typical stresses occurring in the main heat exchanger of air separation units (ASUs) manufactured by Linde has been selected.

In order to simulate two heat exchanger blocks in their entirety some additional modelling steps are included. In the CFD simulation use of porous media is made to provide a simplified representation of the fins. Similarly simple block structures are used in the CSM model whose material properties have been changed to mimic the behaviour of the fins. The thermal model gives promising results and shows good agreement to analytical solutions however experimental validation is still necessary. This work shows that the coupling of the two solvers is generally possible but can still be streamlined in some respect with data extraction from the CFD solver being relatively slow and the following mapping of the temperatures onto the CSM mesh and eventual solving of the structural mechanics left with room for improvement in terms of computational speeds. In terms of identifying key stress regions the results indicate elevated stresses occurring at the weld which connects the two heat exchanger modules.

Secondarily to the large scale model a submodel was developed, depicting the perforated fin type. This task served as a proof of concept to gain a better understanding of local thermo-hydraulic phenomena especially to what extent perforation played a role in local heat transfer coefficients since such variables cannot be monitored in the large scale model. From the sub-model it was found that the perforations play a significant role in the heat transfer ability of the fin and local heat transfer coefficients in close proximity to the perforations were more than double the value of the average heat transfer coefficient observed in the bulk flow.

Acknowledgements

I would like to take this opportunity to show my gratitude to the individuals who have helped realize this work and provided support when needed. First and foremost I would like to thank my supervisor at Linde, Dr. Sebastian Ulmer for giving me the opportunity to join the department and work on this project. As well as taking out the time to check up on my progress on a weekly basis and giving constructive criticism when needed, especially in the CFD aspects of this work. Next I would like to give thanks to Dino Mehanovic who made himself available whenever I had questions regarding the FEM segment of the work. Additionally my thanks go to Manuel Knaup for taking out time from his schedule to indulge in the spontaneous discussions about my work and always provided a second opinion. I also wish to show appreciation in general to the department of Equipment process design and computational mechanics for making these past months fly by and generally providing an extremely pleasant environment to work in. At TU Delft I would like to thank my supervisor Dr. Rene Pecnik who enabled me to organize this thesis in industry and declared himself ready to supervise my work. Last but not least I am forever grateful to my family especially my mother and father who have instilled within me the importance of education from an early age and have cultivated my love for learning. My siblings Adam and Camilla as well as the many friends I have made during my travels who could always be relied on to put a smile on my face even during the hardest of times and for this I am deeply grateful.

Ahmed Ibrahim
Munich, May 2019

Contents

Nomenclature

Acronyms

ASU	Air Seperation Unit
CFD	Computational Fluid Dynamics
CHT	Conjugate Heat Transfer
CSM	Computational Structural Mechanics
CW	Common Wall
DNS	Direct Numerical Simulation
FE	Finite Element
FEA	Finite Element Analysis
FEM	Finite Element Method
FSI	Fluid Structure Interaction
FVM	Finite Volume Method
HTC	Heat Transfer Coefficient
LES	Large Eddy Simulation
NTU	Number of Transfer Units
NWM	Near Wall Modelling
NWR	Near Wall Resolution
PDE	Partial Differential Equation
PFHE	Plate Fin Heat Exchanger
RANS	Reynolds Averaged Navier Stokes
SST	Shear Stress Transport
URANS	Unsteady Reynolds Averaged Navier Stokes
VLES	Very Large Eddy Simulation
WALE	Wall-Adapting Eddy Viscosity

Latin Symbols

A	Area [m^2]
A_α	Contact area [m^2]
A_{fs}	Interfacial area density [$1/m$]
C	Heat capacity [J/K]
C_1	Linear Darcy-Forchheimer constant [$kg/m^2 s$]
C_2	Quadratic Darcy-Forchheimer constant [kg/m^4]
C_{ijkl}	Elastic modulus tensor [Pa]
E	Specific total energy /Youngs Modulus [J/kg] / [Pa]
F_{ij}	Deformation gradient tensor [-]
F_i	Force vector [N]
I	Second Moment of Inertia [kgm^2]
J_{ij}	Jacobian [-]
K	Stiffness [N/m]
K_{aibk}	Stiffness matrix [N/m]
K_{loss}	Quadratic loss coefficient [-]
K_{perm}	Specific permeability [-]
M	Moment due to real load [Nm]
$N^a(x_i)$	Interpolation function [-]
P_k	Production of turbulent kinetic energy [m^2/s^3]
Q_v'''	Volumetric heat source [W]
R	Specific gas constant [$J/molK$]
S_E	Energy Source [J]
S_M	Momentum source [kgm/s]
S_{ij}	Fist Pioloa-Kirchhoff stress tensor [Pa]
T	Temperature [K]
T_b	Bulk temperature [K]
T_{nw}	Near wall tempertaure [K]
T_s	Surface temperature [K]
T_w	Wall temperature [K]
T_{ij}	Stress tensor [Pa]
V	Volume [m^3]
W	Work done [J]
$W_{External}$	External work done [J]

$W_{Internal}$	Internal work done [J]
$\dot{Q}$	Heat flow [W]
$\dot{m}$	Mass flow rate [kg/s]
$\tilde{L}$	Characteristic Length Scale [m]
b_i	Body force vector [N]
c_F	drag constant [-]
c_μ	$k-\epsilon$ model constant [-]
c_p	Isobaric specific heat capacity [J/kgK]
$c_{1\epsilon}$	$k-\epsilon$ model constant [-]
$c_{2\epsilon}$	$k-\epsilon$ model constant [-]
d_h	Hydraulic diameter [m]
e	Specific internal energy [J]
f	Fanning friction factor [-]
f_K	Friction factor [-]
g	Gravitational acceleration [m/s^2]
h	Specific enthalpy [J/kg]
h_c	Convective heat transfer coefficient [W/m^2K]
j	Colburn factor [-]
k	Turbulent kinetic energy [m^2/s^2]
$k_{filtered}$	Turbulent kinetic energy from filtered Navier-Stokes equation [m^2/s^2]
$k_{residual}$	Turbulent kinetic energy from subgrid-stress model [m^2/s^2]
l	Length [m]
m	Moment due to virtual load [Nm]
p	Pressure [Pa]
q	Heat flux [W/m^2]
q_w	Wall heat flux [W/m^2]
r	Radius [m]
s_i	Displacement vector [m]
t	Time [s]
t_j	Traction force vector [N]
u	Velocity [m/s]
w	Weighting function [-]
y^+	Dimensionless wall distance [-]

Greek Symbols

Φ	Mass flux [kg/sm^2]
Σ_{ij}	Second-Piola Kirchhoff tensor [Pa]
α	Thermal diffusivity / Coefficient of thermal expansion [m^2/s] / [$1/K$]
δ_{ij}	Identity matrix [-]
ϵ	Turbulent dissapation rate / Effectiveness (NTU-Method) [m^2/s^3] / [-]
$\epsilon_{E,ij}$	Eulerian strain tensor [-]
$\epsilon_{L,ij}$	Lagrange strain tensor [-]
ϵ_{ij}	Infintesimal strain tensor [-]
γ	Vapour fraction [-]
λ	Thermal conductivity [W/mk]
μ	Dynamic viscosity [Pas]
∇	Gradient operator [$1/m$]
∇^2	Laplacian operator [$1/m^2$]
ν	Kinematic viscosity/Poissons ratio [m^2/s] / [-]
ν_t	Eddy viscosity [m^2/s]
ν_θ	Turbulent diffusion coefficient for heat transfer [m^2/s]
ω	Vorticity / Specific dissipation rate [rad/s] / [$1/s$]
ϕ	Porosity [-]
ϕ_s	Porosity(solid fraction) [-]
ρ	Density [kg/m^3]
σ_ϵ	$k-\epsilon$ model constant [-]
σ_{ij}	Cauchy stress tensor [Pa]
σ_k	$k-\epsilon$ model constant [-]
τ_{ij}	Kirchhoff stress tensor / Deviatoric stress tensor [Pa]
τ_{sgs}	Subgrid stress [Pa]
$\tilde{\mu}$	Effective viscosity [Pas]
ζ	Dimensionless length scale [-]

Dimensionless Groups

Cr	Courant number
Cr_t	Thermal Courant number
Nu	Nusselt number
Pr	Prandtl number
Re	Reynolds number

List of Figures

List of Tables

1 Introduction

1.1. Background

Heat exchangers play a significant role in many segments of industry including but not limited to space-heating, air-conditioning, power production, waste heat recovery and chemical processing as outlined in Incropera et al. [24]. Depending on the use there are a variety of heat exchangers such as plate fin, shell and tube as well as coil wound heat exchangers to name but a few. Despite the variety in this equipment they do have one thing in common and that is that they could experience severe thermal loading. These thermal loads, particularly during the start-up and shut-down of the apparatus are highly transient. The thermal loading endured by the equipment during this phase is likely to cause the formation of stress regions leading to failure of the heat exchanger after a sufficient number of cycles. The main task of this thesis is to develop a coupled workflow which incorporates computational fluid dynamics (CFD) and computational structural mechanics (CSM) in order to investigate the structural integrity of a heat exchanger during such a transient operation.

For the purpose of this work a test rig of a plate fin heat exchanger (PFHE) used to investigate typical stresses in the main heat exchanger used in air separation units (ASUs) has been nominated to trial this workflow. Specifically this PFHE is to be used in the flexible operation of ASUs. Meaning that the PFHE will have to adapt and synchronize to renewable energy. Thus quick startup of the apparatus is expected in order to take advantage of renewable energy sources when available. As well as a timely shutdown so as to avoid the cost of the more expensive, traditional energy sources. This trial case is based on current work produced by Linde in cooperation with the German ministry of research and education, for more information regarding the origins of this project reference can be made to BMBF [8] and BMBF [7] specifically the project entitled *SynErgie*.

As mentioned previously the driving force behind this project is the flexible operation of Air separation units (ASUs) constructed by Linde. ASUs separate air into its major components, namely nitrogen, oxygen, and noble gases (mainly argon). They serve as an ideal starting point due to their high energy demand, widespread application and high-density storage capacity see Haider et al. [18]. ASUs are typically designed for steady-state, continuous production however with the emphasis on renewable energy sources growing these process will need to adapt and accommodate load flexibility in order to take advantage of the fluctuating energy supply of solar and/or wind. In general the central component of ASUs are the rectification columns used for the cryogenic separation of air, however for the high process integration the main heat exchanger has been identified as a key unit for the dynamic behaviour of the plant. Thus the current work investigates two specific areas regarding the heat exchanger. Firstly due to the transient operating conditions like start-up and shut-down the aluminium brazed plate fin heat exchanger (PFHE) is prone to undergo thermal stresses due to the rapid changes in process flow rates and temperatures. To investigate the global stresses a one-way fluid-structure interaction (FSI) simulation is set up thermohydraulic behaviour in full 3-D resolution is modelled using a CFD solver and the data is transferred to a finite element mesh and stresses are computed in the computational structural mechanics (CSM) solver. The structural mechanics model for the PFHE is based on the work by Hölzl [20], who's methodology has already been applied to small PFHE test units as seen in

the work by Hölzl and Flüggen [21] to determine where the peak stresses occur in PFHEs. While the main focus of the project lies in the determination of thermal stresses a secondary objective is defined to better understand local thermohydraulic phenomena. For this a submodel of a fin type (specifically the perforated fins) within the PFHE was built and investigated.

1.2. Research Questions

In an effort to better define the scope of this project some of the key research questions which are hoped to be at least partially answered are listed here.

Regarding the large scale geometry

- *To what extent can 3-D temperatures be mapped onto a FEM mesh in a one-way FSI simulation framework? Is this workflow viable?*

- *To what extent can porous media be used to reflect thermohydraulic phenomena of detailed geometry?*

- *What are the deformations and resulting locations of the peak stresses?*

Regarding the Fin submodel

- *What is the impact of the perforated geometry on the fluid flow?*

- *To what extent is the temperature profile symmetric across the fin channels?*

- *How do the local heat transfer coefficients behave qualitatively?*

- *What role can CFD play in the development of correlations for different fin type?*

1.3. Thesis Structure

To assist in navigating this work a brief outline of following chapters is given. Chapter 2 provides a description of the theoretical background to this work. Specifically this includes a discussion of the governing equations of fluid and solid mechanics, rounded off with the highlighting the various ways to perform fluid structure interaction simulation. Including examples from industry and academia which implement these state of the art approaches. Chapter 3 describes the simulation setup of the large scale model of the PFHE, including discussion of how porous media was used to model the detailed fin geometry concluding with the presentation of the results from the thermohydraulic and mechanical simulations. Chapter 4 focuses on the secondary objective of this thesis and will describe the model setup of the perforated fin submodel used in determining local thermohydraulic behaviour. Finally chapter 5 concludes the work by attempting to answer at least partially some the research questions posed earlier, as well as a summary of potential further work in this field.

2

Theoretical Background

This chapter provides background with regards to the theoretical concepts that are used in this work. Firstly the computational fluid dynamics (CFD) aspect of a conjugate heat transfer problem will be outlined which includes expressing the relevant mechanisms of heat transfer as well as the conservation equations of fluid dynamics. Additionally a general description of the finite volume method (FVM) used in the discritisation of the governing equations in the CFD solver is provided. The second part deals with the computational structural mechanics (CSM) components. For this the governing equations of solid mechanics will be introduced and how these are applied in a finite element method computation. The final part discusses the different types of coupling procedure with reference to examples from both industry and academia.

2.1. Fluid Dynamic Simulation

This section will outline the fluid dynamics simulation part of the project. This includes an explanation of conjugate heat transfer, which will cover the relevant mechanisms of heat transfer. The governing equation of fluid dynamics will also be covered, including a brief explanation of turbulence modelling, concluding with the FVM used by the CFD solver.

2.1.1. Modes of heat transfer

Mills [36] defines heat as the energy transfer due to temperature gradients or differences. The mechanisms by which energy is transferred via heat is conduction, convection and radiation. Due to the heat transfer in heat exchangers being dominated by conduction and convection this thesis will forgo any detailed explanation of radiative heat transfer.

Heat conduction

On a microscopic level conduction encompasses varied phenomena such as molecular collision in gasses, lattice vibrations in crystals and flow of electrons in metals [36]. When considering the phenomenological laws at the macroscopic level these are described by Fourier's law of heat conduction. This states that in a homogeneous substance, the local heat flux is proportional to the negative of the local temperature gradient as described in equation 2.1.

$$q = -\lambda \nabla T \tag{2.1}$$

Where q is the heat flux, T is the local temperature and ∇ refers to the gradient operator. Finally λ is the constant of proportionality referred to as the thermal conductivity of the material with the negative sign indicating that q moves in the direction of the lower temperature.

Heat convection

A fluid, by virtue of its mass and velocity, can transport momentum by extension then by virtue of its temperature, it can transport energy [36]. Heat convection is the term used to describe heat transfer of a moving fluid. In general convective heat transfer may be driven by two processes. One being *natural*

convection in which the flow is driven by buoyancy forces arising from density variations and the impact of body forces on the flow, usually in the form of gravity. The other form being forced convection which occurs when fluid flow is forced for instance by a liquid pump or air on a flight vehicle propelled through the atmosphere. Furthermore either *natural* or *forced* convection can be laminar or turbulent where the flow regime is judged based on the dimensionless group called the Reynolds number (*Re*) defined in equation 2.2.

$$Re = \frac{\rho u d_h}{\mu} \tag{2.2}$$

Where ρ, u, μ are the density, velocity and dynamic viscosity of the fluid respectively and d_h is the hydraulic diameter. Pipe flow is considered to be turbulent when *Re* exceeds 2300.

To this end the rate of heat transfer by convection is usually a complicated function of surface geometry, the fluid temperature and velocity as well as the fluid physical properties. An attempt is made to describe this type of heat transfer using another constant of proportionality called the convective heat transfer coefficient h_c used in equation 2.3.

$$q_s = h_c \Delta T \tag{2.3}$$

Where q_s is the heat flux from the surface to the fluid and for internal flow $\Delta T = T_s - T_b$ where T_s is the surface temperature and T_b is the averaged fluid temperature also known as the bulk temperature.

2.1.2. Governing equations: Fluid solver

This section will define the partial differential equations used in the thermohydraulic modelling of the fluid flow as well as the heat transfer in the solid.

Governing equation for the solid

Heat transfer in the solid will be governing by the heat conduction equation defined in equation 2.4.

$$\rho c_p \frac{\partial T}{\partial t} = \lambda \nabla^2 T + \dot{Q}_V''' \tag{2.4}$$

Where ρ is the density, c_p is the isobaric specific heat capacity, λ is the thermal conductivity, $\dot{Q}_v'''$ is a volumetric heat source, T is the local temperature and ∇^2 being the Laplace operator defined in Cartesian coordinates in equation 2.5

$$\nabla^2 = \frac{\partial^2}{\partial x^2} + \frac{\partial^2}{\partial y^2} + \frac{\partial^2}{\partial z^2} \tag{2.5}$$

Governing equations for the fluid

The Navier-Stokes equations are the partial differential equations (PDEs) used to model fluid dynamics, they consist of the continuity equation, the momentum equations and the energy equation which are taken from Kundu et al. [28] in their derivative forms in equations 2.6, 2.7 and 2.8 respectively. The equations have been written using Einstein notation which enables to write the governing equations more precisely by implying summation over the index. As a demonstration the conservation of mass is written in both the shorthand, Einstein summation convention and fully in its individual components.

$$\underbrace{\frac{\partial \rho}{\partial t} + \frac{\partial}{\partial x_i}(\rho u_i)}_{\text{Einstein notation}} = \underbrace{\frac{\partial \rho}{\partial t} + \frac{\partial}{\partial x}(\rho u) + \frac{\partial}{\partial y}(\rho v) + \frac{\partial}{\partial z}(\rho w) = 0}_{\text{Written out fully}} \tag{2.6}$$

$$\frac{\partial}{\partial t}(\rho u_i) + \frac{\partial}{\partial x_j}(\rho u_i u_j) = \rho g_i + \frac{\partial}{\partial x_j}(T_{ij}) \tag{2.7}$$

$$\frac{\partial}{\partial t}(\rho E) + \frac{\partial}{\partial x_i}(\rho E u_i) = \rho g_i u_i + \frac{\partial}{\partial x_i}(T_{ij} u_j) - \frac{\partial q_i}{\partial x_i} \tag{2.8}$$

Where

- ρ is the density
- u is the velocity
- p is the pressure
- g is the body acceleration term (gravity)
- T_{ij} is the stress tensor.
- E is the specific total energy
- q is the heat flux

The governing equations have been written in terms of the stress tensor T_{ij} which is a symmetric tensor made up of the static stress and the dynamic stresses from fluid motion as seen in equation 2.9

$$T_{ij} = -p\delta_{ij} + \tau_{ij} \tag{2.9}$$

where p is the pressure and δ_{ij} denotes the identity matrix. The second term is the *deviatoric stress tensor* and defines dynamic stresses based on the fluid motion. The stress tensor, assuming incompressibility is written out completely in 2.10.

$$T_{ij} = \begin{bmatrix} -p + \frac{\partial u}{\partial x} & \frac{1}{2}\left(\frac{\partial u}{\partial y} + \frac{\partial v}{\partial x}\right) & \frac{1}{2}\left(\frac{\partial u}{\partial z} + \frac{\partial w}{\partial x}\right) \\ \frac{1}{2}\left(\frac{\partial v}{\partial x} + \frac{\partial u}{\partial y}\right) & -p + \frac{\partial v}{\partial y} & \frac{1}{2}\left(\frac{\partial v}{\partial z} + \frac{\partial w}{\partial y}\right) \\ \frac{1}{2}\left(\frac{\partial w}{\partial x} + \frac{\partial u}{\partial z}\right) & \frac{1}{2}\left(\frac{\partial w}{\partial y} + \frac{\partial v}{\partial z}\right) & -p + \frac{\partial w}{\partial z} \end{bmatrix} \tag{2.10}$$

Assuming the flow is incompressible and thus the density of the fluid remains constant the energy equation is solved independently while a *coupled* algorithm is used for mass and momentum equations. For compressible flow however the energy equation must be solved with the mass and momentum equations, with the temperature distribution being obtained by plugging in velocity and pressure values in the energy equation. Recall the specific total energy term E in the energy equation, this term can be written as the specific internal energy as seen in equation 2.11

$$E = e + \frac{1}{2}u_i^2 \tag{2.11}$$

where e is the specific internal energy. Furthermore enthalpy can be written in terms of internal energy and kinematic pressure as in equation 2.12.

$$h = e + \frac{p}{\rho} \tag{2.12}$$

where the specific enthalpy is generally expressed in terms of temperature and the specific heat capacity as in equation 2.13.

$$h = c_p T \tag{2.13}$$

Since density is no longer assumed constant there are a total of six unknowns (velocity(*u, v and w*), pressure, temperature and density), and currently only five equations (mass, momentum (*x, y, z*) and energy). For this reason an additional equation is introduced, in the form of the equation of state which defines a relationship between density, pressure and temperature. There exist a variety of such equations of state the most common being the ideal gas law seen in equation 2.14.

$$p = \rho R T \tag{2.14}$$

where R is the specific gas constant.

2.1.3. Turbulence modelling

In order to more effectively resolve the finer details of a flow it is important to dedicate resources to model the turbulent effects that may occur. Flows that exhibit chaotic behaviour are categorized as turbulent. Figure 2.1a shows smoke wires flow through the square perforations of a plate. On the left the flow exhibits laminar behaviour, however as the flow moves past through the holes the laminar flow begins to form eddies until the flow becomes fully turbulent, downstream. From a statistical point of view reference can be made to figure 2.1b. This represents the axial component of velocity in a turbulent jet. The graph contains the hallmark indicative of turbulence, namely the large fluctuations represented by the spikes in the graph that deviate by a about 25% form the mean velocity which is represented by the straight, horizontal line.

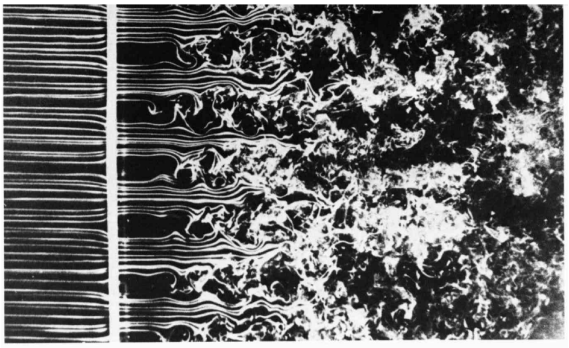

(a) Generation of turbulence, as laminar smoke wires pass through square perforations. Image courtesy of Van Dyke [52].

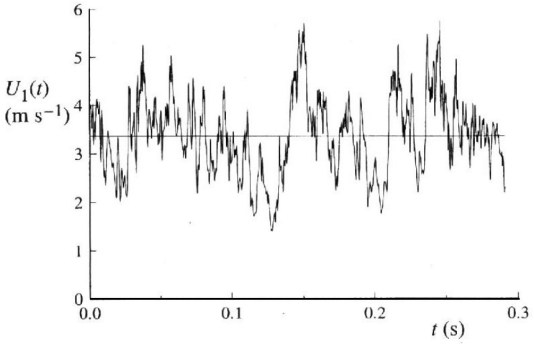

(b) Time history of the axial component of velocity on the centreline of a turbulent jet [42].

Turbulent phenomena may have a significant effect on conjugate heat transfer (CHT) particularly on the convective part. This section is therefore dedicated to introduce turbulence modelling and will more specifically describe the models used in this work namely the Reynold averaged Navier-Stokes (RANS) models and large eddy simulation (LES).

Reynolds averaged Navier-Stokes (RANS)

RANS models aim at to solve the Reynolds equations for the mean velocity field Pope [42]. In order to get to the Reynold equations one must perform some mathematical operations on the Navier-Stokes equations presented previously in 2.6, 2.7 and 2.8. These include the decomposition of instantaneous quantities such as velocity pressure and temperature in terms of an average and a fluctuating term. Taking an ensemble average of the entire equations whilst also assuming incompressibility such that the continuity equation is simplified accordingly. For details regarding the derivation of these equations any textbook on turbulence may be consulted such as Nieuwstadt et al. [40], Bailly [5] or the afore mentioned Pope [42]. Once the previously mentioned steps are are undergone one is left with the Reynold equations as seen in equations 2.15, 2.16 and 2.17 where use of the Einstein notation is again made for simplicity.

$$\frac{\partial \overline{u_i}}{\partial x_i} = 0, \tag{2.15}$$

$$\frac{\partial \overline{u_i}}{\partial t} + \frac{\partial \overline{u_i u_j}}{\partial x_j} = -\frac{1}{\rho_0}\frac{\partial \overline{p}}{\partial x_j} + \nu \frac{\partial^2 \overline{u_i}}{\partial x_j^2} - \underbrace{\frac{\partial \overline{u_i' u_j'}}{\partial x_j}}_{\text{Reynolds Stress}} \tag{2.16}$$

$$\frac{\partial \overline{T}}{\partial t} + \overline{u_j}\frac{\partial \overline{T}}{\partial x_j} = \kappa \frac{\partial^2 \overline{T}}{\partial x_j^2} - \underbrace{\frac{\partial \overline{u_j' T'}}{\partial x_j}}_{\text{Reynolds Stress}} \tag{2.17}$$

When comparing equations 2.16 and 2.17 to the original momentum and energy equations shown in equations 2.7 and 2.8 one can see that some additional terms have appeared. Namely $\overline{u_i' u_j'}$ and $\overline{u_j' \theta'}$ defined as the Reynolds stress terms that appear from the non-linear convective terms in the original Navier-Stokes equations. The new terms cause the number of unknowns to exceeded the number of equations leading to what is termed a *closure problem*. In order to determine a solution to this a further relation must be introduced into the current set of equations. This relation originates from the fact that for a Newtonian fluid the stress is directly proportional to the strain rate with the constant of proportionality being the fluid viscosity. Assuming homogeneous, isotropic turbulence the turbulent stress tensor is proportional to the turbulent strain rate using a *turbulent viscosity* as seen in equation 2.18 with ν_t being the turbulent viscosity.

$$\rho\left(-\overline{u_i' u_j'} + \frac{1}{3}\overline{u_k'^2}\delta_{ij} \right) = \rho_0 \nu_t \left(\frac{\partial \overline{u_i}}{\partial x_j} + \frac{\partial \overline{u_j}}{\partial x_i} \right) \tag{2.18}$$

Similarly for the turbulent temperature flux

$$-\overline{u_j' \theta'} = \nu_\theta \frac{\partial \overline{\theta}}{\partial x_i} \tag{2.19}$$

Where ν_θ is the turbulent diffusion coefficient for heat transfer. Equations 2.18 and 2.19 are known as the Boussinesq closure hypothesis and are the relations used to close for the unknown Reynolds stresses. How ν_t and ν_θ are defined is dependent on which model is used. RANS models are classified as two equation models since they describe turbulence using two additional transport equations. By this approach turbulent flows are much better represented compared to the more simple one-equation model such as the Prandlt model. For the purposes of giving a brief overview of RANS modelling the k-ϵ model will be used.

In the $k-\epsilon$ model turbulent kinetic energy (k) and dissipation rate of turbulent kinetic energy (ϵ) are used in equation 2.20 to model the turbulent viscosity. Moreover the two equations for turbulent kinetic energy and dissipation rate are obtained from the RANS equations and are presented in equations 2.21 and 2.22 respectively.

$$\nu_t = c_\mu \frac{k^2}{\epsilon} \tag{2.20}$$

$$\frac{Dk}{Dt} = P_k + \frac{\partial}{\partial x_j}\left(\frac{\nu_t}{\sigma_k} \frac{\partial k}{\partial x_j} \right) - \epsilon \tag{2.21}$$

$$\frac{D\epsilon}{Dt} = \frac{\partial}{\partial x_j}\left(\frac{\nu_t}{\sigma_\epsilon} \frac{\partial \epsilon}{\partial x_j} \right) + \frac{\epsilon}{k}(c_{1\epsilon} P - c_{2\epsilon}\epsilon) \tag{2.22}$$

These three equations build up the entirety of the $k-\epsilon$ model and in combination with the RANS equation 2.16 and the closure hypothesis from equation 2.18 provide a closed set of equations. Where c_μ ,σ_k, σ_ϵ, $c_{1\epsilon}$ and c_{2_ϵ} are model constants that may be varied to satisfy some types of turbulent flows. Finally P_k represents the production of turbulent kinetic energy defined in equation 2.23 For detailed derivation of the k- and ϵ- equations the work by Nieuwstadt et al. [40] can be referenced and will therefore not be explained here, suffice it to say that the k-equation can be obtained from the momentum equation since $k = \frac{1}{2}\overline{u_i'^2}$. Moreover for the ϵ-equation use of another quantity *enstrophy* is made which is a function of the vorticity of the flow such that $\epsilon = \nu\overline{\omega_i'^2}$.

$$P_k = -\overline{u_i' u_j'} \frac{\partial \overline{u_i}}{\partial x_j} \tag{2.23}$$

On a final note it should be mentioned that the $k-\epsilon$ model is only one of a variety of different RANS models that are available. A popular alternative is the $k-\omega$ which replaces the dissipation rate equation with the specific dissipation rate where ω in this particular case is the specific dissipation rate which has the dimensions of frequency. The $k-\omega$ model is a suitable modelling approach for boundary layer flows and is superior both in its treatment of the viscous near-wall region, and in it accounting for the

effects of the stream-wise pressure gradients [42]. However this model struggles in the treatment of non-turbulent free-stream boundaries. As a solution to this Pope [42] refers to alternative models which behave as a hybrid of the $k-\epsilon$ and $k-\omega$ models, this is done by implementing a blending factor that enables to vary between the two models depending on where the flow is being resolved. For a detailed derivation of the equations and constants used in this model the works by Bailly [5] is recommended.

Large eddy simulation (LES)
Alternatively to the RANS model presented previously a step towards a more detailed solution of turbulent phenomena will be obtained when applying what is known as a large eddy simulation (LES). In large-eddy simulation the larger three-dimensional unsteady turbulent motions are directly represented, whereas the effects of the smaller-scale motions are modelled. It is for this reason that LES is able to convey more information about a flow compared to the Reynolds-stress models since a larger proportion of the turbulent scales are simulated rather than modelled. What distinguishes a large-eddy simulation compared to a direct numerical simulation (DNS) is that in LES the governing equations are modified by applying a spatial filter to the mass, momentum and energy equations that determine which scales are simulated and which are modelled [5]. Due to this filtering process one is able to significantly reduce the computational cost. Setting up a large-eddy simulation generally consists of the following steps:

i. Defining of *filtering* operation, used to decompose velocity field $u_i(x_i,t)$ into the filtered component (resolved component) $[u_i](x_i,t)$ and a residual (subgrid-scale (SGS)) component $[u_i'](x_i,t)$. Where the filtered velocity field $[u_i](x_i,t)$ is three-dimensional and time-dependent, representing the motion of the large eddies.

ii. Derivation of the equations describing the evolution of the filtered velocity field from the Navier-Stokes equations. *Filtered* Navier-Stokes written as

$$\frac{\partial[u_i]}{\partial t}+\frac{\partial[u_iu_j]}{\partial x_j}=-\frac{\partial[p]}{\partial x_i}+\frac{\partial}{\partial x_j}\nu\left(\frac{[u_i]}{\partial x_j}+\frac{\partial[u_j]}{\partial x_i}\right) \tag{2.24}$$

This introduces an unknown quantity originating from the non-linear convective term in the original Navier-Stokes equation :$[u_iu_j]$. This term can be re-written in terms of subgrid-stresses as seen in equation 2.25.

$$[u_iu_j]=[u_i][u_j]+\underbrace{[u_iu_j]-[u_i][u_j]}_{\text{Subgrid stress}} \tag{2.25}$$

Thus in terms of subgrid stresses the filtered Navier-Stokes equations can be written as:

$$\frac{\partial[u_i]}{\partial t}+\frac{\partial[u_i][u_j]}{\partial x_j}=-\frac{1}{\rho_0}\frac{\partial[p]}{\partial x_j}+\frac{\partial}{\partial x_j}\nu\left(\frac{\partial[u_i]}{\partial x_j}+\frac{\partial[u_j]}{\partial x_i}\right)+\frac{1}{\rho_0}\frac{\partial\tau_{sgs}}{\partial x_j} \tag{2.26}$$

Where τ_{sgs} is the subgrid stress and is defined in equation 2.27.

$$\tau_{sgs}=\rho_0\Big([u_iu_j]-[u_i][u_j]\Big) \tag{2.27}$$

iii. Closure must now be obtained for the unknown residual-stress tensor, as described previously for RANS modelling. Here too this can most simply be done by an eddy-viscosity model as seen in equation 2.28.

$$\tau_{sgs}=K_s\left(\frac{\partial[u_i]}{\partial x_j}+\frac{\partial[u_j]}{\partial x_i}\right) \tag{2.28}$$

iv The final step consists of numerically solving the filtered equations for $[u_i(x_i,t)]$ which provide an approximation for the large-scale motions.

The outcome of the simulation depends on the mesh and what model is used to resolve the micro-scale. To this end there are a range of differing approaches to LES [42]. These varying degrees of accuracy are outlined in table 2.1.

Table 2.1: Summary of resolution in DNS and some variants of LES [42]

Model	*Acronym*	*Resolution*
Direct numerical simulation	DNS	Turbulent motions of all scales are fully resolved.
Large-eddy simulation with near-wall resolution	LES-NWR	The filter and grid are sufficently fine to resolve 80% of the energy everywhere.
Large-eddy simulation with near wall modelling	LES-NWM	The filter and grid are sufficiently fine to resolve 80% of the energy remote from the wall, but not in the near-wall region.
Very-large-eddy simulation	VLES	The filter and grid are too coarse to resolve 80% of the energy.

2.1.4. Finite volume method

Popular methods of solving PDEs numerically include the finite difference, finite element and finite volume methods. Typically CFD tools used in industry take advantage of the latter option. This section will only provide a brief overview of the finite volume method since this is a standard procedure and available in most literature on CFD.

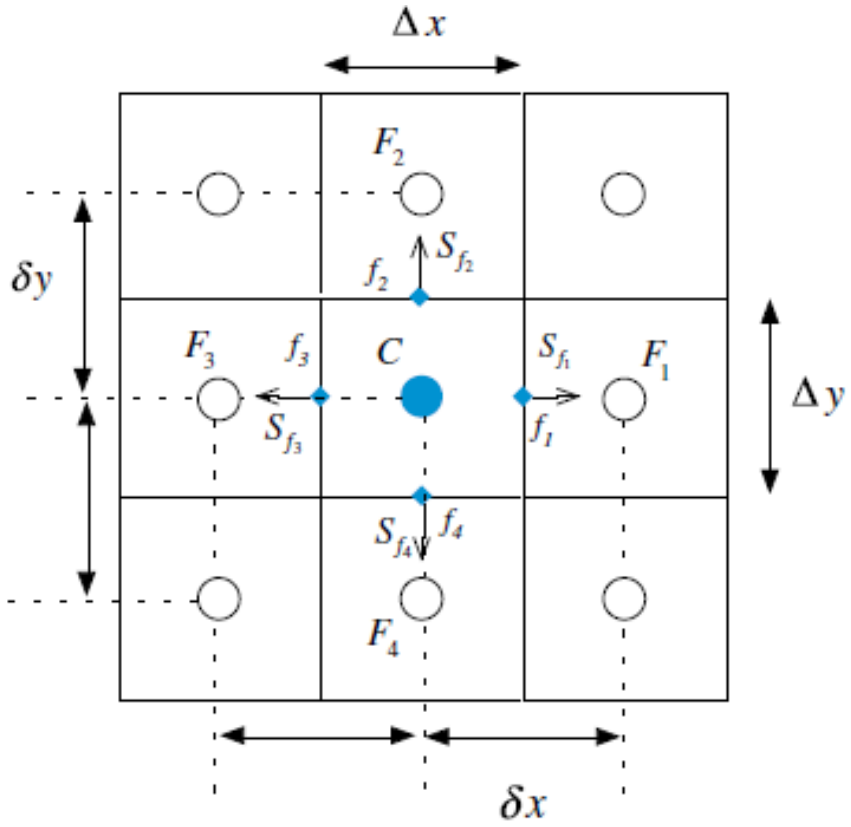

Figure 2.2: Finite Volume Grid Moukalled et al. [37].

Figure 2.2 represents an arbitrary grid with finite volume notation. In order to solve the PDEs governing fluid flow these equations are integrated over a control volume defined by each individual element in the computational domain. Through the use of divergence theorem these volume integral may be written in terms of surface integrals which are then replaced by a summation over the faces of the control volume. The surface fluxes are interpolated from the cell centroids as seen in figure 2.2. Continuing with this procedure for the neighbouring elements will result in the formation of linear sets of algebraic

equations which are then cast into a system of matrices and vectors that are solved using an iterative approach.

2.2. Structural Mechanics Simulation

The description of structural modelling follows a similar pattern to the previous section on the fluid model. First the governing equations of continuum mechanics are described which dictate the physics of deformations and the resulting stresses of solids. Finally a brief overview of the discritisation method for said governing equations will be addressed which pertains to the finite element method.

2.2.1. Governing equations: Solid solver

The following section will outline the governing equations of solid mechanics. Specifically this includes the equations used to describe the response of solids under mechanical or thermal loading. These responses are better understood by looking at the mathematical descriptions of shape changes in solids and the resulting internal forces. After that the equilibrium for deformable solids will be discussed including the principle of virtual work which is the cornerstone of Finite Element Analysis (FEA).

Shape changes in solids

In order to fundamentally define the shape change in a solid a displacement vector $s_i(x,t)$ describing the motion of each point in the solid must be specified. Take for instance the solid being deformed in figure 2.3.

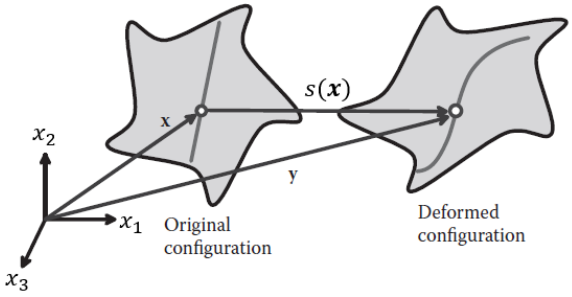

Figure 2.3: Deformation of a solid [9]

As the solid is brought from its original configuration to its deformed configuration all points in the solid begin to move as the load is applied. From figure 2.3 an arbitrary point at position x in the original configuration might move to a new position y at time t. Bower [9] then describes the displacement vector as in equation 2.29.

$$y_i = x_i + s_i(x_i, t) \tag{2.29}$$

Furthermore while the displacement field specifies the shape change in the solid, the velocity field would describe its motion and is defined in equation 2.30.

$$u_i(x_i, t) = \frac{\partial y_i}{\partial t} = \frac{\partial s_i(x_i, t)}{\partial t} \tag{2.30}$$

However instead of differentiating displacement with respect to time the displacement and deformations gradients can be computed along the solid and are defined as follows.

- Displacement gradient tensor: ∇s_i with components

$$\nabla s_i = \begin{bmatrix} \frac{\partial s_i}{\partial x_i} & \frac{\partial s_i}{\partial x_j} & \frac{\partial s_i}{\partial x_k} \\ \frac{\partial s_j}{\partial x_i} & \frac{\partial s_j}{\partial x_j} & \frac{\partial s_j}{\partial x_k} \\ \frac{\partial s_k}{\partial x_i} & \frac{\partial s_k}{\partial x_j} & \frac{\partial s_k}{\partial x_k} \end{bmatrix} \tag{2.31}$$

- Deformation gradient tensor: $F_{ij} = \delta_{ij} + \nabla s_i$ with components

$$F_{ij} = \begin{bmatrix} 1 + \frac{\partial s_i}{\partial x_i} & \frac{\partial s_i}{\partial x_j} & \frac{\partial s_i}{\partial x_k} \\ \frac{\partial s_j}{\partial x_i} & 1 + \frac{\partial s_j}{\partial x_j} & \frac{\partial s_j}{\partial x_k} \\ \frac{\partial s_k}{\partial x_i} & \frac{\partial s_k}{\partial x_j} & 1 + \frac{\partial s_k}{\partial x_k} \end{bmatrix} \tag{2.32}$$

Using the expressions defined in equations 2.31 and 2.32 one is able to derive the remaining variables that describe the shape change in solids. For instance the Jacobian of the deformation gradient defined in 2.33

$$J_{ij} = det(F_{ij}) \tag{2.33}$$

By using the Jacobian of the deformation tensor, the volume change of a solid due to a deformation may be determined. This principle is proven in the work by Bower [9], for incompressible materials $J = 1$.

Since deformations have now been defined the strain can now also be determined. For this there exist a range of strain tensors two of which will be described here. Firstly the Lagrange strain tensor can be found using equation 2.34.

$$\epsilon_{L,ij} = \frac{1}{2}(F_{ij}^T \cdot F_{ij} - \delta_{ij}) \tag{2.34}$$

Similarly to the Lagrangian description of fluid dynamics, the Lagrangian strain tensor quantifies the changes in length of a material fibre and angles between pairs of fibres in a deformable solid. Written out in terms of the displacement gradient the Lagrange strain tensor reads:

$$\epsilon_{L,ij} = \frac{1}{2}\left(\frac{\partial s_i}{\partial x_j} + \frac{\partial s_j}{\partial x_i} + \underbrace{\frac{\partial s_k}{\partial x_j}\frac{\partial s_k}{x_i}}_{\text{Non-linearity}} \right) \tag{2.35}$$

As seen in equation 2.35 a quadratic non-linearity can be seen this is described as a *geometric non-linearity* which may be neglected for small deflections [9].

Alternatively to the Lagrangian strain tensor the Eulerian strain tensor can be defined as in equation 2.36.

$$\epsilon_{E,ij} = \frac{1}{2}\left(\delta_{ij} - F_{ij}^{-T} \cdot F_{ij}^{-1} \right) \tag{2.36}$$

Similarly to the Lagrange strain tensor, except that it enables the computation of strain of an infinitesimal line element from its orientation *after* deformation. Written out in term of the displacement gradient:

$$\epsilon_{E,ij} = \frac{1}{2}\left(\frac{\partial s_i}{\partial x_j} + \frac{\partial s_j}{\partial x_i} - \underbrace{\frac{\partial s_k}{\partial x_i}\frac{\partial s_k}{\partial x_j}}_{\text{Non-linearity}} \right) \tag{2.37}$$

For the Eulerian strain tensor there too exists a geometric non-linearity as seen in 2.37 for small deformation gradient this non-linearity may also be neglected.

For a more detailed discussion of geometric non-linearities in solid mechanics the work by Holzapfel [19] on the subject is recommended. Additionally for an overview of how these effects are incorporated in applied solid mechanics the work by de Borst et al. [13] details how these non-linearities are included into the framework of finite element analysis.

For the purposes of this work large deformations are ignored and the Lagrangian strain tensor is linearised to give what is described in Bower [9] as the infinitesimal strain tensor 2.38

$$\epsilon_{ij} = \frac{1}{2}\left(\nabla s_i + \nabla^T s_i \right) \quad \text{or} \quad \epsilon_{ij} = \frac{1}{2}\left(\frac{\partial s_i}{\partial x_j} + \frac{\partial s_j}{\partial x_i} \right) \tag{2.38}$$

Principle of virtual work

When considering a solid that is deformed by external forces and one applies Newton's laws of motion i.e the conservation of linear and angular momentum an equilibrium equation may be defined. Take for instance the volume element in figure 2.4.

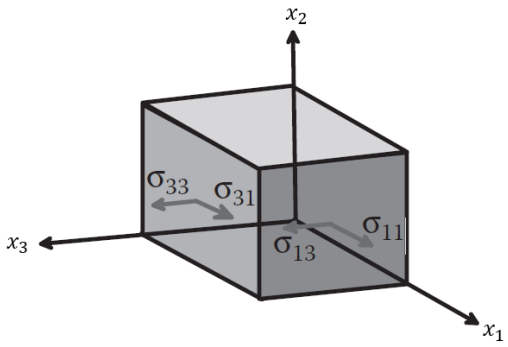

Figure 2.4: Stresses acting on a volume element [9]

Assuming that the volume element is subjected to a body force b_j and let y_i denote the position of a material particle in the deformed solid. The linear momentum balance in terms of stress can be defined as follows.

$$\frac{\partial \sigma_{ij}}{\partial y_i} + \rho b_j = \rho a_j \tag{2.39}$$

Similarly to the strain tensors introduced in the previous section there exist a variety of stress tensors as outlined below.

- Kirchhoff stress: $\tau_{ij} = J\sigma_{ij}$
- First Piola-Kirchhoff stress: $S_{ij} = J_{ij}F_{ik}^{-1}\sigma_{kj}$
- Second Piola-Kirchhoff stress: $\Sigma_{ij} = J\,F_{ik}^{-1}\sigma_{ki}F_{jk}^{-1}$

The above definitions of stress are by nature non-linear since large deformations are assumed, however when making the same assumptions as previously that $\frac{\partial s_i}{\partial x_j} << 1$ for which shape changes are characterized by the infinitesimal strain tensor defined in equation 2.38 then all stress measures defined previously become approximately equal to the Cauchy stress tensor seen in equation 2.40 as proven in [9].

$$\sigma_{ij} = t_j(x_i) \tag{2.40}$$

Where $t_j(x_i)$ denote the internal traction forces.

Now that the Cauchy stress tensor is defined the principle of virtual work can be understood. The principle of virtual work is an alternative way of expressing the equilibrium equation 2.39 derived from the equations of motion. While detailed derivation of the fundamental concepts will not be shown here as there exist plenty of references which already do so a grasp of this concept is important since this provides the starting point for finite element analysis. The use of re-writing the original equilibrium equation in terms of energy principals enables to write equation 2.39 as its *weak* or integral from. For equilibrium then the following must be satisfied.

$$W_{Internal} = W_{External} \tag{2.41}$$

Where $W_{Internal}$ is the internal / stored energy due to a members response to axial loading or a bending moment. $W_{External}$ is the work done on to the system by an external load for instance a force or a moment. For more detail reference can be made to appendix A which demonstrates an example calculation of the displacement calculation for a simply supported cantilever beam using energy methods. The equilibrium equation for linear moment introduced in equation 2.39 can thus also be written in terms of virtual work.

$$\underbrace{\int\int\int \sigma_{ij}\delta\epsilon_{ij}dV}_{W_{InternalVirtual}} = \underbrace{\int\int\int \rho b_i \delta s_i dV + \int\int t_i \delta s_i dA}_{W_{ExternalVirtual}} \tag{2.42}$$

In which for a static problem for every set of kinematically admissible virtual displacements the stress state σ_{ij} satisfies the static equilibrium from equation 2.39 $\nabla\sigma_{ij} + \rho b_i = 0$, where the admissibility is defined for the example calculation of a cantilever beam from appendix A.

2.2.2. Constitutive models

The equations described in the previous section apply universally to all deformable solids. However unless the deformation measure can be related to the internal forces these equations cannot be solved. It is for this purpose that constitutive models are used. These provide a set of equations relating stress to strain Bower [9]. Unlike the governing equations from the previous section, constitutive models are generally not derived from first principals although Holzapfel [19] mentions attempts to do so, particularly in modern non-linear continuum mechanics. For the most part however constitutive models are fit to experimental measurements.

Linear elasticity Linear elastic behaviours are the most basic models and follow the stress-strain relationship depicted in figure 2.5a. Of course other more complex models exist when attempting to describe the plastic deformation of a solid. However for the framework of this project the solid is assumed to be within the elastic regions and thus the issue of plasticity will not be described here in any great detail.

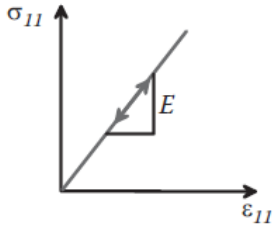

(a) Stress-strain relationship of isotropic, linear elastic material

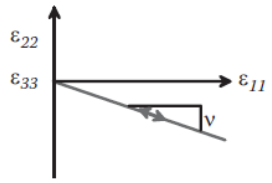

(b) Linear strain curve

Figure 2.5: Isotropic, linear elastic behaviour of a deformable solid Bower [9]

Assuming small deformations the infinitesimal strain tensor from equation 2.38 can be used. The stress-strain relation presented graphically in 2.5a can be expressed in matrix form written out in equation 2.43.

$$\begin{bmatrix}\epsilon_{11}\\ \epsilon_{22}\\ \epsilon_{33}\\ \epsilon_{23}\\ \epsilon_{13}\\ \epsilon_{12}\end{bmatrix} = \frac{1}{E}\begin{bmatrix}1 & -\nu & -\nu & 0 & 0 & 0\\ -\nu & 1 & -\nu & 0 & 0 & 0\\ -\nu & -\nu & 1 & 0 & 0 & 0\\ 0 & 0 & 0 & 2(1+\nu) & 0 & 0\\ 0 & 0 & 0 & 0 & 2(1+\nu) & 0\\ 0 & 0 & 0 & 0 & 0 & 2(1+\nu)\end{bmatrix} + \alpha\Delta T\begin{bmatrix}1\\1\\1\\0\\0\\0\end{bmatrix} \tag{2.43}$$

Where

- E [N/m^2]is the Young's/elastic modulus and is the slope of the stress-strain curve in uni-axial tension as in figure 2.5a often described as a measure of the stiffness of the solid [9].
- ν [-] is Poisson's ratio, which is a ratio of lateral to longitudinal strain in uni-axial tensile stress [9]. In figure 2.5b it is the slope between the lateral strain ϵ_{11} and longitudinal strain ϵ_{33}.
- The final term refers to the thermal effects with α [K$^-$1] being the thermal expansion coefficient and quantifies the change in volume of a material if it is heated in the absence of stress [9].

similarly the stresses can also be written in this form as seen in equation 2.44

$$\begin{bmatrix}\sigma_{11}\\ \sigma_{22}\\ \sigma_{33}\\ \sigma_{23}\\ \sigma_{13}\\ \sigma_{12}\end{bmatrix} = \frac{E}{(1+\nu)(1-2\nu)}\begin{bmatrix}1-\nu & \nu & \nu & 0 & 0 & 0\\ \nu & 1-\nu & \nu & 0 & 0 & 0\\ \nu & \nu & 1-\nu & 0 & 0 & 0\\ 0 & 0 & 0 & \frac{(1-2\nu)}{2} & 0 & 0\\ 0 & 0 & 0 & 0 & \frac{(1-2\nu)}{2} & 0\\ 0 & 0 & 0 & 0 & 0 & \frac{(1-2\nu)}{2}\end{bmatrix}\begin{bmatrix}\epsilon_{11}\\ \epsilon_{22}\\ \epsilon_{33}\\ \epsilon_{23}\\ \epsilon_{13}\\ \epsilon_{12}\end{bmatrix} - \frac{E\alpha\Delta T}{1-2\nu}\begin{bmatrix}1\\1\\1\\0\\0\\0\end{bmatrix} \tag{2.44}$$

This matrix expression may be written more conveniently in index notation as in equation 2.45

$$\sigma_{ij} = \frac{E}{1+\nu}\left[\epsilon_{ij} + \frac{\nu}{1-2\nu}\epsilon_{kk}\delta_{ij}\right] - \frac{E\alpha\Delta T}{1-2\nu}\delta_{ij} \tag{2.45}$$

Bower [9] expresses this stress strain relationship more compactly using the *elastic modulus tensor* C_{ijkl}.

$$\sigma_{ij} = C_{ijkl}(\epsilon_{kl} - \alpha\Delta T\delta_{kl}) \tag{2.46}$$

Where the *elastic modulus tensor* C_{ijkl} is defined in equation 2.47

$$C_{ijkl} = \frac{E}{2(1+\nu)}(\delta_{il}\delta_{jk} + \delta_{ik}\delta_{jl}) + \frac{E\nu}{(1+\nu)(1-2\nu)}\delta_{ij}\delta_{kl} \tag{2.47}$$

2.2.3. Finite element method

In order to solve the governing equation discussed previously for large scale problems advantage must be taken of numerical methods. In most commercial CSM tools the finite element method is the preferred strategy for solving such problems, mainly through the displacement-based methods [13] discussed previously. Starting with the principal of virtual work described in equation 2.42 and stated again here for ease of reference.

Weak form of governing equations

$$\int\int\int \sigma_{ij}\delta\epsilon_{ij}dV = \int\int\int \rho b_i\delta s_i dV + \int\int t_i\delta s_i dA$$

and defining a virtual strain field

$$\delta\epsilon_{ij} = \frac{1}{2}\left(\frac{\partial\delta u_i}{\partial x_j} + \frac{\partial u_j}{\partial x_i}\right) \tag{2.48}$$

if this virtual strain satisfies the admissibility criterion defined in appendix A then the equation of stress equilibrium as well as force boundary conditions are satisfied.

Re-writing the first term of the virtual work integral in terms of the *elastic modulus tensor* yields.

$$\int\int\int C_{ijkl}\frac{\partial s_k}{\partial x_l}\frac{\partial u_i}{\partial x_j} = \int\int\int \rho b_i\delta s_i dV + \int\int t_i\delta s_i dA \tag{2.49}$$

Interpolation/Shape Functions

The first step in finite element analysis then is to compute a displacement that satisfies equation 2.49. Secondly in order to solve the integral numerically one discritzes the displacement and velocity fields, this is done by subdividing the geometry into elements. One such discritisation can be seen in figure 2.6

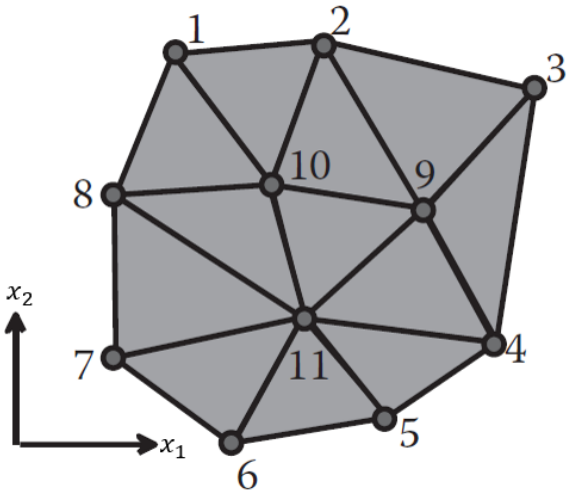

Figure 2.6: Typical finite element mesh [9]

The interpolation of the displacement field can then be written more generally as

$$s_i(x) = \sum_{a=1}^{n} N^a(x^b) s_i^a \tag{2.50}$$

where

- x denotes an arbitrary point in the solid.
- $N^a(x)$ is the interpolation function also referred to as shape function.

Interpolation functions are a function of position and geometry only. Examples of shape functions of a 1D element are presented in figure 2.7.

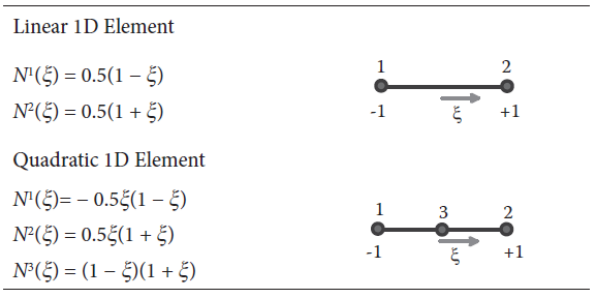

Figure 2.7: Shape functions for 1D elements [9].

in which ξ is a dimensionless length scale. The computation of more complex geometry require different element types and thus more thought must be put into the selected shape functions.

The velocity field can be interpolated in exactly the same way as the displacement in 2.51

$$u_i(x_i) = \sum_{a=1}^{n} N^a(x_i^b) u_i^a \tag{2.51}$$

Construction of system of equations

Substituting the interpolation function for the displacement field (2.50) and velocity field (2.51) into the virtual work equation 2.49 yields the following.

$$\int\int\int C_{ijkl}\frac{\partial N^b(x_i)}{\partial x_l}u_k^b\frac{\partial N^a(x_i)}{\partial x_j}\delta u_i^a dV - \int\int\int \rho b_i N^a(x_i)\delta u_i^a dV + \int\int tN^a(x_i)\delta u_i^a dA = 0 \quad (2.52)$$

From equation 2.52 the elastic modulus tensor (C_{ijkl}) is a function of the elastic properties of the solid. Furthermore the interpolation function ($N^a(x_i)$ is a function of the geometry and nodal positions which are all known quantities. Grouping these terms enables the definition of the stiffness matrix K_{aibk} defined in equation 2.53. Similarly for the remaining two terms on the left a force vector F_{ij} seen in equation 2.54 may be defined based on the known body forces (ρb_i), loading condition at the boundary (t_i) and the interpolation function which as mentioned before is also known.

$$K_{aibk} = \int\int\int C_{ijkl}\frac{\partial N^a(x_i)}{\partial x_j}\frac{\partial N^b(x_i)}{\partial x_l} \quad (2.53)$$

$$F_i^a = \int\int\int \rho b_i N^a(x_i)dV + \int\int t_i N^a(x_i)dV \quad (2.54)$$

Now the virtual work equation can be expressed in matrix form as in equation 2.55.

$$\left(K_{aibk}s_k^b - F_i^a\right)\delta u_i^a = 0 \quad (2.55)$$

In summary then the steps to the finite element method are as follows.

- Computation of the element stiffness matrix K_{aibk} using the known material properties and interpolation function.
- Sum for all elements to obtain the global stiffness matrix
- Computation of force vector F_{ij} made up of body forces (if available) and traction boundary conditions on the surface.
- Sum for all elements to obtain the global force vector
- Include constraints by enforcing displacement boundary conditions in the stiffness matrix
- Solve the system of linear equations 2.56 for the unknown displacements s_1^b

$$Ks_1^b = F^a \quad (2.56)$$

2.3. Coupling of CFD and CSM

This section discusses the state-of-the-art in terms of how coupled fluid-structure interaction (FSI) problems are approached in industry and academia. First the various coupling approaches are described, stating the advantages and disadvantages of each including some examples from industry. The next part describes current industry practices in the thermohydraulic modelling of plate fin heat exchangers (PFHE)

2.3.1. Types of coupling

Firstly the different types of coupling will be discussed, followed by some examples from industry and academia. The simulation of fluid structure interaction problems can be approached in two ways. One is the *monolithic* approach which solves the governing equations of fluid and solid domains in a single solver. Alternatively the *partitioned* approach solves the governing equation of the solid and fluid domain in two separate solvers [14]. The advantage of the monolithic approach is that it is widely believed to be more robust, furthermore the fixed-point iteration used in partitioned solver tend to converge slowly and are prone to diverge when confronted with strong fluid-structure interaction [15]. However while the partitioned approach may suffer from stability issues in extreme cases it is still worth considering since through the separation of the physical regimes into the individual solvers allows for the use of existing, commercial solver codes which have been thoroughly validated and built upon an extensive library of previous experiences in the individual fields [51]. However unlike the monolithic approach

the partitioned approach requires an additional step that communicates data at the fluid solid interface region. Fortunately many of the multi-physics package providers such as ANSYS and Dassult Systems provide in-built tools that take care of this, as long as their solvers are used. For data transfer between two different solver brands there too exist a variety of options in the form of third party solver coupling tools. The most popular of which being the MpCCI tool developed by the Frauenhofer insitute which support a variety of commercial codes [16]. Other popular alternatives include the coupling library developed at TU München called PreCICE [10], Fluid-Structure-Interaction Simulation Manager (FSiM) developed at the Karlsruhe Institute of Technology [35] and OpenPALM developed at CERFACS [49]. Due to the coupling process of the two solvers in the partitioned approach use of different algorithms result in different types of partitioned FSI approaches. For a complete overview of these approaches reference is made to figure 2.8.

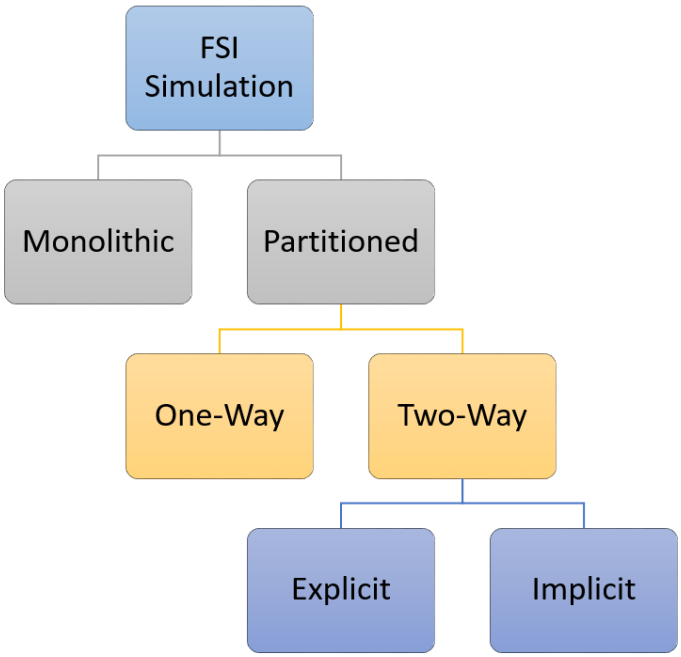

Figure 2.8: Overview of different approaches to FSI simulation.

Whether the solution method is one-way or two way will dictate the extent of the communication between the two solvers. As the name suggests the one-way method enables data transfer from one solver to the other only whereas the two-way solver allows for data to be sent back and forth between the solvers. This makes the two-way approach ideal for problems in which say the fluid causes a deformation onto a structure and the deformed structure in turn affects the flow. Due to this added layer of complexity the two-way approach is computationally more expensive and should thus only be considered when a strong fluid-structure interaction is expected. From figure 2.8 the two-way method can be further subdivided into explicit and implicit. These two options indicate the interactions in each of the simulations. Explicit solves each coupled time step without further iterations between the time-steps, conversely the implicit approach iterates between each time-step, ensuring that the previous time-step is converged before moving on to the next one.

2.3.2. General examples of FSI

This section will discuss some relevant engineering applications of FSI simulations as well as what methods were used and how they were implemented.

One-Way FSI

Generally the simplest way of simulating fluid structure interaction is through a one-way partitioned approach. This method is especially popular in the process industry where a structure is often effected

by the fluid and the reverse effect of the structure on the fluid is very small and thus negligible. The general procedure of one-way FSI simulation are summarized in figure 2.9.

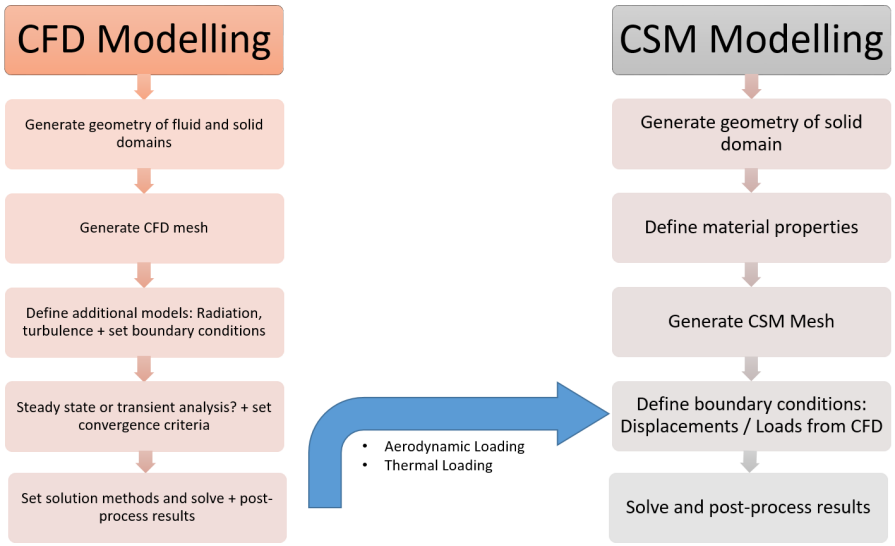

Figure 2.9: Summarized work flow of one-way FSI modelling.

One example from industry concerns the piping in process plants. These are exposed to cyclical thermal stresses furthermore due to mixing of fluids at different temperatures thermal stratification will occur. Causing the fluid at lower temperature to culminate at the bottom and the warmer fluid rising to the top. This generates large temperature gradients in the radial direction of the pipe and causes an uneven stress field along the pipe walls. The works by Zhang et al. [66], Zhang and Lu [65] make use of CFD to solve for both the convective heat transfer in the fluid and conduction across the pipe walls. After obtaining the temperature of the solid pipe this data was imported to a finite element mesh for which a displacement and stress analysis was carried out. This work made use of large eddy simulation to account for the turbulent effects present. However this method requires much finer meshes and therefore greater computational effort. Alternatively to this Kim et al. [26] investigated a similar scenario however instead of using an LES approach the much simpler SST model was used. The results of the transient thermal stratification can be seen in figure 2.10a.

From the figure it becomes evident that very large temperature differences begin to occur of approximately 150 K. Additionally Kim et al. [26] employs an external coupling interface MpCCI to communicate the thermal data from one solver to the other. The resulting stress can be seen to occur at the site of thermal stratification as seen in figure 2.10b.

Another example is the work by Schuler et al. [45] which looks at the temperature distribution and resulting stress distribution in a T-junction pipe. The work was compared to an experiment conducted in an FSI test facility concluding that the numerical results where very close to the experimental data.

Li et al. [31] performs a one-way analysis on dual-coolant lithium-lead blanket, a key technology in thermo-nuclear reactors. This component contains an insert which serves as an electrical and thermal insulator between the fluid and load bearing steel structure. Thus by applying one-way thermal FSI methods the stresses of the inserts can be estimated and measures can be taken to reduce and estimate when and where failure would occur.

Wang et al. [54] applies this FSI approach to determining the stresses that occur in a hydrogen storage cylinder during fast filling. In this simulation a 2-D CFD analysis was made of the refuelling process. Rather than just transferring the temperature, the pressure as a result of the hydrogen jet impinging on the cylinder walls were also transferred to obtain the stresses in the composite layers of the inner wall of the storage cylinder in the FEM model.

Further examples of one-way FSI include the modelling of aerodynamic loads on wind turbine blades

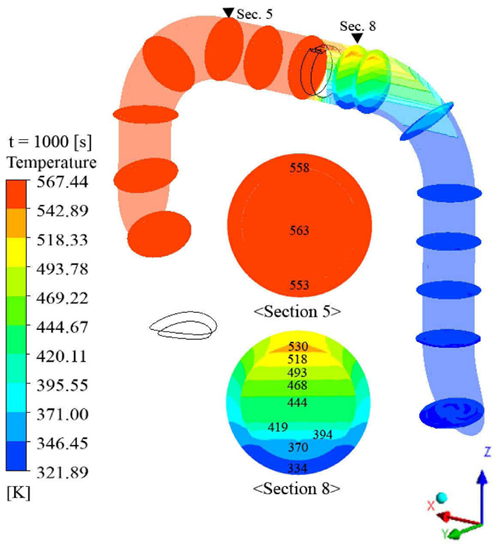

(a) contour plots of temperature distribution across valve in pipe at 1000s Kim et al. [26]

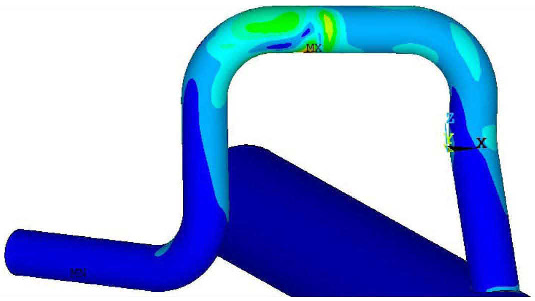

(b) Instantaneous Von Mises Stress distribution at 1000s

Figure 2.10: CFD (left) and CSM (right) analysis of safety injection piping subject to thermal stratification [26]

as done in the work by Wang et al. [55]. As well as the thermohydraulic/mechanical modelling of a helium cooled divertor for use in fusion power plants by Widak et al. [57]. Here no conjugate heat transfer is carried out, rather the heat transfer coefficients are taken from the surface of the CFD model and mapped on the solid surface of the CSM model which simulates the conduction through the body and finally the mechanical stresses.

Two-Way FSI

For strongly coupled systems, defined as those who's physical responses in the fluid domain depend on the deformations in the structural domain and vice versa, a bidirectional data exchange is essential to sufficiently model such a system. Uses of such models are generally encountered in the aerospace industry where even small deformations in the structure may have significant impact on the flow. The work by Yunju et al. [62] aims to investigate the dynamic structural response of an elastic thin-shell structure exposed to aerodynamic loading. In this simulation the CFD solver computed the unsteady solution for one time-step before transferring the aerodynamic force obtained to the structural model then the same time-step is computed in the CSM solver via FEM. The structural displacements and elastic deformation are transferred to the CFD mesh as updated boundary conditions. The above steps are repeated until convergence. The work by Zhao et al. [67] predicted the extent of transonic wing flutter using a similar method. The works by Du [14] and Pei et al. [41] carried out research in the field of turbomachinery. Pei et al. [41] measured impeller deflection for off-design loading conditions while Du [14] simulated labyrinth seals used in gas turbines which experience both extreme aerodynamic loading as well as high temperatures thus a bidirectional coupling was done using both variables. To summarize the implicit two-way FSI method described here figure 2.11 can be used as reference which roughly explains the conceptual steps. While examples of two-way FSI have been mentioned here, for the purposes of this work only a one-way FSI will be carried out as the impact of the structure on the fluid flow is assumed negligible.

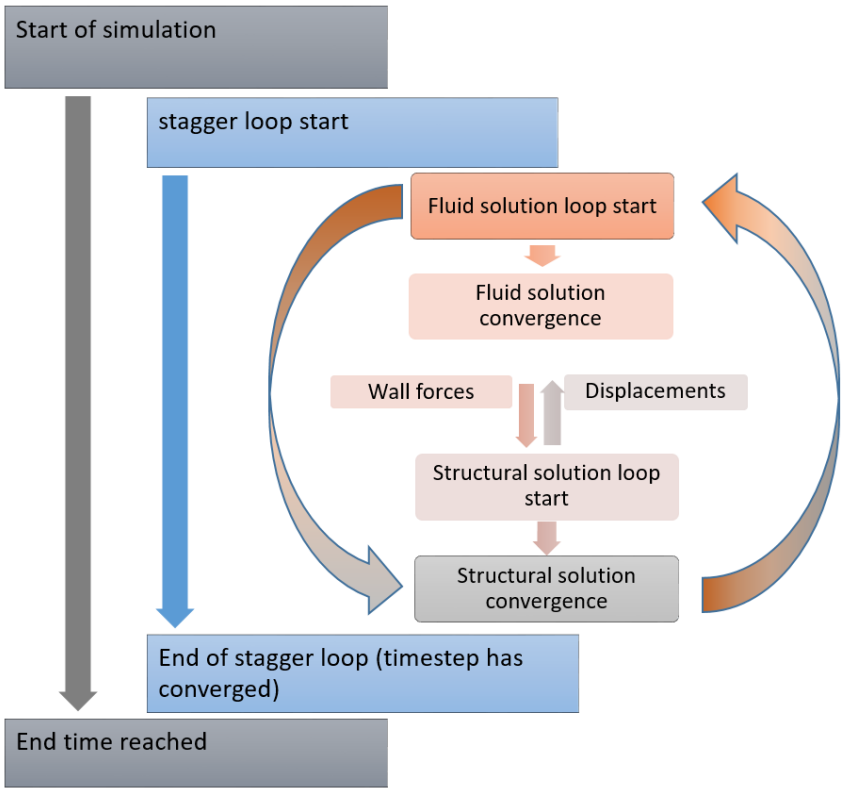

Figure 2.11: Summarized work-flow of two-way, implicit FSI modelling.

2.3.3. Modelling of plate fin heat exchangers

In industry thermo-fluidic modelling is a subject of great interest since understanding thermal phenomena can give insight into the performance and longevity of heat exchangers and other thermal equipment. The methodology to model such effects should present accurate results in terms of temperature distribution in the equipment while also being robust when simulating different operating conditions. Such operating conditions include expected changes in plant operation in the case of plant start-ups and shut-downs as well as unexpected scenarios such as failure of equipment within the plant. It is claimed by Freko et al. [17] that these events or special operations cases can cause significant reduction of lifetime of equipment due to the sudden variation of temperature within the equipment. As well as this the model setup must be streamlined and relatively ”lightweight” which can be achieved by reducing the number of equations being solved. Doing so will reduce computational effort and maintain an ability to generate results in a timely manner. The state of the art methodology applied by Woitalka et al. [59] when it comes to thermohydraulic modelling of heat exchangers is based on an in-house, Linde process simulation tool *OPTISIM*. Within this process simulator a heat exchanger model may be implemented in a modular manner which enables the inclusion of different heat exchangers within the simulation. Each heat exchanger model is broken down into the fundamental conservation equations, namely mass, momentum and energy as well as the phenomenological correlations which define heat transfer and pressure drops as described in Woitalka et al. [59]. Figure 2.12 shows a graphic representation of the model decomposition for a heat exchanger.

As can be seen from figure 2.12 the energy exchange of all three streams(S1, S2, S3) are modelled through the energetic coupling of spatially distributed heat capacities which describe the common wall (CW). The common wall describes the entire heat transfer surface of the heat exchanger. For instance in the case of shell and tube heat exchangers these are the metal tubes and in plate fin heat exchangers this would be the parting sheets. Furthermore the streams are modelled by 1-D streamlines which are described by 1-D Navier-Stokes equations. Since in a variety of heat exchangers such as Coil-Wound heat exchangers as well as shell and tube heat exchangers multi-phase flow characteristics play a major role these are account for in the dynamic model. Equation 2.57 defines the density of the two-phase fluid which is assumed to be homogeneous such that both vapour and liquid phase have the

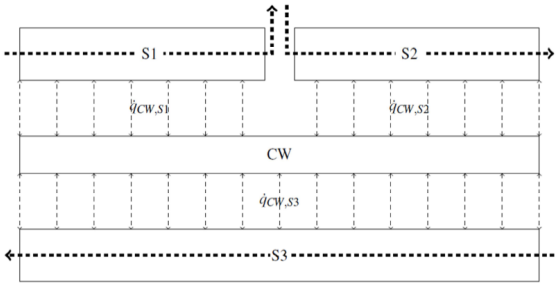

(a) Decomposition scheme of a counter-current heat exchanger with three flow passages S1, S2, S3 and the metal wall CW Woitalka et al. [59]

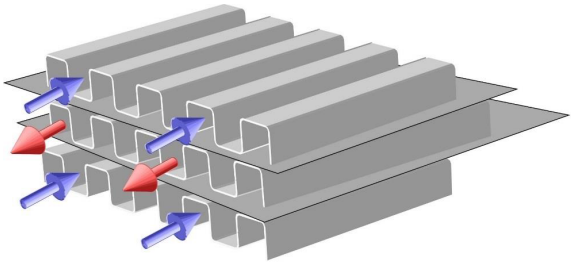

(b) PFHE in counter-current arrangement as modelled in the dynamic formulation in 2.12a.

Figure 2.12: 1-D Common Wall Model Woitalka et al. [59]

same velocity.

$$\rho = \gamma \cdot \rho_v + (1 - \gamma) \cdot \rho_f \tag{2.57}$$

Where ρ_v and ρ_f are the vapour and liquid densities and γ is the vapour fraction. Furthermore since density is not constant the compressible Navier-Stokes equations are applied as seen in equation 2.58, 2.59 and 2.60.

$$\frac{\partial}{\partial t}\rho_j + \frac{\partial}{\partial z}(\rho_j w) = \dot{r}_j, j = 1, ..., nc \tag{2.58}$$

$$\frac{\partial}{\partial t}(\rho w) + \frac{\partial}{\partial z}(\rho w^2) = -\frac{\partial}{\partial z}p + \left(\frac{\partial p}{\partial z}\right)_{fric} + \rho g sin(\theta) \tag{2.59}$$

$$\frac{\partial}{\partial t}(\rho E) + \frac{\partial}{\partial z}(\rho E w) = -p\frac{\partial}{\partial z}u_z + w\left(\frac{\partial p}{\partial z}\right)_{fric} + \frac{\mathbf{P}}{A_c}\dot{q} \tag{2.60}$$

where *nc* denotes the number of components, $\dot{r}_j$ is the reaction rate of the component *j*, *E* is the the total energy and $\mathbf{P}$ for the perimeter, lastly $\left(\frac{\partial p}{\partial z}\right)_{fric}$ is the irreversible pressure drop.

Next to conservation equations, phenomenological correlations are used to describe heat transfer coefficients and pressure drops which depend on vapour fraction (γ), *Nu*, *Pr* or any local quantity along the passage. Applying different correlations will enable to model different heat exchangers, and flow conditions.

One of the main advantages of such a modelling approach is the seamless integration of the heat exchanger model whose flow sheet can be compiled as a module into the process simulator as described in Freko et al. [17]. In doing so the impact of various plant operating conditions on the heat exchanger can be simulated with relative ease. Finally this method is also able to model multiphase flow maldistribution which will give an additional insight into the flow properties. Main disadvantage of the method is the lack of a fully resolved 3-D flow as the model essentially follows a streamline for each of the passages. Moreover although multiphase flows can be modelled this can only be done by assuming homogeneous flow, meaning that the liquid and vapour parts are moving at equal velocity therefore heterogeneous flow phenomena such as phase slip are neglected in the current model.

3

Large Scale Model

To gain a better understanding of thermo-hydraulic phenomena in 3-D resolution and the resulting thermal stresses of a large scale geometry some additional modelling effort is required. This chapter will cover the implementation of a fin model based on porous media as well as the coupling of CFD and CSM solver for the stress analysis. Firstly the fin model will be introduced which includes an introduction to porous media, covering the governing equations as well as the phenomenological correlations used to represent a given fin type. Secondly the model implementation for the large scale geometry is discussed. This entails a description of the geometry followed by the scenario that is to be simulated as well as the general setup of both the CFD and CSM simulation which include rigorous mesh studies for both solvers and an explanation with regards to the coupling procedure. Finally the results of both temperature distribution and resulting stresses are presented as well as a comparison with the current 1-D dynamic model.

3.1. Fin Model

Commencing this chapter is a brief description of how fins are modelled using the porous media approach. Figure 3.1 below provides a graphical representation of how the porous media are used based on a section of a PFHE. The fins to be modelled are seen on the left in this case these are two layers of

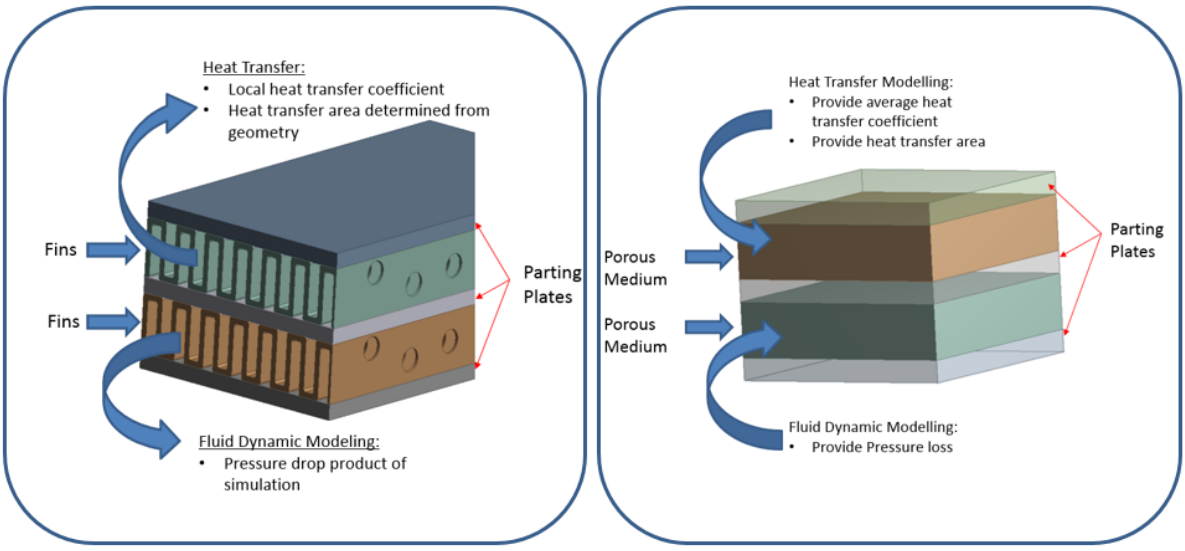

Figure 3.1: Geometry of Porous geometry for submodel of the PFHE.

perforated fins separated by a thin parting sheet. Simulating this geometry would require to capture the

geometric details of the fins and perforations, for this a highly refined mesh would be required to resolve the relevant scales resulting in extensive computational effort. Moreover only a small segment of the heat exchanger could be modelled and thus the global variables across the entire equipment cannot be known. The right side of figure 3.1 displays the simplified geometry in which the fins are replaced by homogeneous, porous blocks. Since this model neglects any of the intricacies of the original geometry variables such as local heat transfer coefficients as well as pressure loss cannot be determined. Manufacturers of fins often conduct extensive experimentation in order to build correlations that describe thermal and hydraulic behaviour of a particular fin. Advantage of such correlations is taken in order to build a fin model that is representative of a particular fin.

3.1.1. Porous media

Having introduced the modelling approach it is important to define what is meant by a porous medium and how these are treated in CFD. A Porous medium refers to a material with a solid matrix consisting of gaps, occupied by fluid as in figure 3.2. Nield and Bejan [39] states that the interconnectedness of these voids or pores allow fluids to flow through the material.

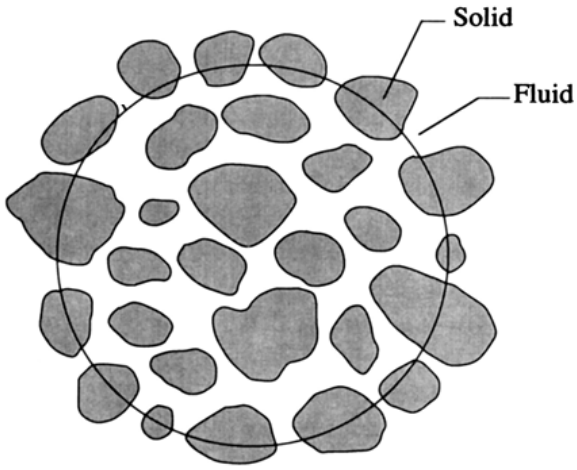

Figure 3.2: Example of a representative porous volume as seen in Nield and Bejan [39].

Governing equations of porous media

In general the conservation equations used to describe fluid flow in porous media as seen in Nield and Bejan [39] are described below. Starting with the conservation of mass as described by the continuity equation 3.1.

$$\phi \frac{\partial \rho_f}{\partial t} + \frac{\partial}{\partial x_i}(\rho_f u_i) = 0 \tag{3.1}$$

This equates the increase of mass of the fluid as defined by the time derivative to the mass flux into the volume defined by the divergence term where the subscript *f* and *s* denote the fluid voids and solid matrix respectively. Note the addition of the dimensionless variable ϕ which is the porosity and defines the ratio of fluid void to the total volume with $\phi_s = 1 - \phi$ being the fraction occupied by the solid. Conservation of momentum in porous media is described by the general momentum equation as described equation 2.7 with the addition of a source term S_M and ϕ.

$$\phi \frac{\partial \rho_f u_i}{\partial t} + u_j \frac{\partial}{\partial x_j}(\rho u_i) = \mu \left(\frac{\partial^2 u_i}{\partial x_j^2} \right) + S_M \tag{3.2}$$

There exist a few variations of this source term (S_M) to define flow in porous media. The most common is Darcy's law which states that flow velocity is directly proportional to the pressure gradient as in equation 3.3.

$$u = \frac{1}{\mu} K_{perm} \nabla p \tag{3.3}$$

Where K_{perm} is the specific permeability matrix and is independent of the fluid but rather depends on the geometry of the medium. Furthermore assuming isotropic porosity this is a scalar and making the pressure gradient the subject of the equation yields equation 3.4.

$$\nabla p = -\frac{\mu}{K_{perm}} u_i \tag{3.4}$$

While for low Reynolds numbers the linear drag term introduced by Darcy holds, increasing the Reynolds number will show that the relationship between velocity and pressure gradient is non-linear. For this reason a quadratic drag term originating from Forschheimer's equation is added to give the Darcy-Forschheimer law for flow in porous media 3.5.

$$\nabla p = \frac{\mu}{K_{perm}} u_i - c_F K_{perm}^{-\frac{1}{2}} \rho_f |u_i| u_i \tag{3.5}$$

Where c_F is a dimensionless drag constant. Figure 3.3 is a plot of friction factor (f_K) as a function of Reynolds number *Re*. The linear, Darcy regime occurs between *Re* = 0.1-1, while transition occurs between *Re* = 1-10 where the Forschheimer term begins to dominate.

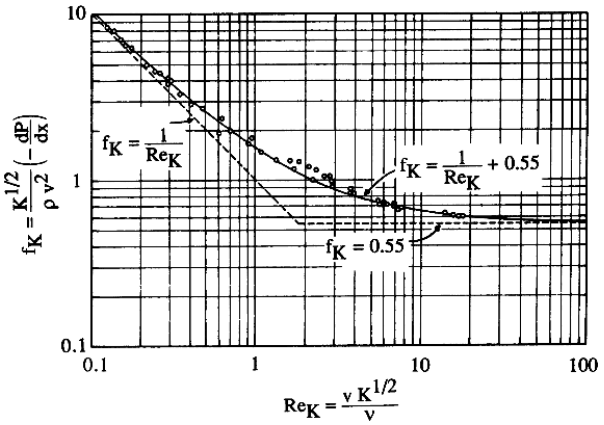

Figure 3.3: Transition from the Darcy regime to the Forschheimer regime in unidirectional flow through an isothermal saturated porous medium from [39].

Alternative source terms exist to model porosity such as Brinkman's equation [39] seen in equation 3.6

$$\nabla p = -\frac{\mu}{K_{perm}} u_i + \tilde{\mu} \frac{\partial^2 u_i}{\partial x_j^2} \tag{3.6}$$

where the quadratic, Forschheimer term is replaced by a viscous term similar to the Laplacian appearing in the Navier-Stokes equations. In which $\tilde{\mu}$ being the effective viscosity which depends on the porosity and tortuosity of the medium. However since the CFD solver employed makes use of the Darcy-Forschheimer relation the remaining work will use the source term as displayed in equation 3.7.

$$S_M = -\frac{\mu}{K_{perm}} u_i - K_{loss} \frac{\rho}{2} |u_i| u_i \tag{3.7}$$

Where $K_{loss} = c_F K_{perm}$ and is termed the quadratic loss coefficient. Writing the Darcy and Forschheimer terms as constants C_1 and C_2 as seen in equation 3.8 and 3.9 respectively,

$$C_1 = \frac{\mu}{K_{perm}} \tag{3.8}$$

$$C_2 = K_{loss} \frac{\rho}{2} \tag{3.9}$$

the source term which is essentially a pressure loss over a given length and is written as a quadratic equation in 3.10.

$$\frac{\Delta p}{l} = S_M = -C_1 u_i + C_2 u_i^2 \tag{3.10}$$

The final equation of the governing principles of fluid flow in porous media concerns the the treatment of the energy equation. Essentially there are two ways to express the energy equation, firstly heat transfer may be considered for the fluid voids in isolation. This way of implementing the energy equation is termed the *thermal equilibrium model*. Alternatively it is possible to prescribe a *thermal non-equilibrium model*, this defines a finite temperature difference between the solid matrix and fluid void thus an additional energy equation describing the solid matrix is required. The energy equations for the fluid and solid phases are defined in equations 3.11 and 3.12 respectively.

$$\frac{\partial}{\partial t}(\rho_f \phi h_f) + \frac{\partial}{\partial x_i}(\rho_f K_{perm} \cdot u_{i,f} h_f) = \frac{\partial}{\partial x_i}(\lambda_f K_{perm} \nabla T) + \phi S_{E,f} + Q_{fs} \tag{3.11}$$

$$\frac{\partial}{\partial t}(\rho_s \phi_s h_s) + \frac{\partial}{\partial x_i}(\rho_s K_{perm,s} \cdot u_{i,s} h_s) = \frac{\partial}{\partial x_i}(\lambda_s K_{perm,s} \nabla T_s) + \phi_s S_{E,s} + Q_{sf} \tag{3.12}$$

Where the subscripts *f* and *s* represent the fluid and solid components respectively. The software applies a dual cell approach in which the solid region is superimposed on the fluid region where and the heat transfer between the fluid and solid is determined by a standard heat transfer coefficient as shown in equation 3.13.

$$Q_{fs} = -Q_{sf} = h_c A_{fs}(T_s - T_f) \tag{3.13}$$

Where h_c is the overall heat transfer coefficient between the fluid and solid and A_{fs} is the interfacial area density between the fluid and solid and is defined by equation 3.14.

$$A_{fs} = A_\alpha \left(\frac{A}{V} \right) \tag{3.14}$$

Where A_α represents the contact area between fluid of fraction α with solid. For single phase flow A_α=1, and the remaining terms is calculated using the geometric features of the fin type.

Phenomenological correlations

In order to determine the coefficients stated in equation 3.10 use of correlations are made which are representative of a given fin type. These correlations are often defined using dimensionless groups that define momentum and heat transfer such as the Fanning friction and Colburn (j-factor) respectively which are defined in the textbook by Seader and Henley [46]. Starting with the correlation for the momentum given as a relationship between the Fanning friction factor *f* and Reynolds number by applying equations 3.15 and 3.16 pressure drop and velocity can be calculated.

$$\Delta p = 4f \frac{l_p}{d_h} \frac{\Phi^2}{2\rho} \tag{3.15}$$

$$u = \frac{Re\mu}{\rho d_h} \tag{3.16}$$

Where *f* l_p, d_h and Φ are the Fanning friction factor, streamwise length of the flow domain, hydraulic diameter and mass flux respectively. Using these as well as fanning friction correlations for the specific fin type, similarly to the correlation seen in figure 3.4a. A plot can be made which describes the pressure loss as a function of velocity.

By fitting a second order polynomial trendline to the data one is able to determine both the linear (C_1) and quadratic (C_2) resistance coefficients. The work by Wang et al. [56] and Cetin and Aksel [11] use this approach to define pressure losses in the porous media and are therefore able to investigate the extent of flow maldistribution in fins. Cetin and Aksel [11] goes beyond this and additionally includes a heat transfer model by taking into account the energy equation with addition of *thermal non-equilibrium model*. Similarly to the pressure drop the heat transfer coefficient is implemented using experimentally

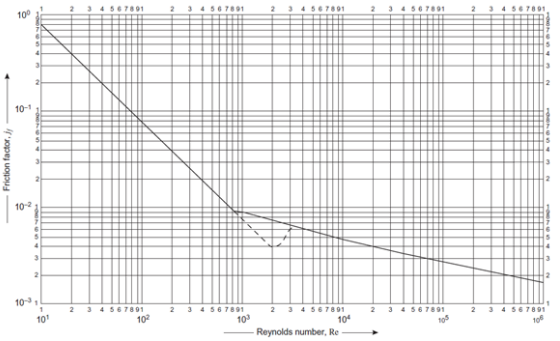

(a) Tube-side friction factor for a shell and tube heat exchanger [50].

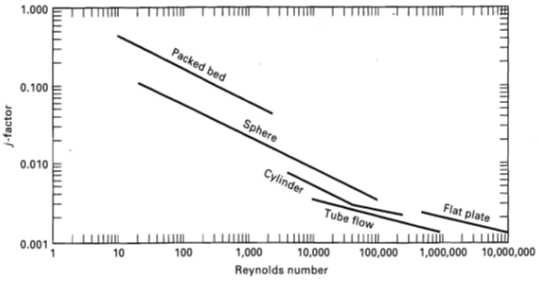

(b) Chilton-Colburn j-factor correlations for different flows.

Figure 3.4: Experimentally determined correlations describing mass and heat transfer for various flows[46].

determined correlations. For heat transfer such a correlation exists in the form of the dimensionless term known as the Colburn factor (j) which is a function of the Reynolds number as seen in figure 3.4b.

Applying equation 3.17 one is able to determine the heat transfer coefficient between the fluid and solid regions.

$$h_c = \frac{j\Phi c_p}{Pr^{\frac{2}{3}}} \tag{3.17}$$

By fitted a power law curve to the data it is possible to define the heat transfer coefficient as a function of flow velocity which is calculated assuming the flow is compressible through the application of an equation of state.

3.1.2. Mesh convergence study CFD

In the interest if saving time the mesh convergence study was carried out on two counter current channels of the PFHE, as seen in figure 3.5. For this mesh convergence and following validation study a separate set of boundary conditions regarding flow velocity and temperature are used which can be seen in the table C.1 in the appendix.

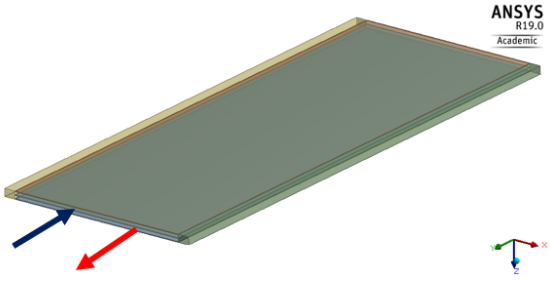

(a) Two channel PFHE submodel.

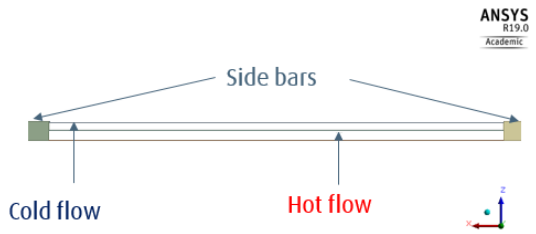

(b) Streamwise cross-section of two channel PFHE submodel.

Figure 3.5: Geometry of two channel model used in the mesh convergence and validation of the fin model.

For the mesh convergence two main variables were investigated: Firstly the cell length in streamwise direction was changed. Secondly the effect of the cell height is also investigated. A range of cell lengths were investigated ranging from 5mm to 500mm, figure 3.6 shows two such examples.

The variables selected for monitoring were the metal temperatures at either ends of the parting plate between the two counter current flow channels. The results of which are presented in figure 3.7 which shows a comparison of different cell lengths.

From this it becomes evident that between the coarsest and finest mesh a maximum temperature difference of approximately 8.5K can be seen which occurs at both ends of the parting plate. The plot

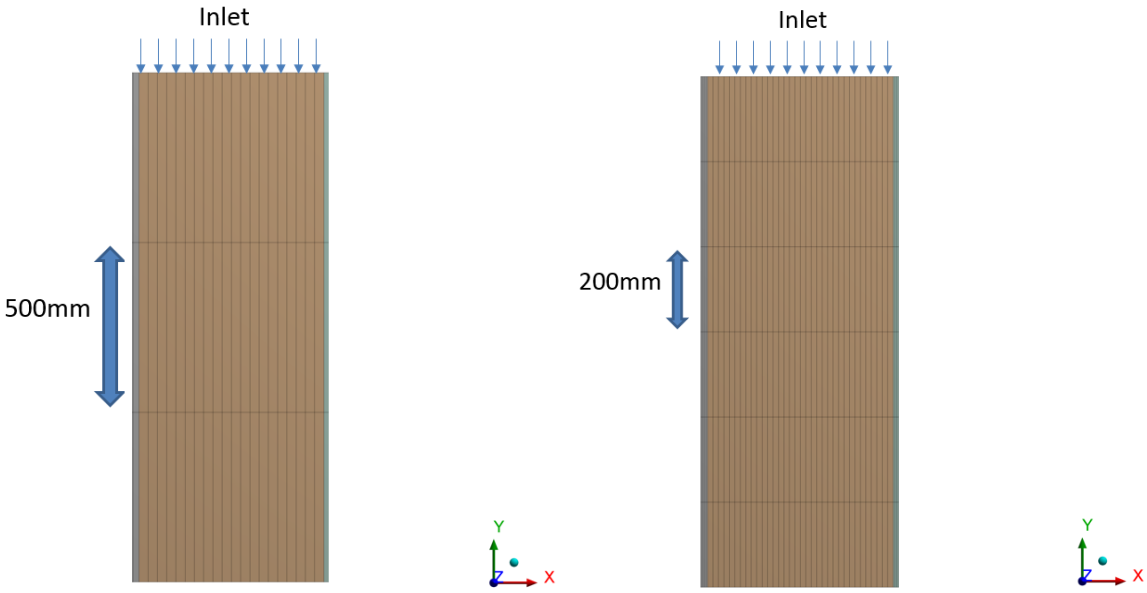

(a) Mesh with 500mm cell length in streamwise direction.

(b) Mesh with 200mm cell length in streamwise direction.

Figure 3.6: Comparision of 500mm and 200mm cell lengths.

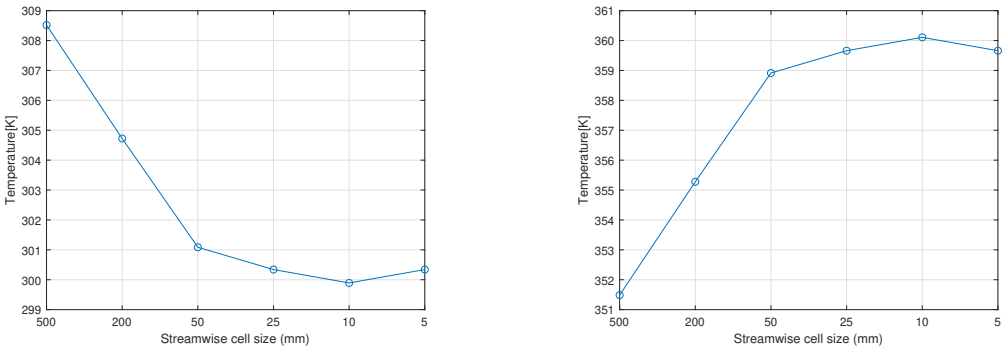

(a) Steady-state temperature at middle parting plate at cold inlet/hot outlet for different cell lengths.

(b) Steady-state temperature at middle parting plate at cold outlet/hot inlet for different cell lengths.

Figure 3.7: Comparison of different cell lengths in streamwise direction.

also indicates that as the cell length decreases one converges to a temperature value. For a cell length of 50mm the solution was considered sufficiently converged. Another point of interest were the cells heights required to ensure mesh independent results. For this study the porous domain and the parting plates were investigated separately. For the porous domain an attempt was made using one cell this was then doubled continuously to a maximum of 16 cells as seen in figure 3.8. This method was also followed for the parting plates up to a maximum of 4 cells.

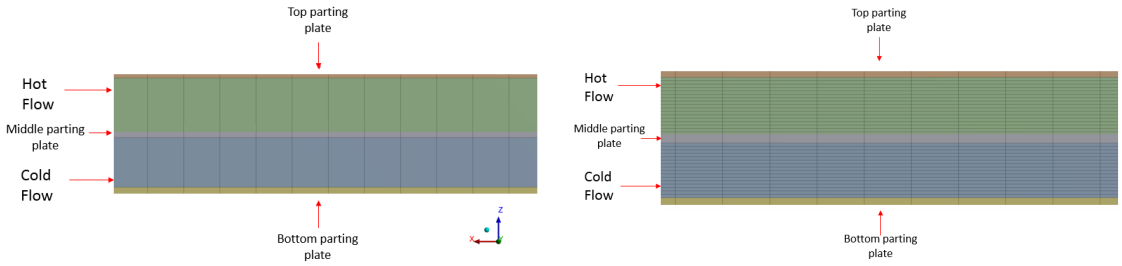

(a) Mesh with 1 cell in transverse direction of porous volume.

(b) Mesh with 16 cells in transverse direction of porous volume.

Figure 3.8: Different cells heights for porous domain.

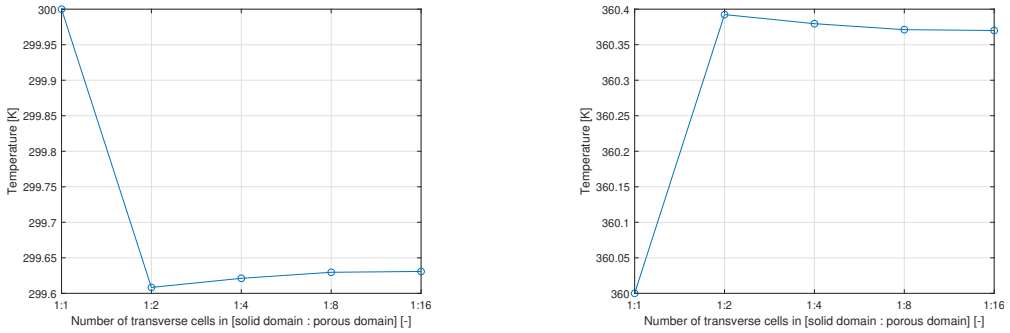

(a) Steady-state temperature at cold inlet/hot outlet of parting plate.

(b) Steady-state temperature at hot inlet/cold outlet of parting plate.

Figure 3.9: The effect of cell heights in porous domain on temperature at the either ends of the parting plate.

From figure 3.9 it is evident that decreasing cell height has little impact on the temperature at either end of the parting plate. A maximum temperature difference of about 0.4K occured between using a single cell and using 2 cells in the porous domain. To be on the safe side the use of 2 cells will be continued to resolve the porous domain. Next the solid domain was investigated specifically the parting plates that transfers heat from one channel to the other, these typically vary between 0.8mm and 2.0mm [2], the mesh variations can be seen in figure 3.10.

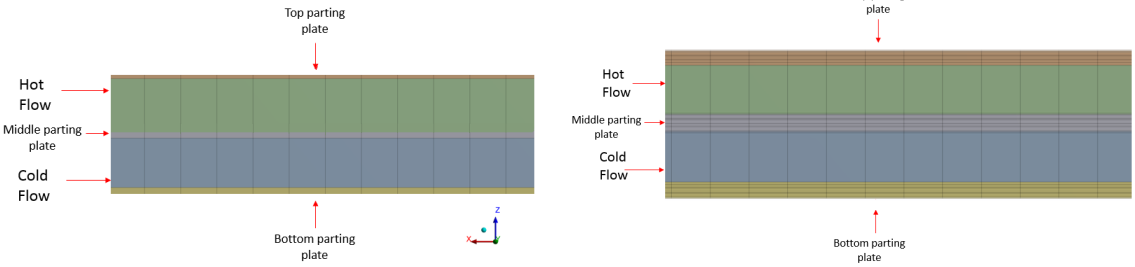

(a) Mesh with 1 cells in transverse direction of parting plate.

(b) Mesh with 4 cells in transverse direction of parting plate.

Figure 3.10: Mesh Settings for parting plates in porous model.

The results of the convergence study is presented in figure 3.11.

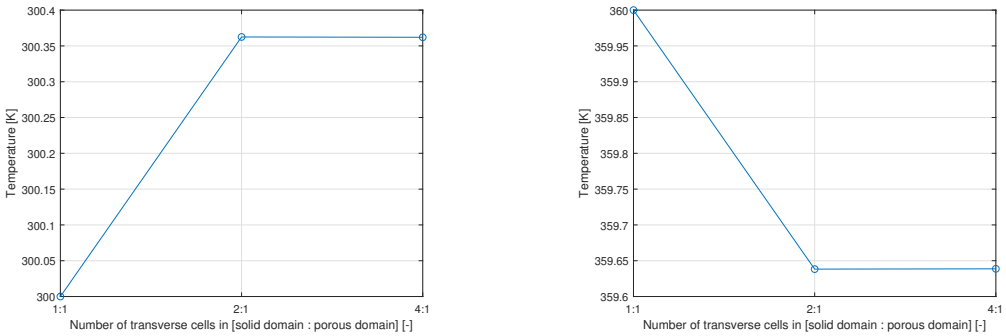

(a) Steady-state temperature at cold inlet/hot outlet of parting plate.

(b) Steady-state temperature at hot inlet/cold outlet of parting plate.

Figure 3.11: The effect of cell heights in porous domain on temperature at the either ends of the parting plate.

From figure 3.11 one may again see that only a small temperature difference, occurring in the first mesh refinement from 1 to 2 cell in the parting plate, with any further refinement having negligible impact of the result. To conclude the mesh convergence the final mesh setup consists of both porous and solid domains with 2 cell heights and cell length of 50mm in streamwise direction. Using this configuration results in 28888 nodes and 18700 elements for the two channels. Scaling this up to the large scale geometry consisting of approximately 200 channels it is estimated that approximately 3.5 million elements will be required.

3.1.3. Fin model validation

In order to justify the use of porous media to model the fins of a PFHE a validation of the fin model was carried out. This was done by determining an analytical solution for a counter-current PFHE using the *number of transfer units* method also termed *NTU-Method*. Next to the method using the logarithmic mean temperature difference the NTU-method enables the determination of the duty ($\dot{Q}$) without knowing the temperatures of the streams leaving the heat exchanger. The details of the method can be found in any literature concerning heat transfer and heat exchangers, in this case reference has been made to Wagner [53]. Fundamentally the method is based on defining what is called a heat exchanger effectiveness defined in 3.18

$$\epsilon = \frac{\dot{Q}}{\dot{Q}_{max}} \tag{3.18}$$

To theoretically achieve $\dot{Q}_{max}$ the minimum heat capacity is required with the maximum possible temperature difference which would be obtained from the difference between the hot inlet and the cold inlet temperatures. Thus an expression for maximum duty is defined as in equation 3.19.

$$\dot{Q}_{max} = C_{min}(T_{Hot_{in}} - T_{Cold_{in}}) \tag{3.19}$$

The actual duty will be lower and can be determined by multiplying by a correction factor which is the aforementioned effectiveness ϵ. The effectiveness is either determined graphically from NTU vs ϵ graphs, or from formulas usually based on an exponential function. Which formula to use depends on the heat capacity ratio of the two streams. The simplified test case simulated for the validation consists of air passing through both channels in a counter-current arrangement at the same velocity and with constant material properties (see table C.1 for complete settings of the model). Thus the ratio of heat capacity will be 1 and for this special case equation 3.20 is recommended in [53].

$$\epsilon = \frac{NTU}{1 + NTU} \tag{3.20}$$

In which the *NTU* as in equation 3.21 is determined using the overall heat transfer coefficient *U*, heat transfer area *A* and the minimum of the two heat capacities C_{min} which can be that of either stream since they are identical.

$$NTU = \frac{UA}{C_{min}} \tag{3.21}$$

For the boundary conditions used to validate the fin model the equations described in this section enabled a calculation for the duty of the heat exchanger, this duty was found to be 230W. In order to compare this with the CFD calculation the thermal conductivity of the solid was reduced in order to cancel out the 3-dimensional conduction which is not accounted for in the *NTU*-method. Once the steady-state solution was run the outlet temperatures of one of the streams was used to calculate the duty from an energy balance for one of the streams as in equation 3.22.

$$\dot{Q} = \dot{m}h(T_{coldout} - T_{coldin}) \tag{3.22}$$

Comparing the two shows that a discrepancy between the simulation and analytical solution of approximately 3% is present using the mesh with 18700 cells.

3.1.4. Timestep convergence study

As of yet all computations regarding the mesh convergence were computed for a steady-state case. However ultimately the interests of the project concerns the start-up operation of the PFHE and since this is a highly dynamic process a transient simulation will be required. The transient simulation will require to take one more factor into consideration namely the timestep. Selecting a timestep that is too large will lead to numerical instability as well as reduce the amount of the transient phenomena that will be captured. Selecting a timestep that is too small on the other hand will increase computational time without gaining any additional details. To this end it is often useful to define a criteria to which the timestep may then adapt to. One such a criteria is the Courant number as defined in equation 3.23.

$$Cr = u\frac{\Delta x}{\Delta t} \tag{3.23}$$

Where u is the velocity, Δx is the grid spacing and Δt is the timestep. In its current formulation the Courant number contains information about the fluid dynamic properties of the flow namely the velocity. However for the purposes of this model the fluid dynamic properties remain mostly irrelevant since these have been included in the porous model in the form of pressure/friction correlations and heat transfer correlations. Thus an alternative criteria for timestep selection is proposed. A *thermal Courant* number which instead of depending on flow velocity depends on the thermal characteristics of the material which is defined in equation 3.24.

$$Cr_{Thermal} = \frac{\alpha}{\tilde{L}} \frac{\Delta x}{\Delta t} \tag{3.24}$$

Where α defines the thermal diffusion and depends on the material properties of the solid as defined in 3.25 and $\tilde{L}$ is a characteristic length scale, which in this case is the volume to area ratio of the heat transfer surface.

$$\alpha = \frac{\lambda}{\rho_s c_{p,s}} \tag{3.25}$$

Making use of this criteria enabled to increase the timestep by a factor of approximately 60 when compared to the original Courant number. This will enable significant savings in terms of computational time without impacting the resultant temperatures. To validate this approach, the metal temperatures using the timestep obtained from the *thermal* Courant number is compared to two other, smaller timesteps, corresponding to the traditional Courant number in figure 3.12.

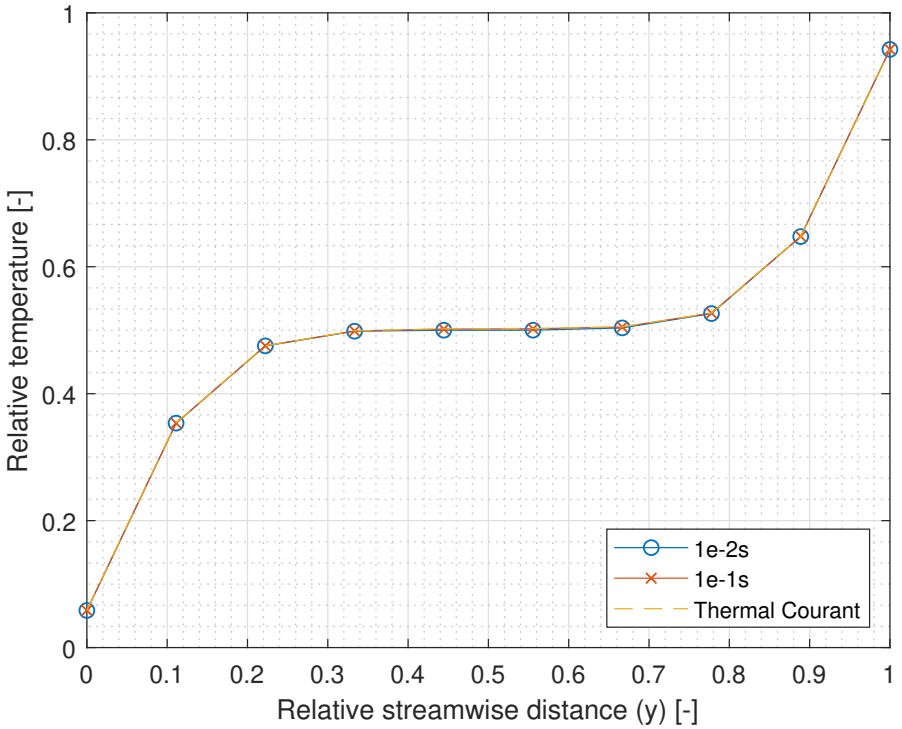

Figure 3.12: Comparison of different timesteps from transient simulation.

3.1.5. Mesh convergence study CSM

Similarly to the CFD simulation the CSM simulation results could be impacted by the mesh used. For this reason it was necessary to conduct a mesh convergence study in order to guarantee a mesh independent solution. Factors in which the mesh may influence the solution could occur in two instances, firstly if the mesh is significantly different to the CFD mesh the temperature mapping may become more prone interpolation errors as thermal data is transferred from the mesh nodes in CFD to the mesh nodes in CSM. Secondly the resolution of the mesh will have a direct impact on the nodal displacements and by extension the equivalent stress computed by these displacements.

Temperature mapping

Firstly the effect of the finite element mesh on the accuracy of temperature mapping was investigated. Due to the relatively simple geometry a hexahedral mesh was used implementing the SOLID186 element from the Ansys element library. This is a hexahedral element with 20 nodes one at each vertex and the remaining ones along it's edges as seen im figure 3.13.

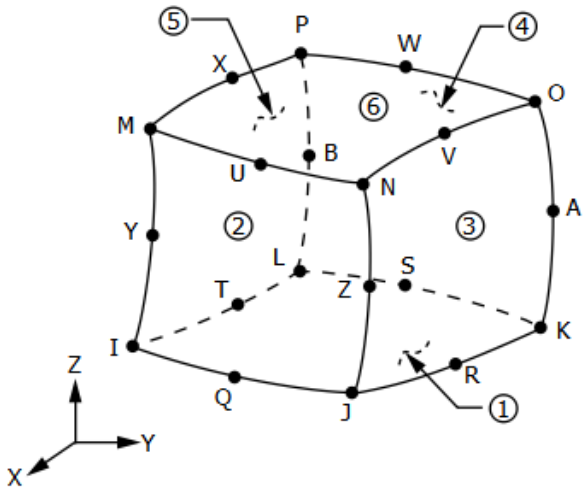

Figure 3.13: Hexahedral SOLID186 element geometry [3].

Similarly to the CFD mesh convergence study the edge length of the elements were varied this time however the entire temperature profile along the parting plate is compared instead of just at the ends. Temperature data at points on a line along the middle of the parting plate between the two channels were taken for each of the mesh settings the results of which can be seen in figure 3.14.

Figure 3.14a show the effect of the CSM mesh on the mapped temperatures. On first glance it can be concluded that the mapped temperatures for all the meshes are very close to one another with a maximum temperature difference of just under 1 K. This trend can be better appreciated when looking at the mapped temperature comparison of the 500mm and 5mm meshes in figure 3.14b. Secondly what becomes noticeable are the sudden temperature jumps for some of the meshes. These jumps seem to occur in the finer meshes which interpolate more between the nodes thus exhibiting these short zig-zag patterns, in contrast to this the larger meshes particularly the 500mm and 200 mm meshes do not show this behaviour instead a more wave like pattern occurs which is due to the relatively few interpolation points causing these longer, more constant gradients. Finally very good agreement between the 50mm meshes of the CFD and mapped CSM temperature profiles can be seen in figure 3.14c. Maximum temperature differences occurred at either ends of the parting plate, reaching a maximum temperature difference of just under 2K.

In conclusion it can be said then that overall temperature mapping is not a particular issue even with the different node counts from CFD to CSM and varying mesh density has negligible effect of the resulting mapped temperature. This is confirmed at least qualitatively in figure 3.15 which compares the mapped temperatures for the very fine mesh in figure 3.15a and the coarser 200mm mesh in figure 3.15b with both showing no significant differences. For details on how the data transfer is carried out reference can be made to the appendix B.

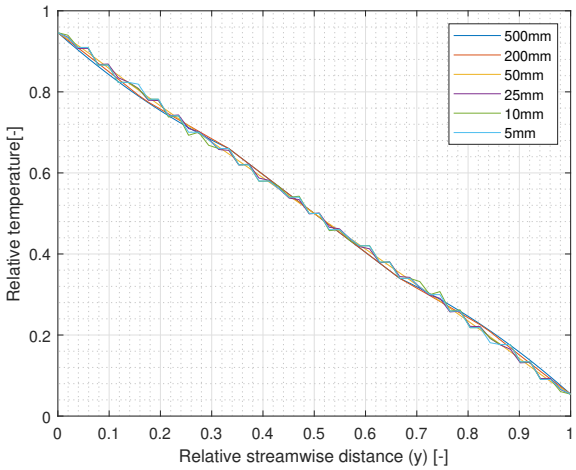

(a) Mapped temperature profile along the length of the parting sheet in FE Mesh for different cell lengths.

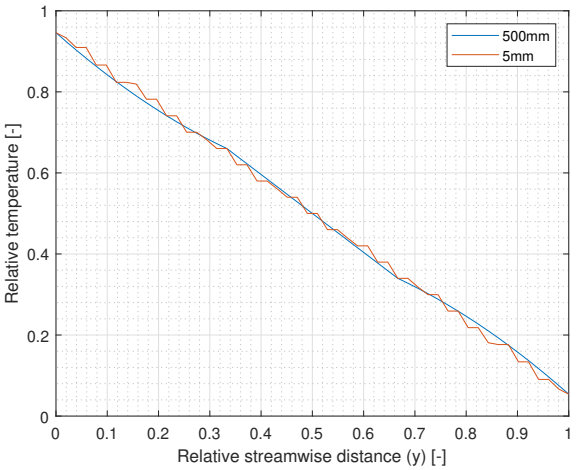

(b) Mapped temperature profile along the length of the parting sheet in FE Mesh for cell lengths 500mm and 5mm.

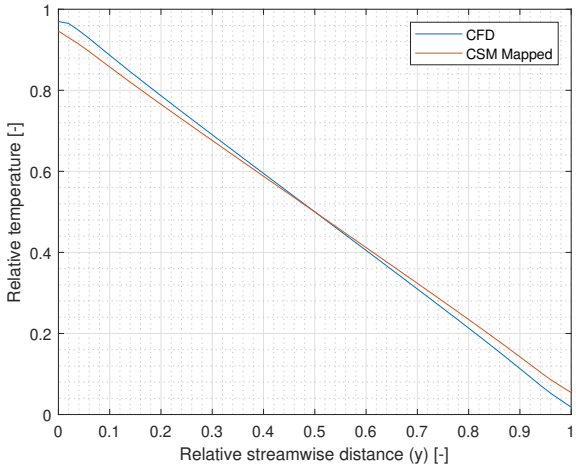

(c) Comparison of CFD and mapped CSM temperature profiles

Figure 3.14: Mapped temperature profiles of middle parting plate for different CSM meshes.

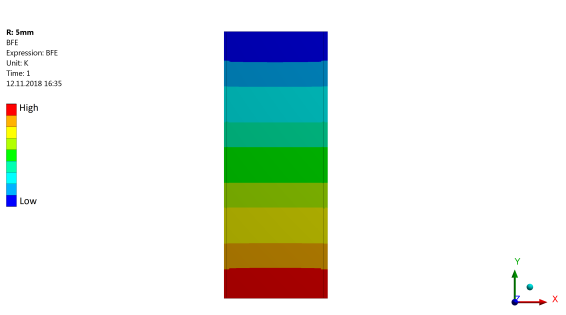

(a) 5mm.

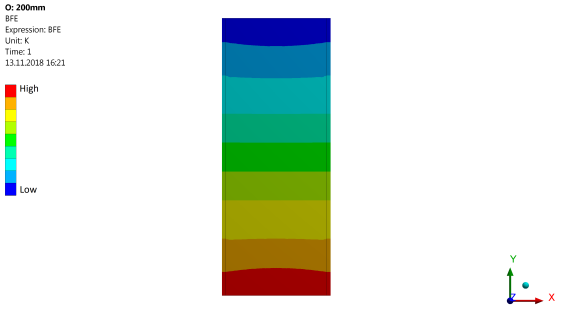

(b) 200mm.

Figure 3.15: Comparison of the mapped temperatures on parting plate and side bars for a coarse (200mm) mesh and a fine (5mm) mesh.

Equivalent stress convergence

Next the effect of the mesh on the stress results are investigated. For this the same mesh lengths will be compared and areas of maximum stress in the structure will be identified. The maximum stress areas will be used as reference points in order to determine how the mesh density will affect these regions. Initially stresses were computed using the coarse mesh of 200mm, the stress distribution along the top parting plate is depicted in figure 3.16a.

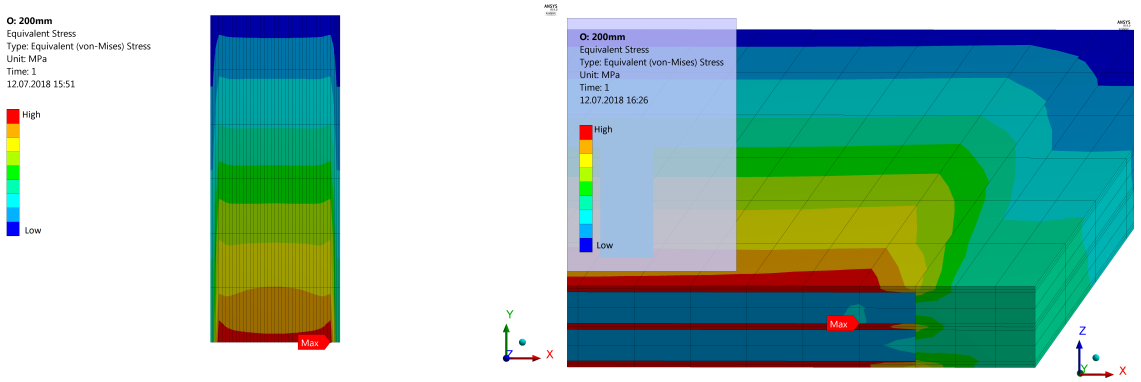

(a) Equivalent (von-Mises) stress distribution across the top parting plate in the two channel model

(b) Equivalent (von-Mises) stress distribution at the hot inlet in the two channel model.

Figure 3.16: Equivalent (von-Mises) stress distribution in the two channel model

Unsurprisingly the maximum stress occur on the side of the hot inlet since the temperature difference between this end of the channel and the the initialized solid temperature is greater to that at the cold inlet side. Specifically these peak stresses occur on the parting plates near the side bars. This region was taken as a reference point at which the other meshes will be compared to. Figure 3.16b shows the stresses in this region for the coarse mesh.

Using this as a reference point the maximum stresses of the other meshes were recorded and plotted in 3.17.

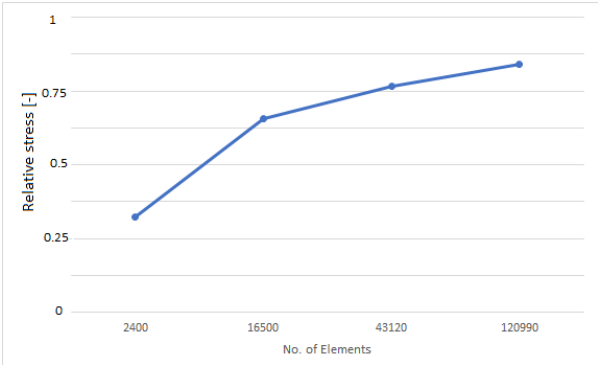

Figure 3.17: FEM Mesh convergence study.

Although continuing to increase the mesh density still has an impact on the maximum stress observed the change in stress per additional element is relatively small. Based on this the mesh corresponding to 16500 elements was deemed sufficient.

3.2. Full Geometry

3.2.1. Geometry description

Having conducted the preliminary studies concerning the mesh and timestep an attempt is made to implement the two channel model for two modules of the PFHE. A module is defined as one core block consisting of fins separated by parting plates, one such block can be seen in figure 3.18.

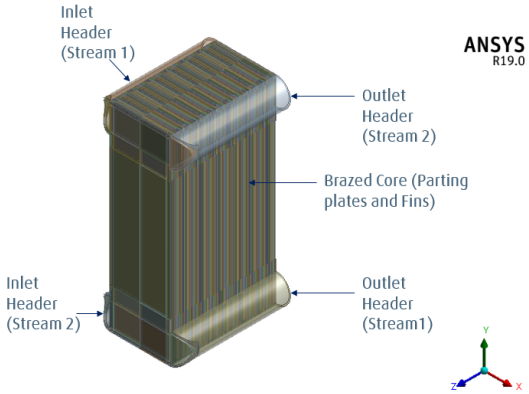

(a) 3D Model of single module from a PFHE.

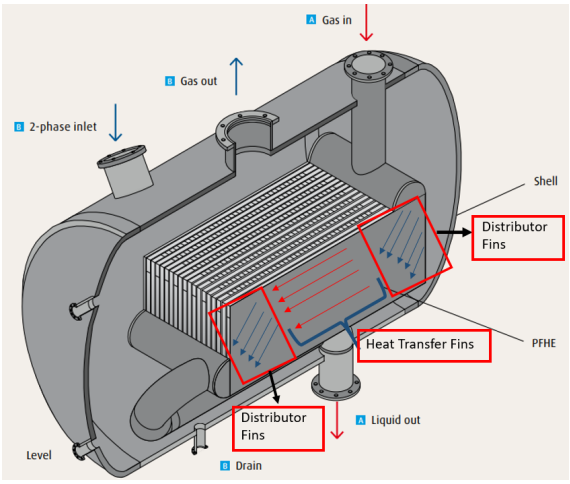

(b) Side view depicting fin types in a PFHE as seen in Linde [32].

Figure 3.18: Complete layout of a single module PFHE (left). Outline of a single channel (right).

Figure 3.18a is representative of a single module of the PFHE which consists of two inlet and two outlet headers each responsible for their respective streams. These are connected to a single brazed block made up of fins which alternate between stream 1 and stream 2, separated by parting plates responsible for the heat transfer between the channels. In reality a typical fin channel contains a variety of fins each affecting the properties of the flow. For simplicity figure 3.18b shows one of the channels divided into different fin regions. The flow initially enters the header which provides a space to collect the fluid and enables distribution to the inlet of the first set of fins. These initial fins are termed distribution fins and serve to direct the flow to the main fin region which in 3.18b is the location containing the heat transfer fins often termed the active fins. As the name suggests these fins aim to maximise the heat transfer and for this reason the fin density in this region of the PFHE is more concentrated in an effort to increase the heat transfer area. After that the flow enters a final set of distributor fins which direct the flow to the outlet header responsible for collecting the fluid again. While the general model is based on figure 3.18 some simplifications were made. Instead of only including one brazed core the model will consist of two brazed core modules stacked on top of each other and connected to one another at each end. Furthermore the headers were removed and the distribution fins at either end of the channel were replaced by heat transfer fins thus the assumptions are outlined below.

- the flow from the header is ideally distributed along the inlet fins.
- the headers role as a thermal mass is negligible.
- the flow is unidirectional within the entirety of the channel length.

The 3D model to be simulated is presented depicted in figure 3.19.

3.2.2. Simulation setup

The following part will provide a description of the scenario that is to be simulated. Additionally the boundary conditions and models used to mimic this process will be discussed.

Simulation Scenario

The scenario to be simulated is supposed to capture the start-up operation of a PFHE to be used in

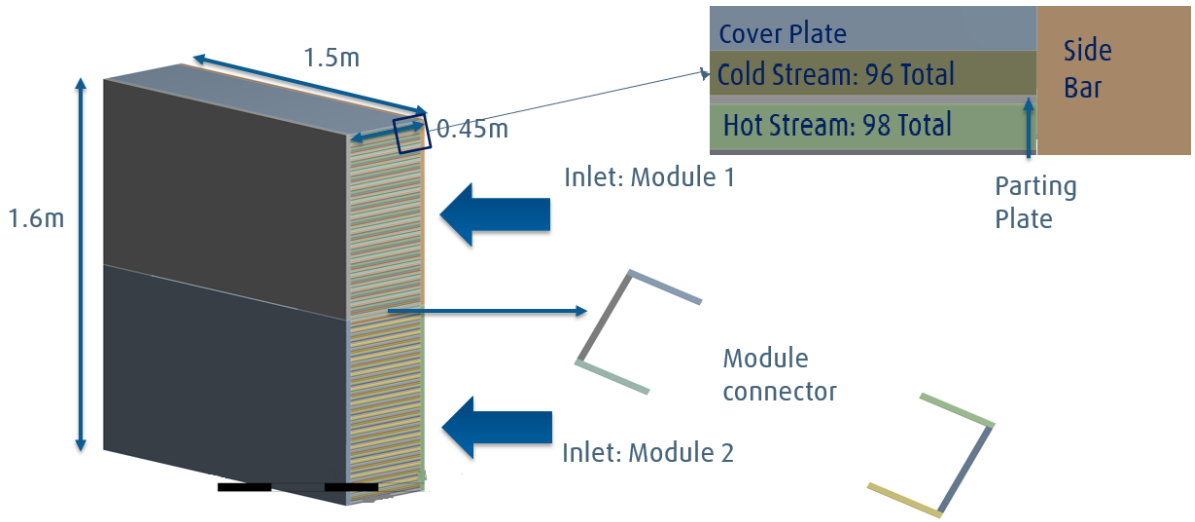

Figure 3.19: 3D Model of 2 module PFHE.

air separation units (ASUs). Specifically this will consist of single phase, Nitrogen (N_2) gas at approximately -177°C passing through stream 1 while stream 2 is unoccupied. The 2 modules are initialized at 50°C and the duration of the process is set to last 500s before the cold stream is shut off again. This scenario is based on a test rig of the PFHE which can be refereed to from the work by Haider et al. [18].

Boundary conditions and models: Fluid solver
Having described the start-up conditions which are to be simulated the next step is to introduce the numerical setup of the simulation. Table D.1 found in the appendix provides details as to the boundary conditions used, models implemented and the solver settings.

To begin with boundary conditions must be set onto the mesh these will be based on the start-up operation of the PFHE. During start up the entire model is initialized at 50°C, once the simulation commences only one stream in both modules is active while the other stream is at rest. After approximately 500s the active stream which will be referred to as the cold stream from here on out is terminated and the alternate counter-current flow stream (which will be called the hot stream) is triggered [18]. For the purposes of this assignment only the cold, start-up period of 500s will be simulated. Thus in order to effectively define the problem thermal as well as fluid boundary conditions must be defined appropriately as seen in table D.1.

The remaining channels in the heat exchanger namely the dummy and hot streams where there is no flow were initially computed by applying the porous media model and setting the inlet velocities to zero. However using these settings lead to unphysical results and eventually failure of the solver. In order to remedy the problem inlet and outlets to these streams were replaced by walls. This however also resulted in highly unstable solutions, producing unsatisfactory convergence, moreover significant imbalances were discovered in the energy equations for the unoccupied fins. An alternative approach is used in these channels specifically these regions are modelled by solid blocks who's material properties are modified to resemble the fins. The justification of such a simplification stem from the reasoning that in the channels where no flow is forced through convective heat transfer will consist of natural convection driven by the temperature variations of the parting plates above and below the fluid. The heat transfer via natural convection will clearly be negligible in comparison to thermal conduction occurring between the fins and the parting plate due to the large surface area provided by the fins. Additionally the flow caused by natural convection would require significant mesh refinement in order to capture properly. This is thought to be the reason why such poor convergence was found. The altered properties of the solid block include the density, specific heat capacity and thermal conductivity, all of which were multiplied by a correction factor based on the fluid to solid fraction defined in the porous medium.

Boundary conditions and models: Solid solver

Similarly to the porous media used in the CFD simulation to model the complex fin geometry a similar approach is used in the mechanical simulation. Instead of including the fins a continuous metal block is inserted whos mechanical properties have been changed to reflect deformations of this fins. Namely this was done by multiplying the original elastic modulus of aluminium by the solid fraction calculated from the fin geometry, this method is explained in more detail in the patent by Hölzl [20]. Next a description of the constrains set onto the model are discussed. Due to scale of the 2 modules the boundary conditions for the CSM simulation must be reconsidered. The walls of the modules cannot simply be held in place via fixed boundary condition since in reality the outer walls of the heat exchanger are able to expand or contract in all three direction. Imposing a fixed boundary condition would therefore create stress loads at locations where in fact no such stresses exist. While this would be an example of overconstraining the model, some constraints must be set in order to conduct a stress computation. After some thought a method was developed in which constraints could be placed on the geometry without overconstraining it. This is done by applying displacement boundary conditions onto specifically selected nodes. These constraints are presented in figure 3.20.

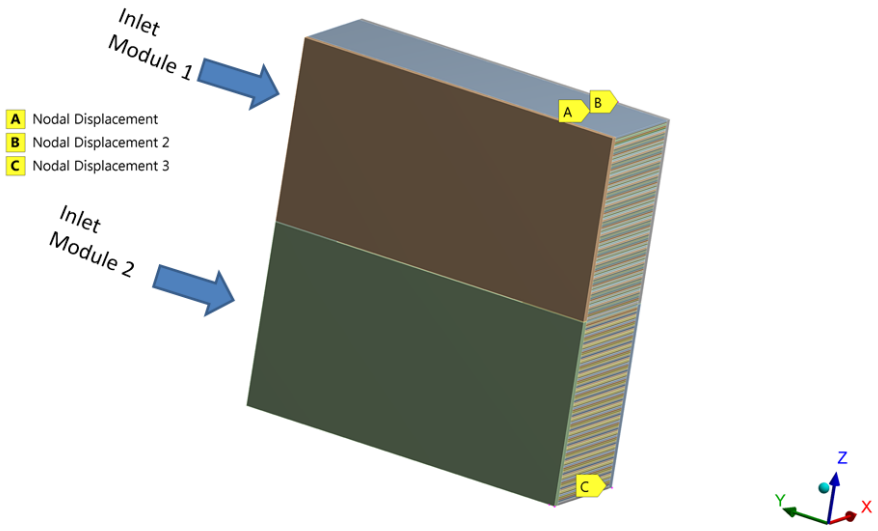

(a) CSM model of 2 module PFHE. x and y nodes at locations A and B. z nodes at location C

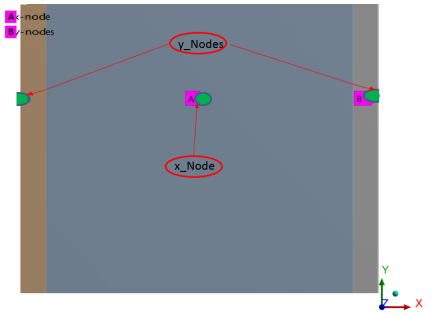

(b) Geometric constraints in x- and y-direction at the top of the upper module.

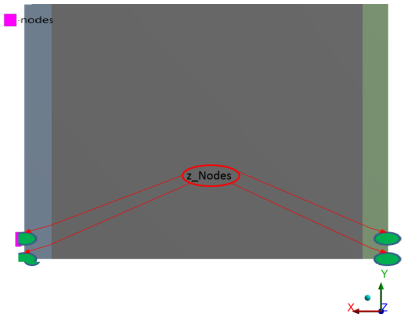

(c) Geometric constraints in z-direction at the bottom of the lower module.

Figure 3.20: CSM Boundary Conditions

Each of these nodes are constrained in a specific direction, the X node is constrained in the x-direction while allowed to move freely in y- and z-directions, similarly Y and Z nodes are constrained in y- and z-direction respectively and can move freely in the other directions.

3.3. Results and Discussion

Having modelled the fins with porous media and implementing this model onto the large scale PFHE geometry results were obtained describing both the thermohydraulic behaviour from the CFD simulation as well as the resulting displacements and stresses from the CSM simulation.

3.3.1. Thermohydraulic behaviour

To begin with the results obtained from the CFD analysis describing the thermohydraulic behaviour of the PFHE will be discussed. This part will deal with the 3D transient temperature distributions in the PFHE focusing on metal temperatures at different locations in the brazed core. To conclude a comparison of the 3D CFD model is made to the currently employed 1D model.

Streamwise temperature development

Firstly the streamwise temperature development in the PFHE will be looked at. Figure 3.21 shows contour plots of the temperatures in the parting plate and side bars at different times.

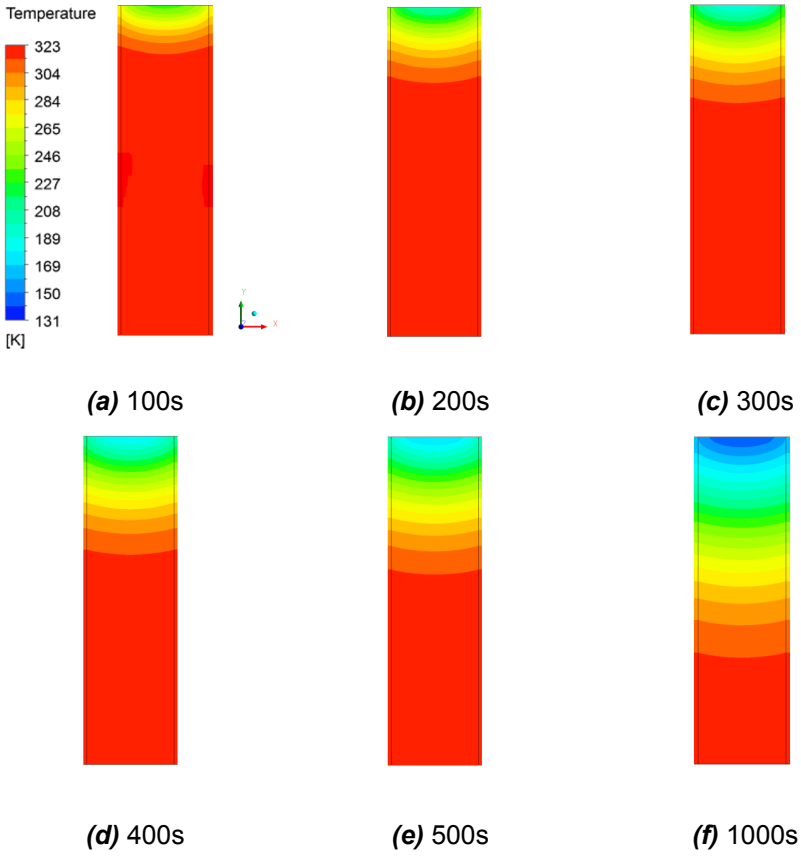

Figure 3.21: Streamwise contour plots of transient temperature development in parting plate and side bars located centrally in one of the modules.

Figure 3.21 indicates that within the duration of the test run of 500s the temperature profile in the parting plate varies highly in the first half. A maximum temperature difference of approximately 200K across a distance of just under 750mm is specifically seen while the remaining section of the parting plate is unaffected by the incoming flow as the bottom half in figure 3.21e retains the initial temperature of 323K. Even after 1000s there are still some parts which retain the initial temperature as seen in the contour after 1000s (see 3.21f). Furthermore the temperature exhibits a parabolic profile despite the flow entering the channel as a plug flow. This effect is best seen at the inlet of the flow which illustrates how the side bars, due to their higher thermal mass are lagging behind. The effects seen in the contour plots for one of the parting plates are reflected in figures 3.22 which show the streamwise temperature variation at different timesteps at three different locations in the brazed core.

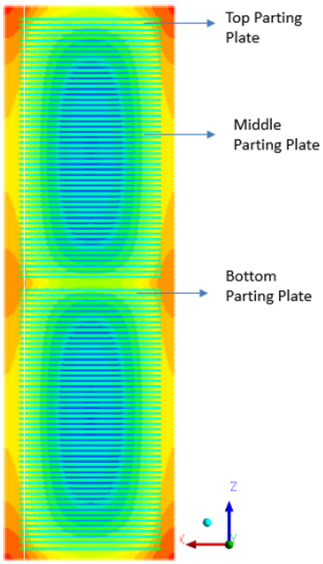

(a) Locations of the parting plates to be compared.

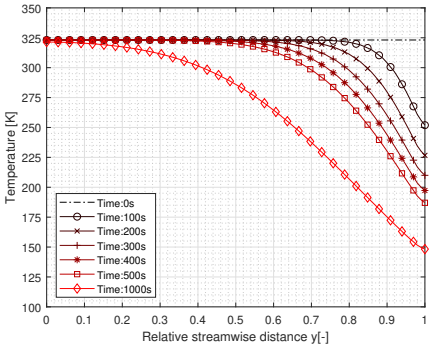

(b) Top parting plate

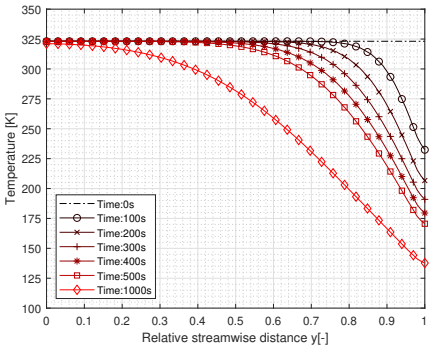

(c) Middle parting plate.

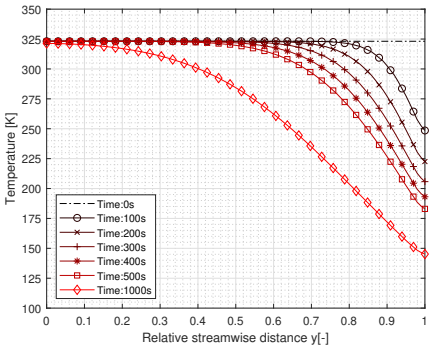

(d) Bottom parting plate.

Figure 3.22: Streamwise transient temperature development for parting plates at different location in the brazed core.

In figure 3.22 the stream enters the modules on the right hand side at y=1.5m which to relates to a relative length of 1 in the figure. After just 100s the parting plates experience a large temperature drop which varies depending on the location within the brazed core. Figure 3.22b shows the top plate, which undergoes the smallest temperature drop out of the three locations with a maximum temperature drop of about 68K. The largest change in temperature is witnessed in the middle of the block (see 3.22c). Here the parting plate undergoes a drop of approximately 90K at the inlet within the first 100s. The reason for this difference is thought to be the cover plate at the top and bottom of the modules which have a greater thermal mass relative to the parting plates. This as well as the adiabatic boundary condition set at the outer surface of the cover sheets is thought to be the reason why the parting plate in close proximity to it is able to retain more of its heat. Although a cover sheet is also located at the top of the second module the parting plate here is slightly cooler as seen in figure 3.22d which shows a maximum temperature drop of about 73K in the initial 100s. The reason for this is likely the module connector which affixes the two modules via their cover plates and is in thermal contact with the bottom cover plate this causes more heat to be directed away from this parting plate. Nevertheless due to the small surface area of the module connector a difference of only 5K is seen here when compared to the temperature of the top parting plate. Another item to note is that even after the intended running time of 500s the core of the block has still not achieved a homogeneous temperature. In fact far from it comparing temperatures at 500s for the three locations still show variations of just over 15K between the top and middle parting plate, with these two locations only 400mm apart this may still impact the

structural integrity in the brazed core. For curiosities sake the CFD computation was continued for 1000s to see if the onset of a steady-state is even close, and as seen for any of the three graphs in figure 3.22 this is certainly not the case with temperature differences of about 7K still present near the inlet.

Figure 3.23 compares different layers to one another. For this a cold fin layer and the adjacent parting plate and hot fin layer located at the centre of one of the modules are chosen as seen in figure 3.23a.

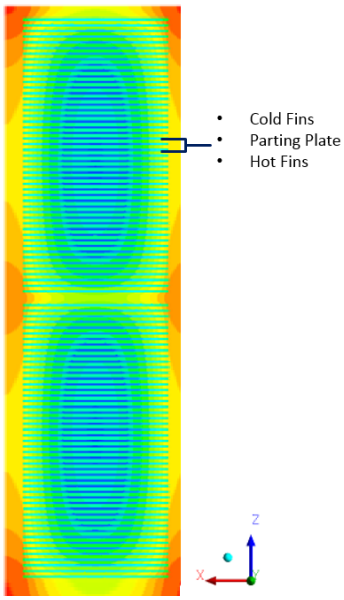

(a) Locations of the layers to be compared.

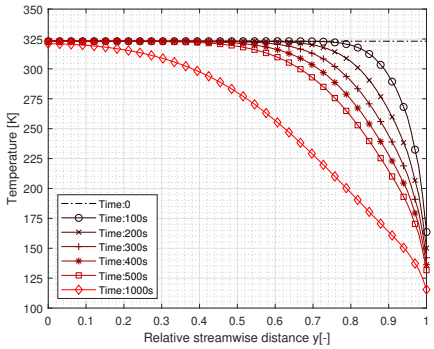

(b) Cold fins.

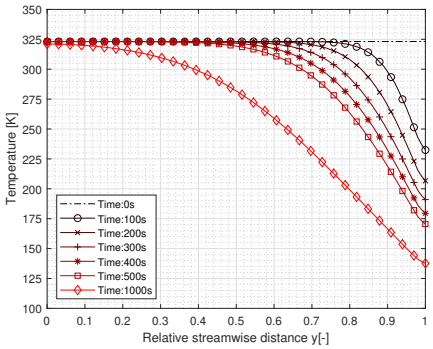

(c) Parting plate.

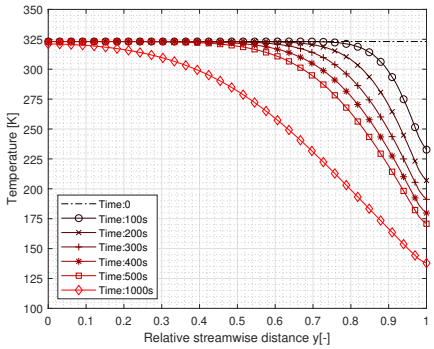

(d) Hot fins.

Figure 3.23: Streamwise transient temperature development of cold fins, parting plate and hot fins located centrally in one of the modules.

Examining the parting plate and hot fin layer from figures 3.23c and 3.23d respectively show that virtually no temperature difference between these two layers exist. This is not too surprising since the hot fins don't have anything flowing through them. In contrast to this however the cold fin layer maintains a temperature difference of about 20K directly at the inlet when compared to the other two layers. The consequence this may have from a mechanical perspective is that the brazing which connects the fins to the parting plate may be prone to crack propagation due to the differences between the low fin temperatures of the cold stream and the relatively high temperature of the parting plate. While such large temperature difference are observed at the inlet this trend does not continue further into the core. Comparing figures 3.23b and 3.23c 100mm away from the inlet corresponding to a relative distance of 0.85 will see a reduction of temperature difference of about 10K. Further away still at 200mm (relative distance of 0.7) the three layers converge to the same temperature.

Transverse temperature development
So far the temperature in streamwise direction have been presented for the different streams, however in terms of the stress analysis it is also important to understand the temperature developments in the x-direction, transverse to the flow. In an effort to determine this, planes at various distances from the inlet have been taken as seen in figure 3.24.

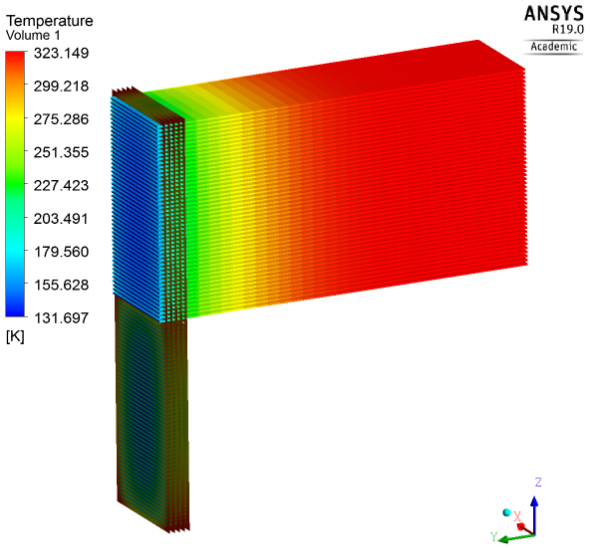

Figure 3.24: Locations of planes taken for the contour plots in figure 3.25.

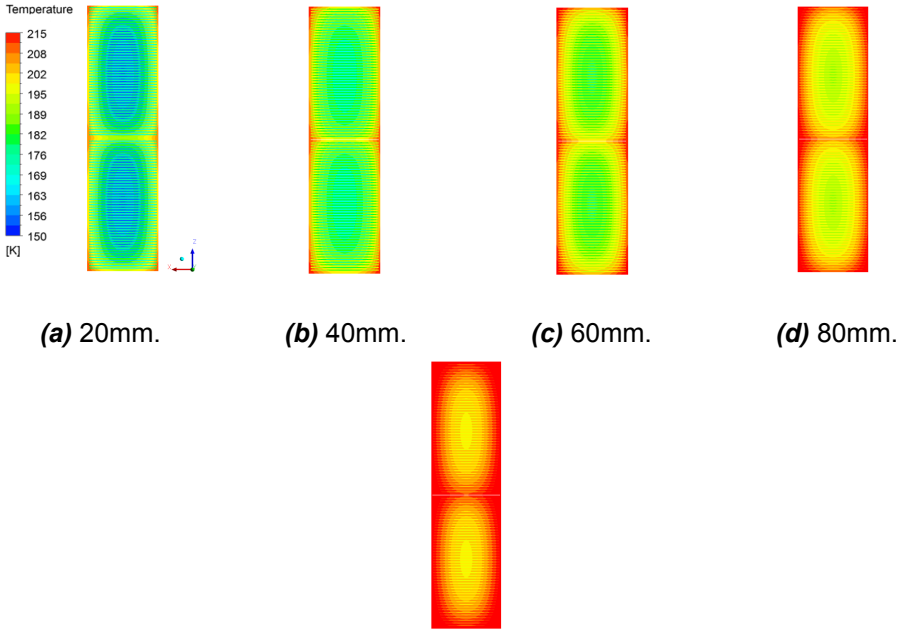

(a) 20mm. ***(b)*** 40mm. ***(c)*** 60mm. ***(d)*** 80mm.

(e) 100mm.

Figure 3.25: Contour plots from planes in figure 3.24.

Figure 3.26 show the transverse temperature distribution of two modules, 20mm from the inlet at different times. Illustrated well here is how the cooling process occurs in the two brazed cores. After the first 100s figure 3.26a reveals how the decrease in temperature initiates at the centre for each of

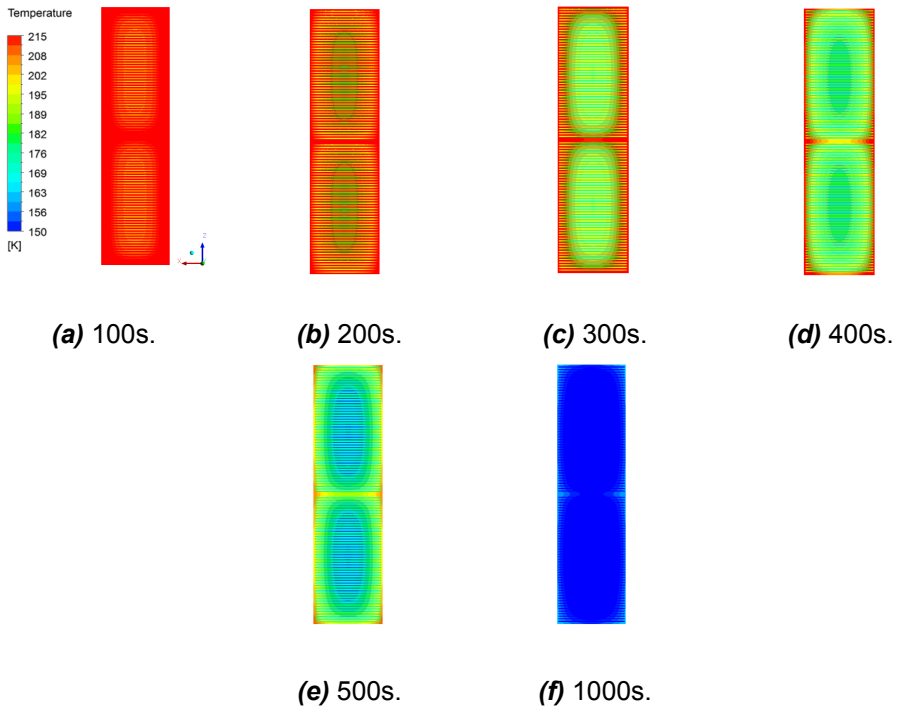

(a) 100s. ***(b)*** 200s. ***(c)*** 300s. ***(d)*** 400s.

(e) 500s. ***(f)*** 1000s.

Figure 3.26: Contour plots from a plane 20mm from the inlet of the cold flow at different time steps.

the modules, this will be due to fact that heat is more effectively retained by the side bars and covers located at either sides of the modules and at the top and bottom of each module respectively since these are constructed of thicker pieces of metal in contrast to the relatively thin parting plates. Additionally the large surface area of the fins will significantly influence the increased rate of cooling at the centre. The increased retention of the heat is best seen in figures 3.26c and 3.26d which now depict how the colder temperature has spread through all the fins and parting plates but there is still a clear difference between this core region and the side bars and cover plates. Moving further along in time in figure 3.26e one can see that after 500s the maximum temperatures are isolated in the top corners of the upper module and the bottom corners of the lower module with another high temperature region appearing at the sidebars near where the two modules connect. Moving further to 1000s a steady-state is still illusive only 20mm into the heat exchanger since there still exists a difference in the side bar temperatures and the core.

Beyond contour plots the transverse temperature profiles at different y-distances away from the inlet are presented graphically in figure 3.27 which again show that the lowest temperatures are located at the centre of the brazed core, with the peak temperature for each timestep occurring consistently at either ends where the sidebars are located. Figure 3.27a corresponds to the contour plots shown previously in figure 3.26 representing the temperature 20mm away from the inlet. This shows that after 100s a temperature difference between the core and side bars of about 37K exists. Though this temperature difference decreases as time passes by, after 500s a temperature difference of 25K is still observed. As expected further into the brazed core of the module the initialized core temperature is retained more effectively and the difference between the temperatures at the side bar and the centre is reduced which is shown in the remaining figures 3.27b to 3.27f which represent temperatures at distances ranging from 40mm to 525mm away from the inlet. Further results regarding temperature differences between fluid and fin, different parting plates and transverse temperatures at different distances into the brazed core can are presented in figures E.1, E.2 and E.3 respectively in the appendix.

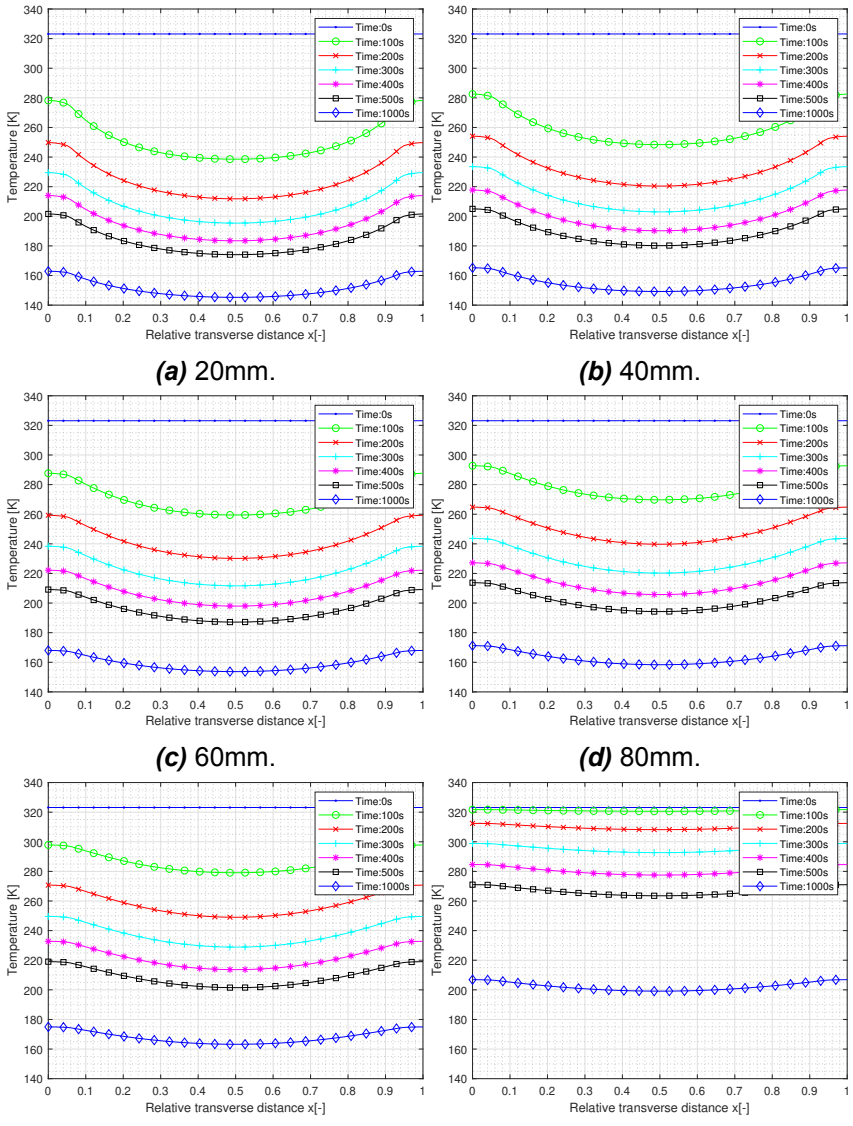

(a) 20mm. ***(b)*** 40mm.

(c) 60mm. ***(d)*** 80mm.

(e) 100mm. ***(f)*** 525mm.

Figure 3.27: Transient temperature development in the transverse direction of parting plate and side bar located in the centre of one module, at different distances away from the inlet. The vertical lines indicate the location of the side bars.

3.3.2. Mechanical analysis

Using the temperature data from the conjugate heat transfer simulation the results of the mechanical analysis will be presented. This will include showing the resulting deformations as well as the locations of the peak stresses which occur in the component holding together the two modules. Lastly stresses in the brazed core area are also analysed which consist of the stresses in one of the parting plates.

Deformations

Illustrated in figure 3.28 is the total deformation of the 2 modules after 500s. The maximum deformation occurs at the top of one of the modules, this corresponds to the areas with the highest temperature from the CFD analysis. Important to note is that although the CFD simulation which shows a symmetric temperature in both modules, the deformations in figure 3.28 do not reflect this. The reason for this is simply due to the boundary conditions set on the CSM solver described previously in this chapter. Put simply the boundary conditions allow the top module to move freely in the z-direction while the bottom module is slightly more restrained in this direction. Never the less the take home message conveyed by the deformations seen in figure 3.28b is that the independent movement of the modules will clearly result in a shearing motion at the points in which the two modules are connected.

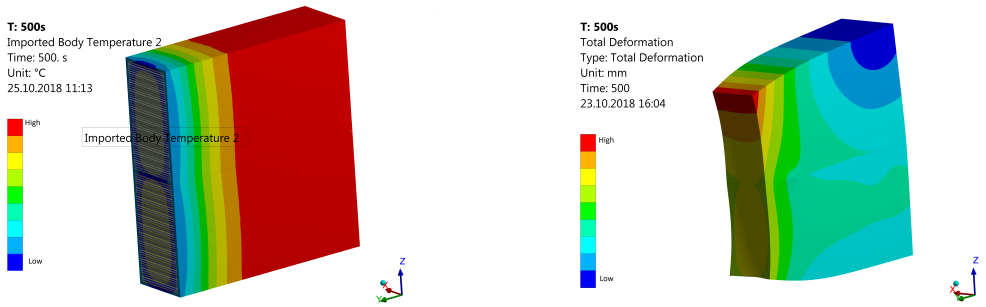

(a) Mapped temperatures. ***(b)*** Deformation scaled up by a factor of 72.

Figure 3.28: Two modules at 500s

Maximum stresses

As seen in the deformations of the two modules previously the maximum stress concentration was found to occur at the point at which the two modules are adjoined. Specifically on the side where the cold stream enters the two heat exchanger blocks as seen in figure 3.29.

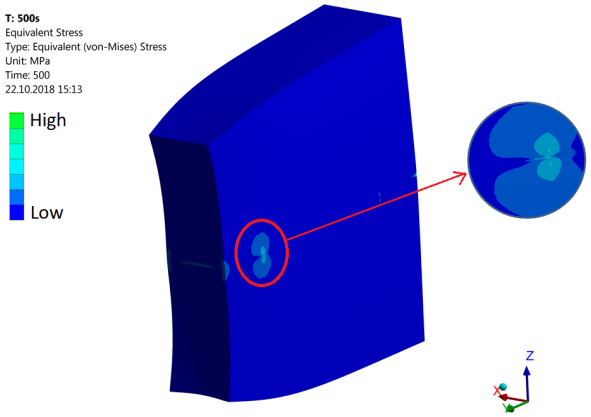

Figure 3.29: Stress concentration located at the interface between the two modules.

Stresses in the core

Having determined the location of maximum stress in the PFHE, the stresses within the brazed core have also been investigated. To this end one of the parting plates and side bars located in the middle of the core has been selected, various locations were investigated which are outlined in figure 3.30a. Figure 3.30c shows the stress distribution along the length of a parting plate in this the flow is considered to start at the 1500mm mark (relative distance of 1), corresponding to the peak stress occurring at 100s. As time progresses the stress in this region decreases by about 50% however further into the PFHE the stresses are observed to rapidly drop off until a constant value is reached as the temperature becomes more uniform.

Next the data presented concerning the transverse stresses from figures 3.30d to 3.30g are discussed. All of which with exception to figure 3.30d show that the maximum stresses occur on the two sides of the parting plate at the interface to the side bars. This is likely due to the large temperature differences between the side bars and the parting plate as described in the thermohydraulic analysis of the transverse temperature distributions. Another commonality is that a rise in stress is observed towards the centre of the parting plate. This conforms to the transverse temperatures in the parting plate and side bar from figure 3.27 which show minimum temperatures occurring at the centre of the parting plate causing greater contraction of the metal here. A difference between the graphs can be seen in the transient behaviour of the stress distribution. Close to the inlet one observes that that peak stresses are reached fairly early on and occur at the centre of the parting plate where the peak stress occurred within the first 100s and gradually decrease with time. The other locations show maximum stresses occurring at different times, which basically indicates the cold front reaching these regions at different times. Another trend noticed is the migration of the peak stresses from the centre of the parting plate to the edges. This can be directly attributed to the location of the highest temperature gradients. Close to the inlet the biggest temperature gradients occur in the parting plate which is most heavily influenced by the incoming fluid. The sidebars however remain largely unaffected and thus exhibit lower stresses. However moving further away from the inlet the temperature in the parting plate becomes more uniform whilst the side bars which were initially unaffected undergo a delayed increase in temperature gradient due to their additional thermal density and hence exhibit the greater stresses as one moves further from the inlet.

Using the information from the stress analysis some conclusions can be made regarding the regions of interest of the two modules of the PFHE. Firstly the impact of the two deforming modules is the key mechanism of the elevated stress region at the site connecting the two modules. Stresses in the brazed core of the respective modules are small in comparison and operate well within the safety of the linear elastic finite element model.

As to the validity of the results while the qualitative information gained from the analysis makes sense and seems somewhat reasonable whiles also holding up to similar FEM calculations done on similar PFHE in the works by Hölzl et al. [22]. However it remains difficult to validate the structural simulation fully since this would require testing the equipment until failure to gain better understanding of the failure modes. Thus the quantitative data should only give an indication of the regions of interest and should be taken with a grain of salt.

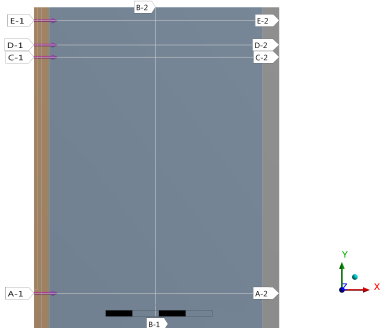

(a) Evaluation regions.

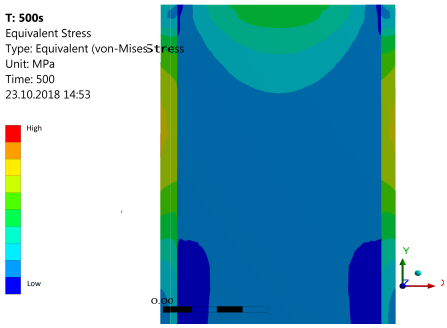

(b) Stress distribution in parting plate and side bars at 500s.

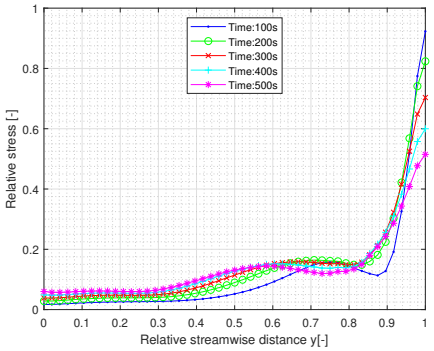

(c) B-1 to B-2.

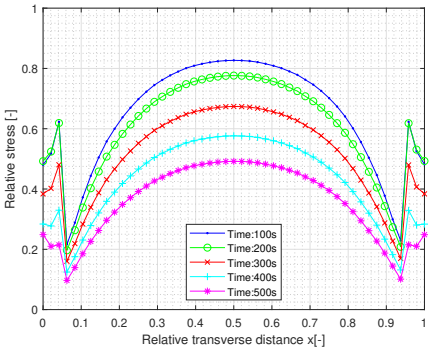

(d) E-1 to E-2.

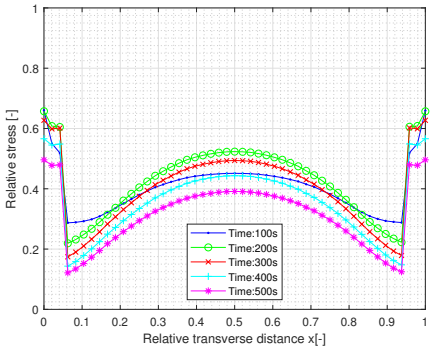

(e) D-1 to D-2.

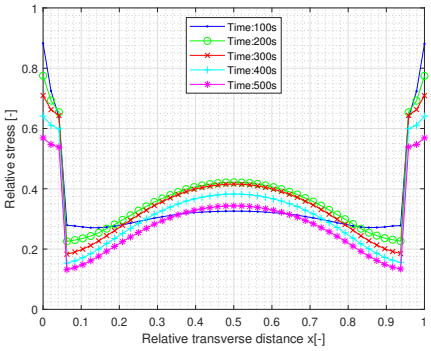

(f) C-1 to C-2.

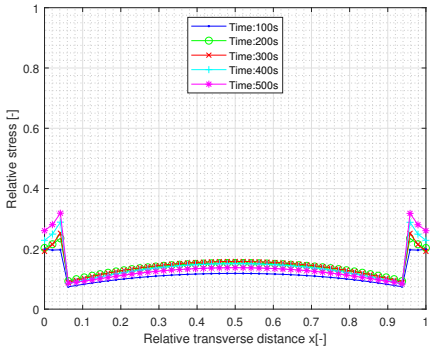

(g) A-1 to A-2.

Figure 3.30: Stress distribution of parting plate in brazed core.

4

Fin Submodel

Using the fin model allowed the simulation of the large scale geometry which in turn enabled the analysis of the global thermohydraulic and mechanical stress analysis in 3-D resolution. As mentioned at the beginning of the previous chapter what cannot be captured by the fin model are the local thermohydraulic phenomena that occur in the fins. For this a geometry and mesh are required that are capable of resolving the details of the flow that occur within the smaller scales at a local level. This chapter will be structured in the following manner. Firstly a description of the geometry to be simulated is provided, secondly a brief summary of sub-modelling used in the area of PFHE. Thirdly arguments regarding the meshing approach are made, followed by the treatment of turbulence and finally the results of the simulation are discussed.

4.1. Fin Geometry

Within a PFHE a variety of fins are included, each with their associated features and properties. Examples of some of the main fin types are given in figure 4.1.

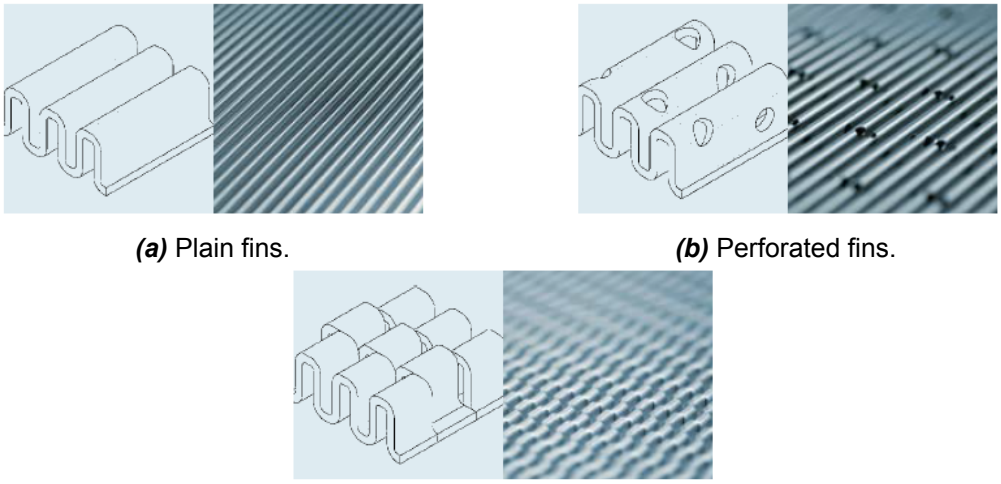

(a) Plain fins.

(b) Perforated fins.

(c) Serrated fins.

Figure 4.1: Fin type commonly used in PFHE as seen in the brochure by Linde [32]

Often fin types are varied within a single stream in order to take advantage of their thermal and hydraulic properties. An instance of this could be for distribution fins, located at the start and end of a the channel. For these often larger, more spaced out fins such as the perforated fins depicted in 4.1b are used in order to reduce pressure drop which will likely be high in this region anyhow due to the re-direction of the flow. A Further example includes streams where the fluid medium undergoes a phase change as it traverses the channel. For such cases perforated bars as depicted in figure 4.2b

are used to accommodate multiphase flow distribution. Figure 4.2a shows the distributor fins marked in red. Fins primarily used for heat transfer are generally unidirectional and prioritize surface area to enhance heat transfer with the drawback of increasing the pressure drops. For this often serrated fins from figure 4.1c or plain fins from figure 4.1a are considered.

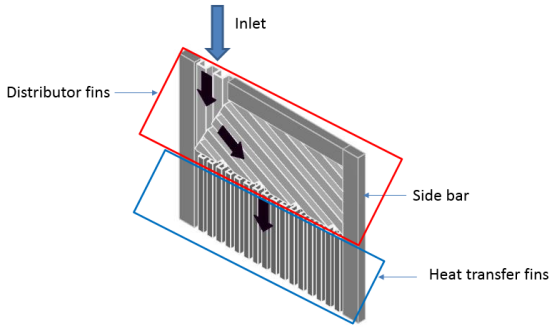

(a) End distributor fins [2].

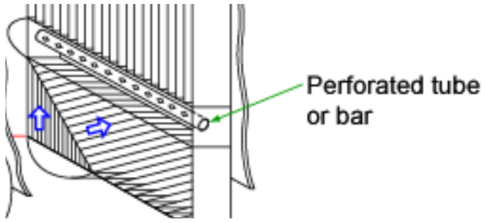

(b) Perforated bar used in two phase flow distribution [2].

Figure 4.2: Strategies for fluid distribution.

The fin type investigated in this project is the perforated fin. The section to be simulated is shown in figure 4.3. Due to the increased geometric detail only a very small section was taken with only about a dozen fin channels being considered per stream. The perforations follow a sinusoidal path with a spacing of a few millimetres between each hole. Similarly to the large scale geometry the scenario to be simulated is the cold stream consisting of the single phase nitrogen gas while the counter-current stream is unoccupied.

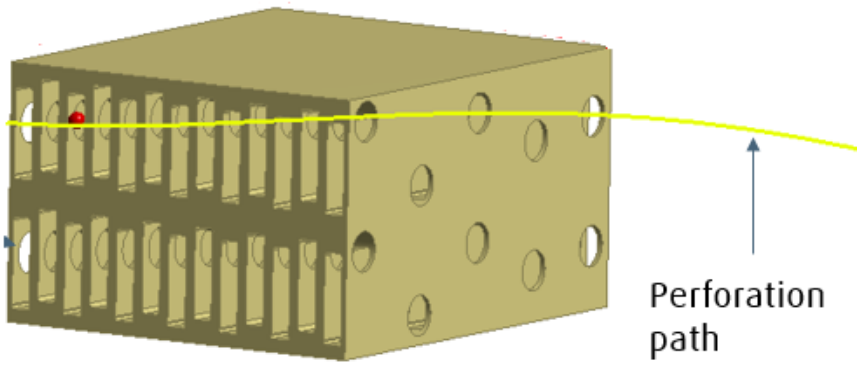

Figure 4.3: Straight section of two channel perforated fins.

4.2. Submodels in PFHE

The creation of a submodel is not at all foreign in the analysis of heat exchangers. Before moving into the details of the model studied in this work a quick review is given regarding areas of applications. Particularly in PFHE, submodels are implemented in order to better understand the local flow and heat transfer phenomena. Some examples of these investigations include the header region leading into the distribution fins which are areas in which fluid maldistribution plays a significant role. The reason for this is due to the sudden expansion of flow area which induces turbulent recirculation regions as seen in the vector plot of a typical header region in figure 4.4.

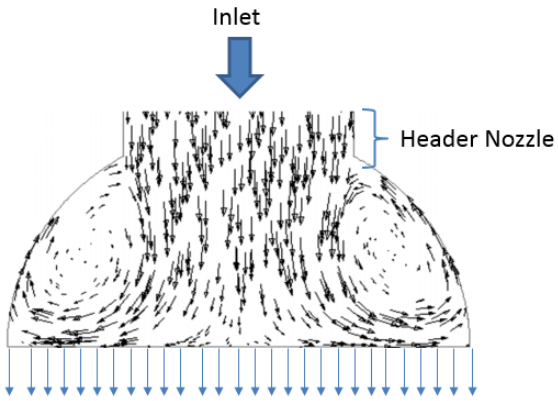

Figure 4.4: Velocity vectors of cross-section for a conventional header [63].

For this reason extensive research in this area has been done in the works of Zhang et al. [63] and Yang et al. [60].
The works by Sheik Ismail et al. [47] studied the flow patterns in serrated and wavy fins and validated the results by comparing the relevant dimensionless group the *fanning friction factor* to other correlations, achieving good agreement of about $\pm 9\%$.
Multiphase flow is also a point of interest since evaporation as well as condensation may also occur in the equipment depending on what fluid medium and operating conditions are used. To this end Yuan et al. [61] performed CFD simulations for two-phase flow distributors similar to the the perforated bar shown previously in figure 4.2b. Apart from flow distribution another area of interest is the simulation of heat transfer in the fins since this a key performance indicator of the entire heat exchanger. The works by Chen et al. [12] and Khoshvaght-Aliabadi [25] build various CFD models each representing different fin types used in heat exchangers for high temperature gas-cooled reactors. Further examples of heat transfer analysis of fins include the works by Bhowmik and Lee [6], Hu and Xiong [23] which looked at temperature distribution in plane fins of a counter current heat exchanger and Zhang et al. [64] who investigated the performance for varying fin wall thickness in terms of heat transfer and performed a structural analysis using the resulting temperatures from the CFD simulation.
The simulation setup which is described in more detail next applies some of the approaches and assumptions from the latterly cited works which focus on the heat transfer analysis.

4.3. Simulation Setup

This part introduces the boundary conditions as well as the numerical setup used in the CHT simulation. Two main assumptions are made for simplicity.

- Flow maldistribution from the header is neglected and flow is assumed to flow evenly and at the same velocity across the entire inlet.
- Pure, gaseous flow is assumed, thus neglecting any maldistribution or effects originating from multiphase flow interaction.

Summarised in table F.3 found in the appendix are the boundary conditions of the simulation and the numerical settings applied. The remaining section will discuss the mesh generation and justify the treatment of turbulence through use of a RANS model.

4.3.1. Mesh

This part introduces the considerations taken in the meshing of the geometry in figure 4.3. Firstly due to the perforations which follow a sinusoidal path it was not possible to create a structured surface mesh at the inlet and sweep this through the entire geometry as would be the common approach. For this reason an unstructured mesh was implemented which consists of mainly tetrahedral elements. Furthermore in order to better resolve the boundary layer of the flow, near-wall refinement was included through the addition of an inflation layer which can be seen at the outer surface of the fluid domain as in figure 4.5.

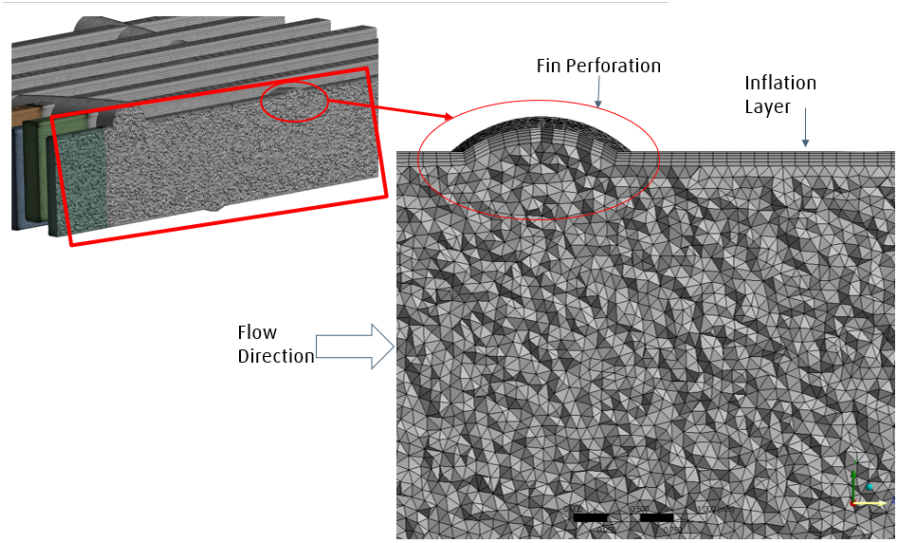

Figure 4.5: Near-wall mesh refinement satisfying $y^+ < 1$.

The near wall refinement is set to follow the perforations in the fluid domain. The cells in the bulk of the flow are given a constant size of 0.1mm while the near-wall refinement is made up of 5 layers with a first layer height set to satisfy $y^+ < 1$ with the growth rate of the following cells set to 1.2 per layer. Such that the entire wall refined mesh is within the viscous sub-layer of the boundary layer.
This being a conjugate heat transfer simulation consideration must also be taken when constructing the mesh of the solid domain. In order to capture the heat transfer taking place between the solid and fluid domain one must ensure that the nodes in the solid and fluid domain are connected, this is illustrated in figure 4.6.

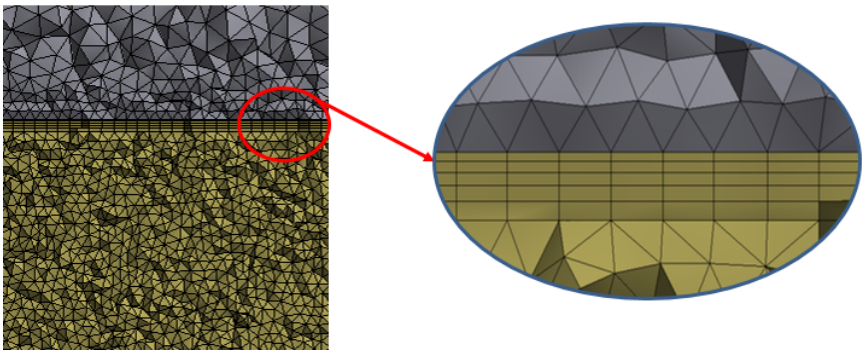

Figure 4.6: Conjugate heat transfer with a magnified view between the fluid domain (yellow) and solid domain (grey).

4.3.2. Turbulence

Due to the complexity of the geometry as well as the relatively large changes in the fluids material properties the flow exists within the transition region to turbulence. In order to confirm this assumption a steady-state simulation was conducted using a low Reynolds number RANS model specifically the k-ω model as detailed in Wilcox [58] for the fluid domain only with constant wall temperature boundary conditions. The k-ω model is generally preferred to the k-ϵ due to the fact that the k-ϵ uses a damping function at the wall for low Reynolds number flows which is non-linear and may cause solver instability. Knowing the hydraulic diameter of the fin as well as the fluid properties of gaseous nitrogen entering the flow domain an inlet Reynolds number could be calculated, this was found to be approximately 1000. Using the definition of turbulent transition in pipe flow as in Schlichting and Gersten [44] which defines turbulent flow to occur at approximately Re=2300, one can make the argument that the inlet of the flow may still be considered well within the laminar region. In order to implement this into the k-ω model the transported variables k and ω are set to be very small at the inlet (1×10^{-30}) since zero cannot be set as a division by zero would not be recognized by the solver. With this setup then the Reynold number of the steady-state of the flow was determined as is shown in figure 4.7.

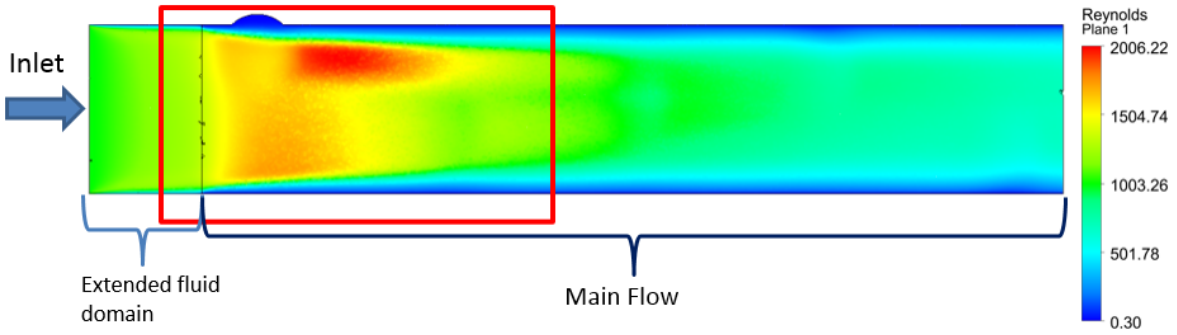

Figure 4.7: Development of Reynolds number inside one of the fins after steady-state is reached in the flow.

As predicted from the estimate the Reynolds number at the inlet suggests that the flow is initially laminar at the inlet of the fluid domain. Once in the fin and especially at the location in close proximity to the first perforation a large jump in the Reynolds number is seen reaching a maximum value of about 2000 immediately downstream of the perforation. The value of Reynolds number here is now high enough to consider the flow as being in the transition from laminar to turbulent.

Transition models

The modelling of transition using RANS models is not directly possible usually an additional model is applied to replicate the transition. One such model is the *Gamma Theta* model, this model makes use of experimental correlations and is formulated as two transport equations. Use of the model can be seen in the work by Abdollahzadeh et al. [1] which compares various low-Re RANS models including a few with the transition model such as the Gamma model for the case of a convective heat transfer analysis for the flow over a flat plate. Here it was concluded that while for solely natural convection the original $k - \epsilon$ models provide a better prediction. In the case of mixed and forced convection where more variables affect the flow, transition models provided much better agreement with the experimental results. While transition models have been proven rigorously against simple geometry and/or flows in the works by Menter and Langtry [34], Langtry [29] and Langtry and Menter [30]. The use of these models for more complex, non-periodic geometry such as for perforated fins where it becomes more difficult to specify some of the variables required by the transition model such as momentum thickness and where transition to turbulence is expected to occur. Due to the perforations the boundary layer is constantly disrupted thus defining a constant momentum thickness as well as defining where specifically transitions occurs is not possible.

LES wall-adaptive local eddy viscosity model

Alternatively to implementing a transition model the use of a large-eddy simulation (LES) was opted for specifically the wall-adapted local eddy-viscosity (WALE) model derived in the work on subgrid-scale

modelling by Nicoud and Ducros [38]. This is classified as an algebraic model such as the well known Smagorinsky model from Smagorinsky [48] which models the eddy viscosity using the Smagorinsky constant that varies depending on the type of flow and mesh resolution. Furthermore a damping function for the eddy viscosity is applied when close to the wall to ensure that the eddy viscosity is zero at the wall. The key advantage of the WALE model is that through its definition of the eddy viscosity it ensures that the eddy viscosity will always be zero at the wall and it can do so without the addition of a damping function. Since the damping function in the Smagorinsky model is an exponential function of the distance from the wall it can be easily implemented in the case of simple geometry but becomes more difficult to define when dealing with complex geometry. The fact that it can ensure almost no eddy viscosity is produced for wall-bounded flows enables the turbulent diffusion to be negligible. This allows the development of linearly unstable waves and thus the transition from laminar to turbulent can somewhat be reproduced[38]. Additionally by using a highly refined numerical grid an attempt will be made to solve most of the flow rather than rely on the modelled subgrid-stress thus approaching a direct numerical simulation (DNS). The disadvantage of LES is the aforementioned requirement of a very fine mesh resolution. Additionally to this the transient effect resolved are particularly sensitive to the selected time step. Thus in order to ensure that all transient effects are resolved the Courant–Friedrichs–Lewy condition must be satisfied, this in combination with the fine mesh results in a time step of order $1 \times 10^{-5} s$. With such a small time-step the temperature development in the metal body will take too long to be determined.

To proceed then instead of carrying out the CHT simulation with the LES model it was deemed more constructive to only simulate the fluid domain using a constant wall temperature. Heat flux is then compared to the RANS model in order to see how large the effect of the transition from laminar to turbulent will impact the heat transfer. The boundary conditions of the LES and RANS simulation are exactly the same the only difference is the spatial discritisation scheme selected and can be seen in tables F.1 and F.2 respectively found in the appendix. While for the RANS a second-order upwind scheme is used for the LES model the central differencing convection scheme was selected since this it is recommended due to this scheme being less dissipative [4].
In order to compare a LES which is transient in nature and delivers instantaneous data to a RANS simulation that is by definition time-averaged one must take a time-average of the data from the LES. Before any statistics are taken the flow must be converged as well as having traversed the flow domain a few times. Lastly in order to determine if the flow was statistically stationary two probes were placed in the flow domain to monitor velocity. The instantaneous velocities are presented in figures 4.8a and 4.8a.

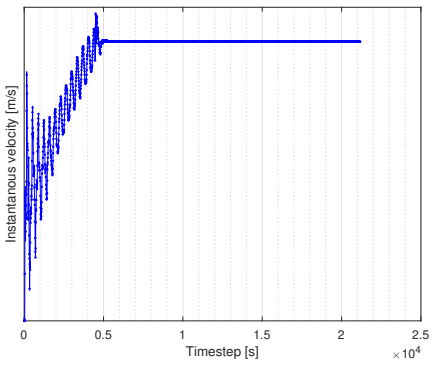

(a) Instantaneous velocity at Probe 1

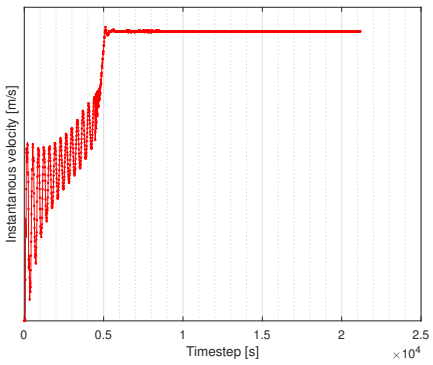

(b) Instantaneous velocity at Probe 2

Once the instantaneous velocity reached a constant value the LES was considered statistically stationary and the averaging of the temperatures and wall heat flux commenced.
Before comparing the LES simulation to the RANS model the extent of the resolution of the LES must be known. As described in the chapter on theoretical background, a LES may vary in quality depending on the mesh used in the discritisation To find how much is simulated and how much is modelled via the sub grid stresses one must calculate the kinetic energy that is simulated based on the filtered Navier-Stokes equations and the kinetic energy based on the residual motions from the sub grid model. Figures 4.9a and 4.9b show the filtered kinetic energy, simulated from the filtered Navier-Stokes equation and the

residual kinetic energy obtained from the sub grid model.

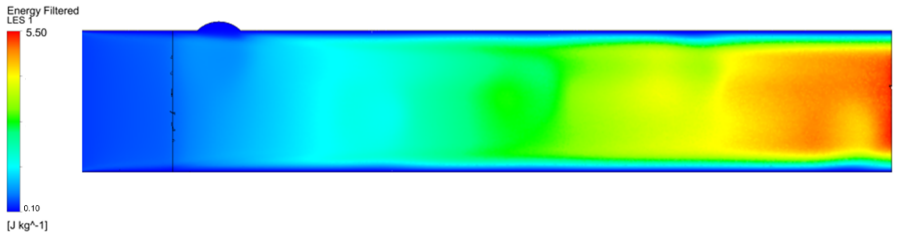

(a) Simulated, filtered kinetic energy in one fin channel after 0.17s.

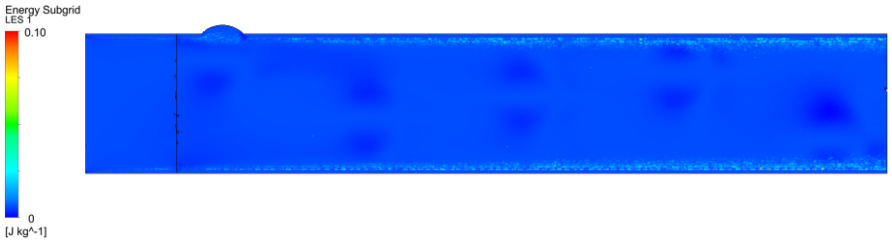

(b) Residual kinetic energy in one fin channel after 0.17s from subgrid model.

Figure 4.9: Comparison of kinetic energy obtained from the filtered Navier-Stokes equations and from the subgrid model.

From figure 4.9 it becomes evident that the majority of the energy is simulated, in order to quantify specifically the portion of simulated to modelled one can calculate the ratio of filtered kinetic energy to total kinetic energy as in equation 4.1.

$$\frac{k_{filtered}}{k_{filtered} + k_{residual}} \tag{4.1}$$

Where

- $k_{filtered} = \frac{1}{2}[\overline{u_i}][\overline{u_j}]$: Is the kinetic energy of the filtered velocity field.
- $k_{residual} = \frac{1}{2}[\overline{u_i u_j}] - \frac{1}{2}[\overline{u_i}][\overline{u_j}]$: Is the residual kinetic energy from the subgrid model.

Applying these definitions to equation 4.1 indicates that the proportion of filtered kinetic energy lays in the region of 98%. This suggests that almost all of the kinetic energy in the flow is simulated thus the LES is said to be approaching a direct numerical simulation (DNS) . The $y^+ < 1$ criteria in every location in the flow as can be seen in figure 4.10.

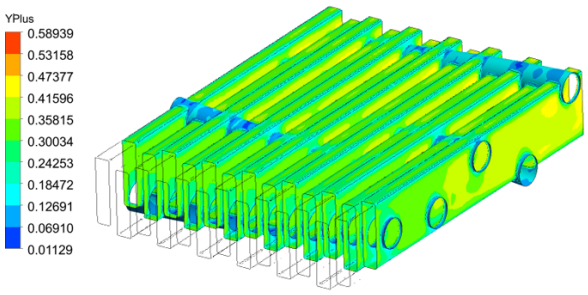

Figure 4.10: Contour plot of y^+ at the wall of the fluid domain.

The time averaged wall heat flux from the LES was compared to the wall heat flux from the RANS simulation in order to determine to what extent the transition from laminar to turbulence which is picked up by the LES has an impact on the heat transfer. The contour plots seen in figures 4.11a and 4.11b show the wall heat flux of the fluid domain.

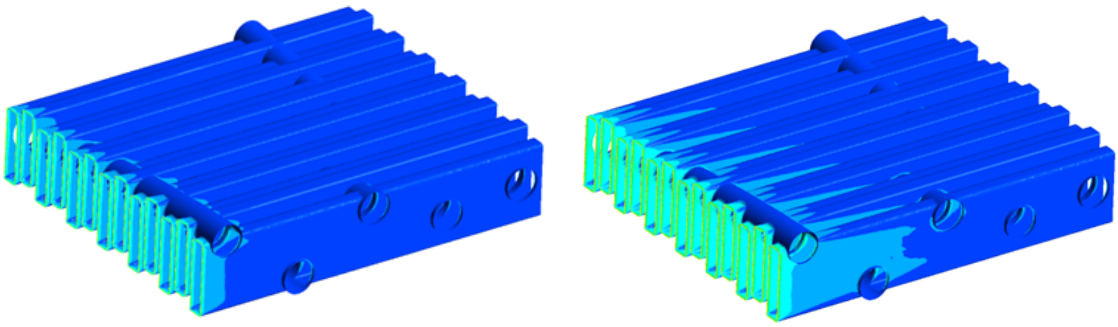

(a) LES after 0.17s ***(b)*** RANS ($k - \omega$ model).

Figure 4.11: Comparison of wall heat fluxes from LES and RANS.

Calculating the area integral of the wall heat flux for the wall of the entire fluid domain and comparing the two simulations gave a difference of approximately 5.2% with the RANS simulation slightly overestimating the heat transfer. Due to the significantly smaller time steps required to solve using LES a conjugate heat transfer simulation will not be feasible as heat flux through the metal occurs at time scales much greater to that of the fluid. Instead the RANS simulation which can be run at greater time steps will be used despite the small differences likely to occur by neglecting the transitional effects.

4.4. Results and Discussions

Proceeding with the unsteady Reynolda-averaged (URANS) model the full CHT simulation was run including the solid domain. This section shall present the results of this. Areas of interest include the velocity and variation of the thermo-physical properties of the flow as well as an understanding of the local heat transfer coefficients.

4.4.1. Flow features

To begin with the flow features within the fin will be looked at, the effect of the perforations on the flow are of particular interest here. The aim of the perforations are to encourage turbulent mixing in order to disrupt boundary layer growth so that heat transfer is maximised. These disruptions in the velocity field are best exemplified in figures 4.12 which shows the cross section of a few of the fin channels, including the perforation.

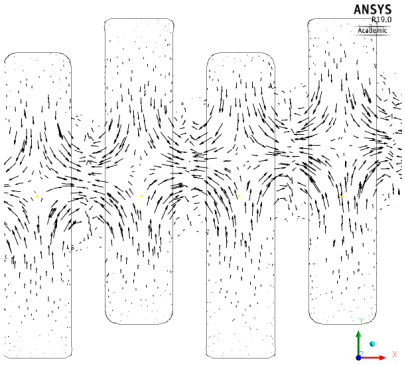

(a) Vector plot x-component of velocity.

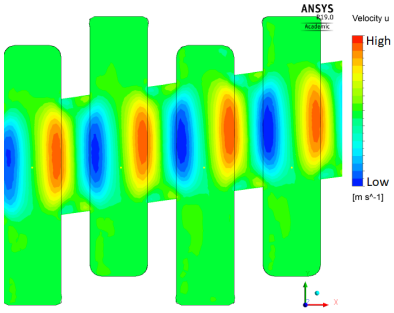

(b) Contours plot x-component of velocity.

Figure 4.12: Flow features near the fin perforations.

The vector plot in figure 4.12a indicates the cross flow that occurs in the perforations of the fin wall. The arrows of the vector plot show a fraction of the fluid being directed to the perforations. The contour plots of the transverse velocity components as seen in figure 4.12b shows how the fluid from the adjacent fin channels essentially cancel each other out and end up recirculating at the perforation rather than transferring from one channel to the other. This recirculation causes a deceleration of the flow in the streamwise (z-direction) which is also reflected in the velocity plot in figure 4.13

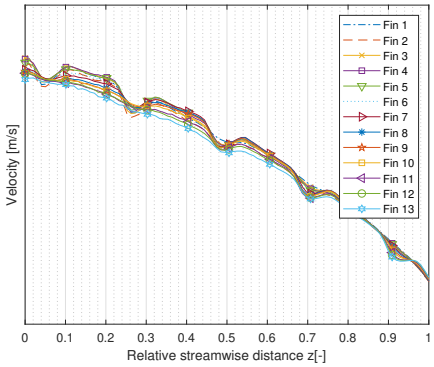

(a) Streamwise velocities at each fin channel after 5s.

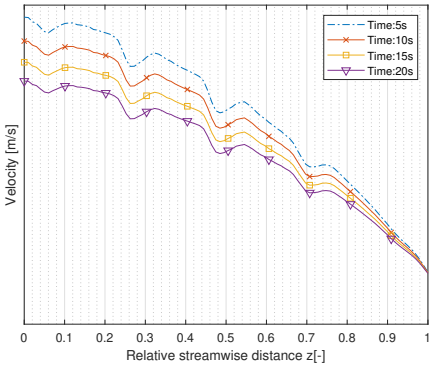

(b) Transient streamwise velocity in fin channel 6.

Figure 4.13: Streamwise velocity, fin channels as labelled in figure 4.14a.

The effect of the perforations is reflected also in the temperature profile through the fins. Figure 4.14a shows the flow in all the fin channels. From this one can already see significant variations in

the different fin channels confirming that the temperature is far from symmetric. To the right in figure 4.14b one of the channels was tracked in time and over the 20s simulated the streamwise temperature is seen to drop steadily as the cold flow traverses the channel. The asymmetry in the temperature is highlighted again in figure 4.15. Comparing temperatures in fin channels 1 and 13 in figure 4.15a one can see that after the perforations in fin 13 the cold temperature has evolved further in contrast to fin 1 which is somewhat warmer. Temperatures are taken across the red line in figure 4.15a and displayed graphically in figure 4.15b which shows the maximum temperature difference being between fin channel 1 and 13 and this being in the range of approximately 20K. The difference decreases to about 5K towards the end of the domain. This suggests that if the flow domain were to be extended, then hypothetically the transverse temperature maldistribution would disappear. However close to the inlet it nevertheless plays a significant role.

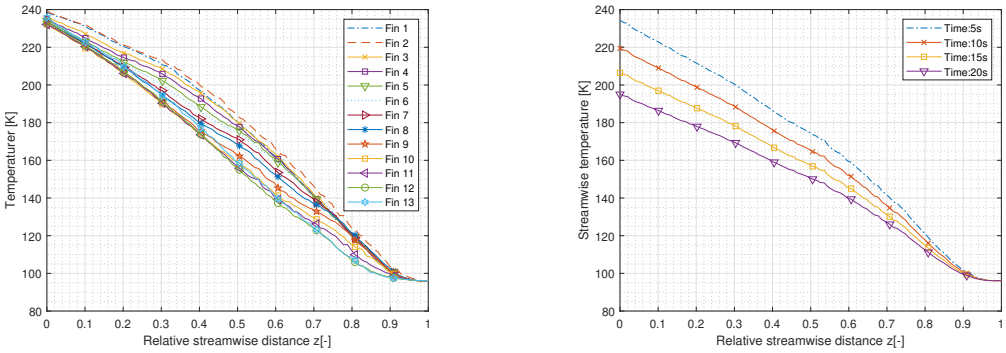

(a) Streamwise temperature in for different fin channels.

(b) Transient temperature in fin channel 6 over 20s.

Figure 4.14: Transverse velocity contours and vector plots.

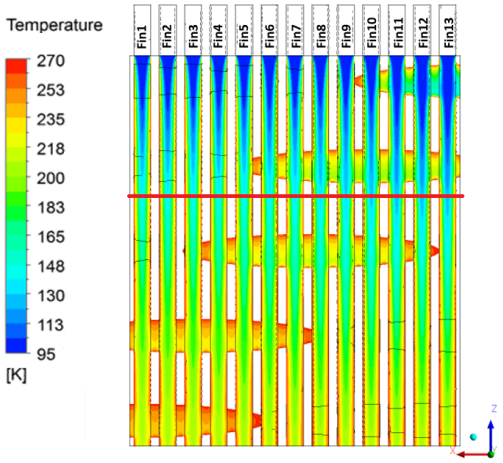

(a) Temperature contours for fin channels.

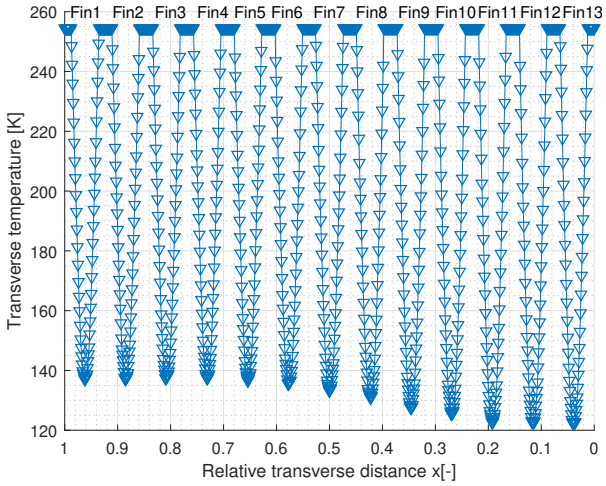

(b) Temperature variation in fin channels, taken across red line from figure 4.15a.

Figure 4.15: Temperature differences in neighbouring fin channels after 20s

4.4.2. Local heat transfer coefficients

The main purpose of a fully resolved geometric simulation of the perforated fins is to better understand the local heat transfer phenomena that take place between the fluid and solid domains. A key property that describes this is the heat transfer coefficient (HTC). In industry an average HTC is generally determined experimentally and assumed globally. This part will present how the heat transfer coefficient has been defined and was determined locally. The HTC has been defined in the theoretical section from Newton's law of cooling in equation 2.3. How the temperature difference is defined will obviously play a significant role in what value for the heat transfer coefficient is determined. While the CFD tool allows for heat transfer coefficients to be determined locally care should be taken as to how this is done. The HTC determined in CFX by default uses the definition as in equation 4.2.

$$h_{c,CFX} = \frac{q_w}{T_w - T_{nw}} \tag{4.2}$$

In which q_w is the wall heat flux, T_w is the solid wall temperature at the fluid-solid interface and T_{nw} is what is termed the near-wall temperature, this is determined from the fluid element adjacent to the solid wall. This definition of the HTC will not accurately describe the heat transfer for internal flows such as this. An alternative definition used in pipe flow replaces the T_{nw} term with the *bulk* temperature of the flow (T_b). The bulk temperature is a convenient way to define a reference temperature in internal flows and is based on what Mills [36] defines as the *adiabatic mixing temperature*. This is the temperature the fluid would attain at a given axial location if it were diverted into an adiabatic mixing chamber and thoroughly mixed. In mathematical terms the bulk temperature is defined in equation 4.3 for flow in pipes.

$$T_b = \frac{\int_0^R \rho c_p u T 2\pi r dr}{\int_0^R \rho c_p u 2\pi r dr} \tag{4.3}$$

Where *u*, *T* and *R* are flow velocity, temperature and pipe radius. Equation 4.3 describes the bulk temperature as the ratio of rate of flow of enthalpy to the rate of flow of heat capacity.

Due to the large variation in axial temperature as seen in appendix H within each of the fin channels it is important to select a sufficient number of surfaces in order to determine a bulk temperature that is representative of the flow domain. 10 surfaces were selected which can be seen in the appendix G of this work in figure G.1. Ultimately with the defined bulk temperature of the flow the local heat transfer coefficients were determined. Figure 4.16 is a contour plot of the fin wall showing the local variations of the heat transfer coefficient.

The contour plots in figure 4.16b and 4.16c are able to show off rather well the sudden jumps in the heat transfer coefficient in close proximity to the perforations. Confirming that the turbulence induced by this geometric feature does impact the overall heat transfer performance of the fins. Not only does one see an increase directly at the perforation but downstream of the holes one can continue to observe the increase in the heat transfer coefficient.

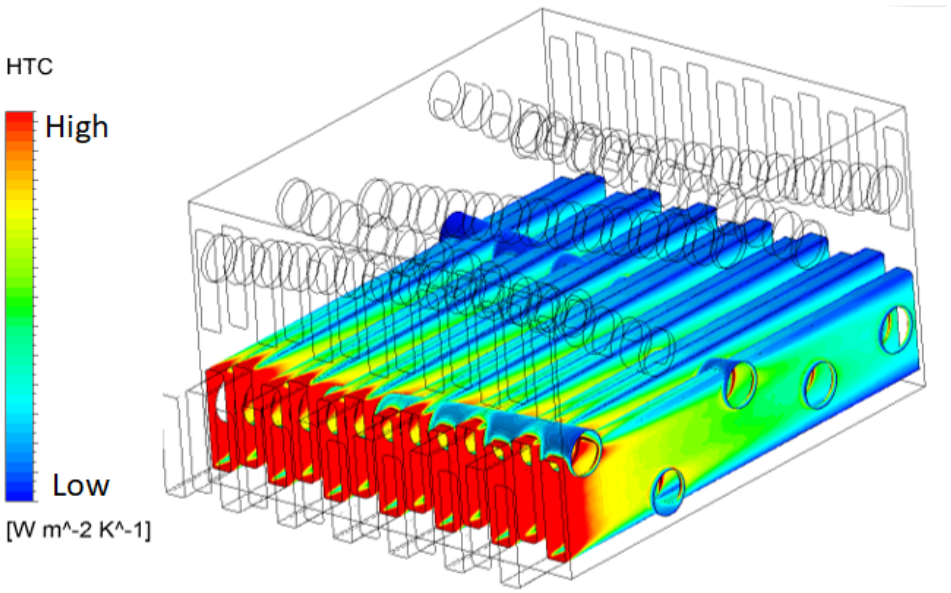

(a) HTC full geometry

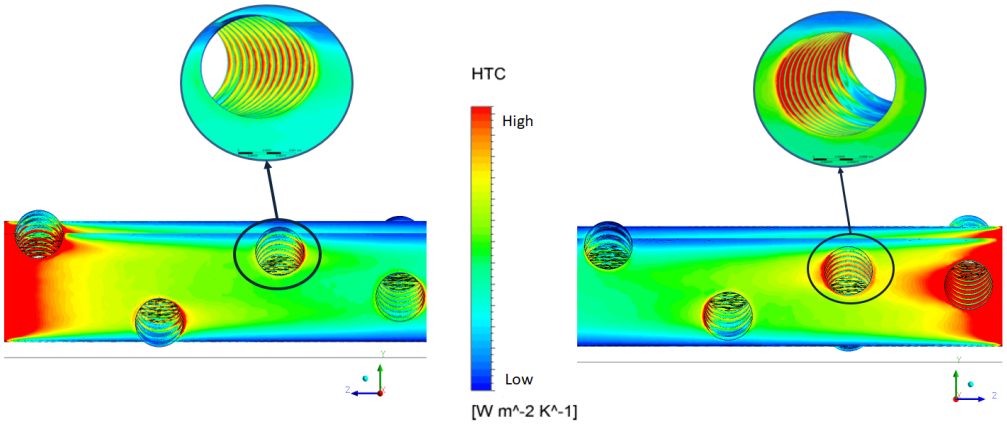

(b) HTC at the wall of Fin 1.

(c) HTC at the wall of fin 13.

Figure 4.16: Local heat transfer coefficients at fluid solid interface of perforated fin geometry.

5

Conclusions and Further Work

The realization of a process plant that can be operated in synchronization with sustainable, and currently available energy sources is truly an undertaking of vast proportion. In an effort to achieve this goal the present work has conducted an in-depth study of the transient operation of a PFHE that reflects a test-rig which is set to undergo fatigue failure testing under transient, thermal loading. The challenges faced were threefold, in order to simulate the large scale geometry a solution had to be devised in which the detailed fin geometry can somehow be represented as a simplified geometry. Secondly the core of this work was the development of a workflow that combines CFD and FEM through a one-way coupling. Thus a data transfer step to enable the one-way FSI simulation by transferring temperature data not just onto a surface mesh but for an entire volume from CFD to a CSM mesh was devised. Lastly for understanding the local heat transfer phenomena a detailed geometry and mesh sufficiently fine had to be produced in order to capture the local effects of a fluid flow.

5.1. Conclusions

This first section shall attempt to answer some of the research questions posed at the outset of this endeavour.

Regarding the large scale geometry

- *To what extent can porous media be used to reflect thermohydraulic phenomena of detailed geometry?*

The comparison of the porous medium in the test case to the analytical method produced very good agreement, with an error of just under 3% in the calculated duty for the two cases. While this discovery is certainly encouraging further validation against a controlled experimental run could further convince of the use of this approach.

- *To what extent can 3-D temperatures be mapped onto a FEM mesh in a one-way FSI simulation framework?*

The main objective of this project was the formulation of a workflow that combines CFD and CSM and in that respect it was successful. The data mapped onto the CSM mesh was in very good agreement with the original temperature profile from the CFD simulation. Maximum temperature differences of less than 1K occur only at a handful of nodes out of the millions present.

- *What are the deformations and locations of the peak stresses?*

The extremely low temperatures at the inlet cause the two modules to contract causing the modules to move independently from one another resulting in the shearing motion between the two blocks. Thus

elevated stresses occur near the module connections.

Regarding the Fin submodel

- *What is the impact of the perforated geometry on the fluid flow?*

The perforations cause some decelerations in the fluid flow, resulting in a drop of just over 10%. Moreover recirculation regions at the location of the perforations are present as a fraction of the streamwise flow moves out of the fin channel through the holes.

- *To what extent is the temperature profile symmetric across the fin channels?*

Due to the wavy path of the perforations some fin channels experienced significantly different temperatures than others. With maximum differences being about 20K. This in turn has significant impact on the material properties of the fluid, specifically the density and therefore the velocity as well.

- *What are the local heat transfer coefficients?*

Locally the heat transfer coefficients appear to vary wildly, with the perforations playing a significant role in this. HTC's are more than double in close proximity to the perforations.

- *What role can CFD play in the development of correlations for different fin type?*

The simulated Colburn and Fanning friction factors show poor to decent agreement with the experimental data depending on what Reynolds number is investigated. This holds up with much of what is found in the literature concerning this area. This technique could seriously be considered to gain a rough first estimate of the thermohydraulic performance of fins without having to go through the effort of manufacturing the fins and setting up complicated experimental rigs. Undoubtedly this would be useful for examining experimental fin geometry. Nevertheless experimental work must undoubtedly continue to be used in order to formulate more accurate correlations defining the heat transfer and momentum for the fins.

5.2. Outlook and Further Work

As the project progressed and most noticeably towards the final stages various areas of interests where identified that were slightly outside of the overall scope of the assignment at hand but should definitely be followed up.

To begin with the large scale model: This project has served as a proof of concept having two purposes. The first and broader one being a feasibility study of one-way FSI computations which have numerous applications in industry. Secondly the accuracy of recreating a complex fin geometry using porous media. In keeping with this the conclusions and recommended further works drawn up here serve as a summary of issues observed during the FSI part of the project and an eye towards the future regarding the porous media model. Recommendations based on the latter point are made with the assumptions of broad validity based on the inability to compare results with actual experimentation.

Beginning with the FSI component of the assignment: The procedure of the data mapping process is a tedious one consisting of a lot of migration of raw data via manually copy and pasting. The use of commercial tools has made it rather difficult to automate the process which the author undoubtedly believes could be done easily with more modifiable open-source software.

The main bottlenecks in the computation are twofold one of which is the extraction of the CFD data which must be in a separate file before the data can be mapped. This process was not able to be parallelized onto multiple cores and if too many timesteps needed to be extracted the post processor runs into memory issues and kill the task. The biggest bottleneck is easily attributed to the structural solver with the mapping of temperatures and running of single timesteps taking up almost the same amount of time as the CFD solver needed to compute 1000s. The main reason for this are the computational limitations due to the fact that the CSM solver is far more memory intensive and as a result had to be run on machines with more memory but far fewer CPUs than what the CFD solver was running on. Thus in order to streamline computational time, trying different solvers which may be less demanding in terms of memory is recommended.

Moving on to the porous media fin model: The natural progression of this model is the incorporation of multiple fin types as opposed to assuming the same fin everywhere as was done in this work. Taking this idea further one could for instance include distribution fins which re-direct the flow. This could be represented by a porous body through the implementation of directional pressure losses specified such that the flow direction could be artificially controlled.

PFHEs in general may operate under two-phase conditions with evaporation and condensation occurring regularly throughout the equipment. To this end implementation of multiphase physics could be incorporated into the solver in tandem with the porous media so that further information can be gleamed on flow maldistribution and heat transfer.

As for the fin submodel: Although some decent results where obtained the agreement to the experimental correlations are heavily influenced by the Reynolds number, the effect of which was underestimated prior to the simulation. The author recommends to investigate flows strictly in the laminar regime to begin with and to incorporate other fin types. Specifically starting from plain fins which provide the most basic geometry out of all the fins and complexities introduced by the perforated or serrated fins such as cross flow from one fin channel to the other can be eliminated. Moreover in order to gain better agreement for the Fanning friction factors the computational domain of the flow downstream should be extended to obtain a better idea of the pressure loss over the length of the fin.

A

Method of Virtual Work for Cantilever Beam

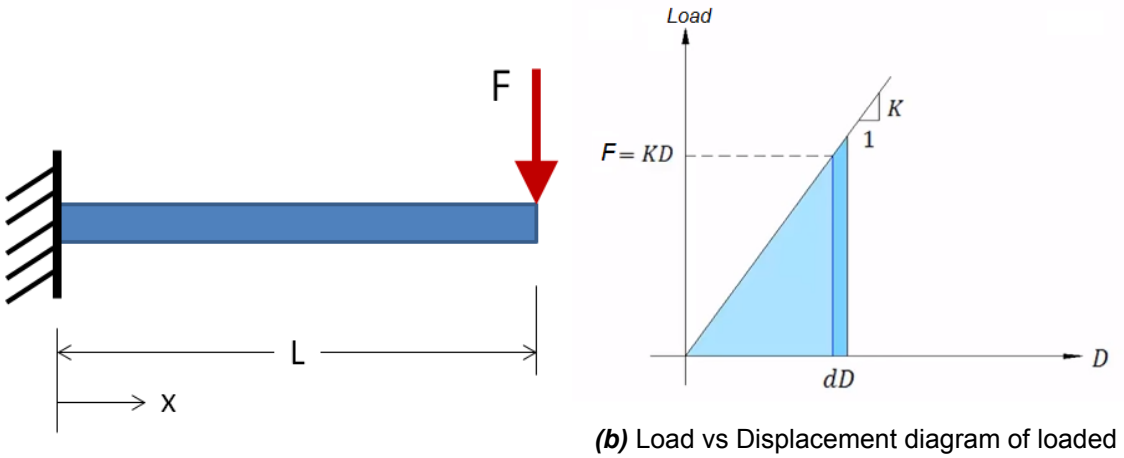

(a) Cantilever beam loaded with force F.

(b) Load vs Displacement diagram of loaded cantilever beam.

Figure A.1: Loaded Cantilever beam and associated load vs displacement diagram.

The loading diagram associated with this particular loading of the beam can be seen in A.1b where K is the stiffness which is assumed to be linear and D is the displacement. The work done onto this system is then defined be the integral equation A.1.

$$W = \int_0^D K D d D \tag{A.1}$$

Alternatively from figure A.1b one can define this as the area under the graph which is shaded in blue by the expression A.2.

$$W = \frac{F D}{2} \tag{A.2}$$

In finite element analysis one begins by determining the displacement of individual nodes that make up the element, unfortunately through the use of the energy principle applied to the cantilever beam in figure A.1a the displacement only at the location where the load is applied may be determined. Thus it stands to reason that in order to determine the displacement at a location of interest one must apply a further load to that location. This application of a virtual load to determine a real displacement is the fundamental thinking behind the principle of virtual work.

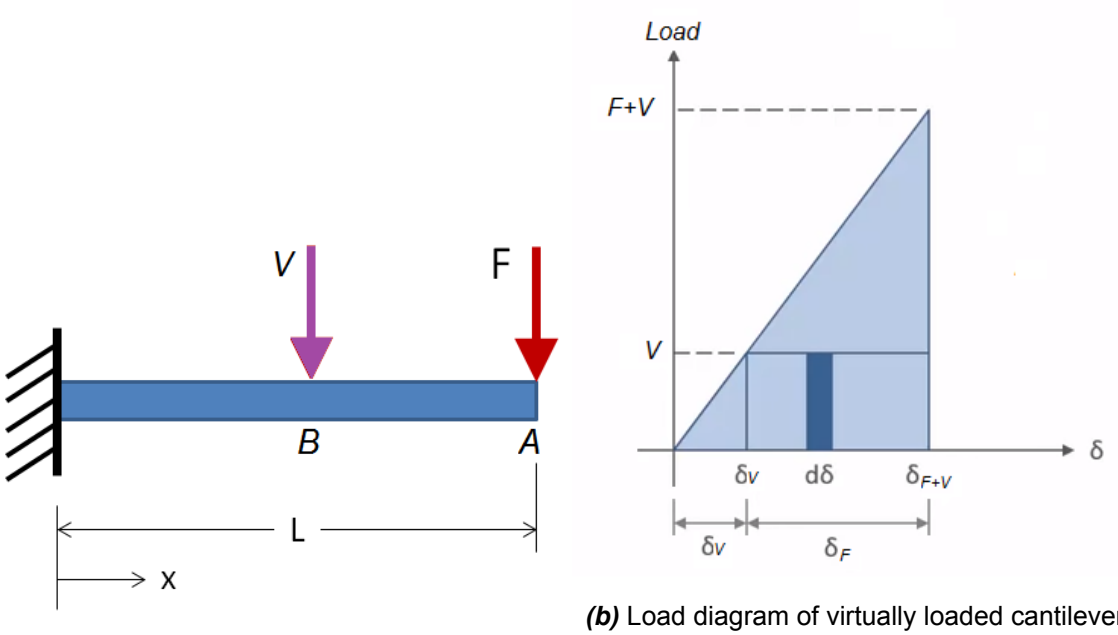

(a) Cantilever beam with applied virtual load.

(b) Load diagram of virtually loaded cantilever beam.

Figure A.2: Virtually loaded cantilever beam with associated load diagram

The load V in figure A.2a represents such a virtual load placed at an arbitrary location along the beam where the deflection is desired. The virtual load applied must however be admissible. Knothe and Wessels [27] describe an admissible virtual load as one that causes a displacement that is geometrically possible i.e. that fulfils the geometric boundary conditions. Referring now to the load diagram in figure A.2b considering the small segment $d\delta$ the following must hold.

$$dW_{External} = V\,d\delta \tag{A.3}$$

Integrating yields

$$W_{External} = \int_{\delta_V}^{\delta_{V+F}} V\,d\delta = V\,\delta_F \tag{A.4}$$

Notice that the factor $\frac{1}{2}$ is no longer present since the integration now occurs for an infinitesimal segment $d\delta$ as explained by Link [33]. In conclusion then for the cantilever beam the following statements are true.

$$W_{External\,Real} = \frac{F\delta_A}{2} \tag{A.5}$$

and

$$W_{External\,Virtual} = V\delta_B \tag{A.6}$$

Similarly for the internal moments in the beam due to the real and virtual external loads applied one can write

$$dW_{Internal\,Real} = \frac{M\,d\theta}{2} \tag{A.7}$$

and

$$dW_{Internal\,Virtual} = m\,d\theta \tag{A.8}$$

integrating along the entire length of the beam and defining the change in angle as $d\theta = \frac{M}{EI}dx$ yields.

$$W_{InternalReal} = \int_0^L \frac{1}{2} M \left(\frac{M}{EI} dx \right) \tag{A.9}$$

And

$$W_{InternalVirtual} = \int_0^L m \left(\frac{M}{EI} dx \right) \tag{A.10}$$

Where *M* and *m* are the moments due to the real and virtual load respectively. Notice again that the factor $\frac{1}{2}$ is absent in the virtual internal work expression. The conservation of energy for the cantilever beam is defined in equation A.11.

$$\underbrace{\int_0^L \frac{1}{2} M \left(\frac{M}{EI} dx \right)}_{W_{InternalReal}} + \underbrace{\int_0^L m \left(\frac{M}{EI} dx \right)}_{W_{InternalVirtual}} = \underbrace{\frac{1}{2} F \delta_A}_{W_{ExternalReal}} + \underbrace{V \delta_B}_{W_{ExternalVirtual}} \tag{A.11}$$

For the conservation of energy to hold for the real internal and external energy they must be equal to one another and thus can be stricken from equation A.11 and therefore leaving.

$$\underbrace{\int_0^L m \left(\frac{M}{EI} dx \right)}_{W_{InternalVirtual}} = \underbrace{V \delta_B}_{W_{ExternalVirtual}} \tag{A.12}$$

Finally recalling that the virtual load *V* is not actually applied and takes an arbitrary value usually a unit load of 1 then equation A.12 simplifies to

$$\underbrace{\delta_B}_{\text{Displacement at location B}} = \underbrace{\int_0^L m \left(\frac{M}{EI} dx \right)}_{W_{InternalVirtual}} \tag{A.13}$$

and thus A.13 provides an expression for the displacement at the desired location along the beam

B

Data Transfer and Mapping

Paramount to any FSI simulation endeavour is the transfer of data from meshes that are often dissimilar. This transfer of data is referred to as *mapping* and can be done in numerous ways with each algorithm either more or less appropriate for a specific applications. This section aims to give a brief overview of the mapping procedure and indicate which methods where used in this work.
The settings to facilitate the transfer of data from source to target mesh are broadly defined in three categories: *mapping*, *weighting* and *transfer type* each of which will be explained in more detail.

Mapping
ANSYS, which was the tool used provide two algorithms that concern mapping control.

- *Profile Preserving*

The profile preserving mapping takes the profile of the variable of interest from the source mesh and then matches it to the target mesh as best it can.

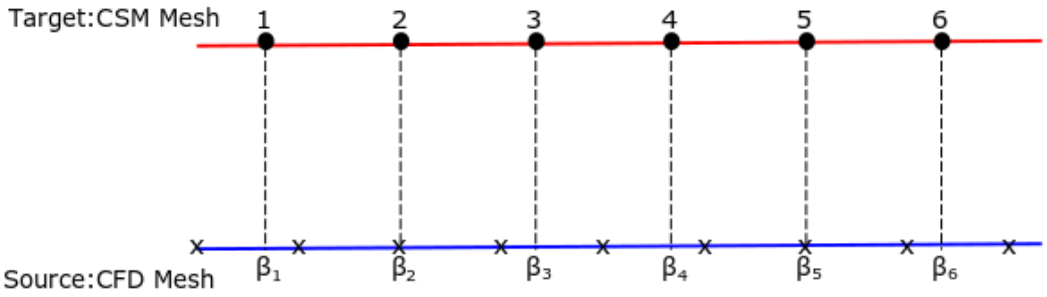

Figure B.1: Schematic of data mapping using profile preserving method.

Figure B.1 represents the mapping procedure from the source mesh (CFD) to the target mesh (CSM). The target mesh nodes represented by the circles are mapped onto the source mesh elements, a weighting calculation is then done at β_i locations on the source side. The value to be transferred is then generally described as $T_1 = \omega(\beta_i)$. Where ω is some weighting function.

- *Conservative*

As the name suggests the conservative mapping ensures that the profile being transferred is interpolated in such a way as to ensure that the quantity passing across the interface is conserved. For instance say a force is transferred, the conservative mapping will ensure that the total force passing out of one mesh is equal to that going into the other mesh.

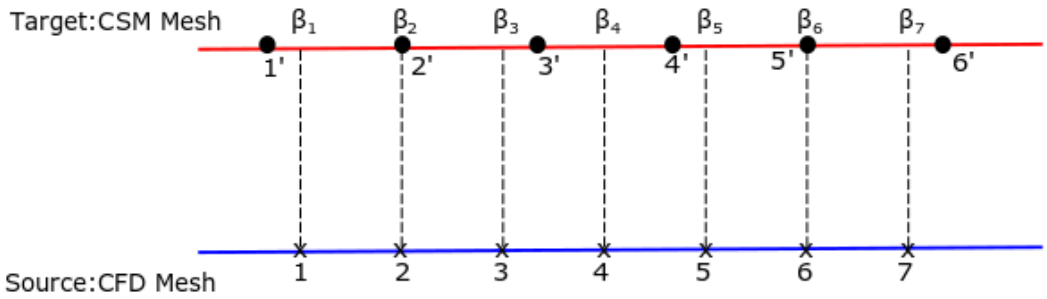

Figure B.2: Schematic of data mapping using conservative method.

Figure B.2 is a schematic of the conservative mapping method. Conversely to the profile preserving method, here the nodes of the source mesh (X) are mapped to the target mesh elements. This results in the source data being divided into two quantities. This is well demonstrated when looking at source node 4, which is split to the target nodes 3' and 4'.

Out of these options the profile preserving mapping was selected the main reason for this is simply that the conservative mapping only makes sense if the profile in question is a physical quantity that can be conserved, such as force or heat flux. Since the variable in question is temperature conservative mapping does not apply.

Weighting

Since the mapping often occurs for dissimilar meshes the weighting functions will dictate how the data is allocated to the target nodes. For this there exist three options: *Triangulation*, *distance based average* and *kriging* each of which are briefly explained next.

- *Triangulation*

For 3D mapping as done in here, the triangulation method creates temporary 3D, 4-node tetrahedrons from the closest source nodes in order to find points that will contribute portions of their data values. Elements are created by iterating over all possible combinations of the source points, starting with the closest points. For all target points found within the element weights are calculated based on the target's location inside the element Ansys [3].

- *Distance based average*

Uses the distance from the target node to the source node(s) to determine a weighting value.

- *Kriging*

Kriging is a regression-based interpolation technique that assigns weights to the surrounding source points according to their spatial covariance values. The algorithm combines the kriging model and a polynomial model to capture global deviations. The interpolation then occurs based on the local deviations Ansys [3].

The triangulation method provided a good compromise between accuracy and computational cost and was thus the method selected.

Transfer type

This is the final option that needs to be defined and concerns the dimension of the data transfer. When using the triangulation method as the weighting option there are two options available.

- *Surface*

In the surface method the target points are mapped by searching for triangles which were formed using the closest source points. The target point is projected onto the plane relative to the triangle. If the target point is located within the triangle weights are calculated based on the target's projected location within the triangle.

- *Volumetric*

In the volumetric method the target point is mapped by searching for the tetrahedrons that were created based on the closest source points. Weights are again calculated based on the target points location within the tetrahedron.

Since the nature of this work required data to be mapped between volumes the latter method was implemented.

C

Boundary Conditions for Validation Case

Table C.1: Boundary conditions and numerical setup for test case used in mesh convergence study and model validation.

Location	***Boundary Condition***	***Value***	***Units***
Cold Inlet (Fluid)	Velocity-Inlet	1	m/s
	Temperature-Inlet	280	K
Hot Inlet (Fluid)	Velocity-Inlet	1	m/s
	Temperature-Inlet	380	K
Cold Outlet (Fluid)	Pressure-Outlet	0	Pa
Hot Outlet (Fluid)	Pressure-Outlet	0	Pa
Cold Flow Wall (Fluid)	Porous – Solid Interface	Conservative Heat Flux	W/m^2
Hot Flow Wall (Fluid)	Porous – Solid Interface	Conservative Heat Flux	W/m^2
Outer Parting Plate Surfaces	Wall	Adiabatic	[-]
Inner Parting Plate Surfaces	Solid – Porous Interface	Conservative Heat Flux	W/m^2
	Solid – Solid Interface	Conservative Heat Flux	W/m^2
Outer Side Bar Surfaces	Wall	Adiabatic	[-]
Inner Side Bar Surfaces	Solid – Porous Interface	Conservative Heat Flux	W/m^2
	Solid – Solid Interface	Conservative Heat Flux	W/m^2
	Numerical Model		
Porous Domain	Porosity	0.75	[-]
	Interfacial Area Density	1500	$1/m$
	Linear Drag Coefficient	200	kg/m^2s
	Quadratic Drag Coefficient	70	kg/m^4
	Heat Transfer Coefficient	76	W/m^2K
Turbulence Model	Laminar (none)		
Solver	Pressure Based		
Spatial Discritization	Second Order Upwind		
Pressure-Velocity Coupling	Coupled		

D

Boundary Conditions for Large Scale Geometry

Table D.1: Boundary conditions and numerical setup for full large scale PFHE geometry

Location	***Boundary Condition***	***Value***	***Units***
Cold Inlet (Fluid)	Velocity-Inlet	From Mass Flow	m/s
	Temperature-Inlet	96.15	K
Cold Outlet (Fluid)	Pressure-Outlet	0	Pa
Cold Flow Wall (Fluid)	Porous-Solid Interface	Conservative Heat Flux	W/m^2
Hot Inlet (Solid)	Wall	Adiabatic	[-]
Hot Outlet (Solid)	Wall	Adiabatic	[-]
Hot Flow Wall (Solid)	Solid – Solid Interface	Conservative Heat Flux	W/m^2
Outer Parting Plate Surfaces	Wall	Adiabatic	[-]
Inner Parting Plate Surfaces	Solid – Porous Interface	Conservative Heat Flux	W/m^2
	Solid – Solid Interface	Conservative Heat Flux	W/m^2
Outer Side Bar Surfaces	Wall	Adiabatic	[-]
Inner Side Bar Surfaces	Solid – Porous Interface	Conservative Heat Flux	W/m^2
	Solid – Solid Interface	Conservative Heat Flux	W/m^2
Outer Cover Plate	Wall	Adiabatic	[-]
Inner Cover Plate	Solid - Solid Interface	Conservative Heat Flux	W/m^2
Module Connector	Solid – Solid Interface	Conservative Heat Flux	W/m^2
	Numerical Model		
Porous Domain	Porosity	0.75	[-]
	Interfacial Area Density	1500	$1/m$
	Linear Drag Coefficient	200	kg/m^2s
	Quadratic Drag Coefficient	70	kg/m^4
	Heat Transfer Coefficient	From Colburn factor	W/m^2K
Turbulence Model	Laminar (none)		
Equation of State	Redlich-Kwong (As defined in CFX)		
Solver	Pressure Based		
Spatial Discritization	Second Order Upwind		
Temporal Discritisation	Backward Euler		
Pressure-Velocity Coupling	Coupled		

E

Additional Results: Large Scale Model

E.1. Fluid vs Fin Temperatures

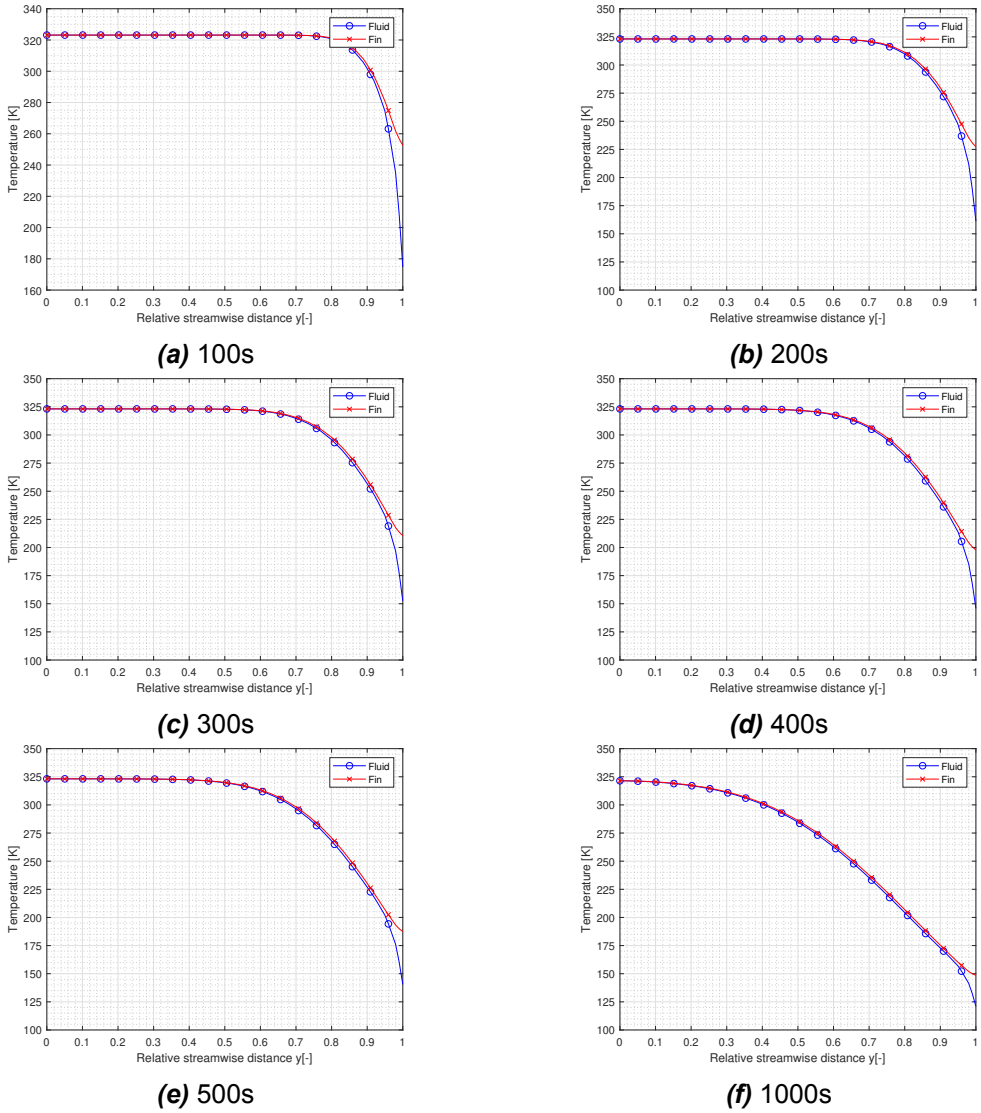

(a) 100s

(b) 200s

(c) 300s

(d) 400s

(e) 500s

(f) 1000s

Figure E.1: Observed temperature difference between fin and fluid.

E.2. Parting Plate Comparison

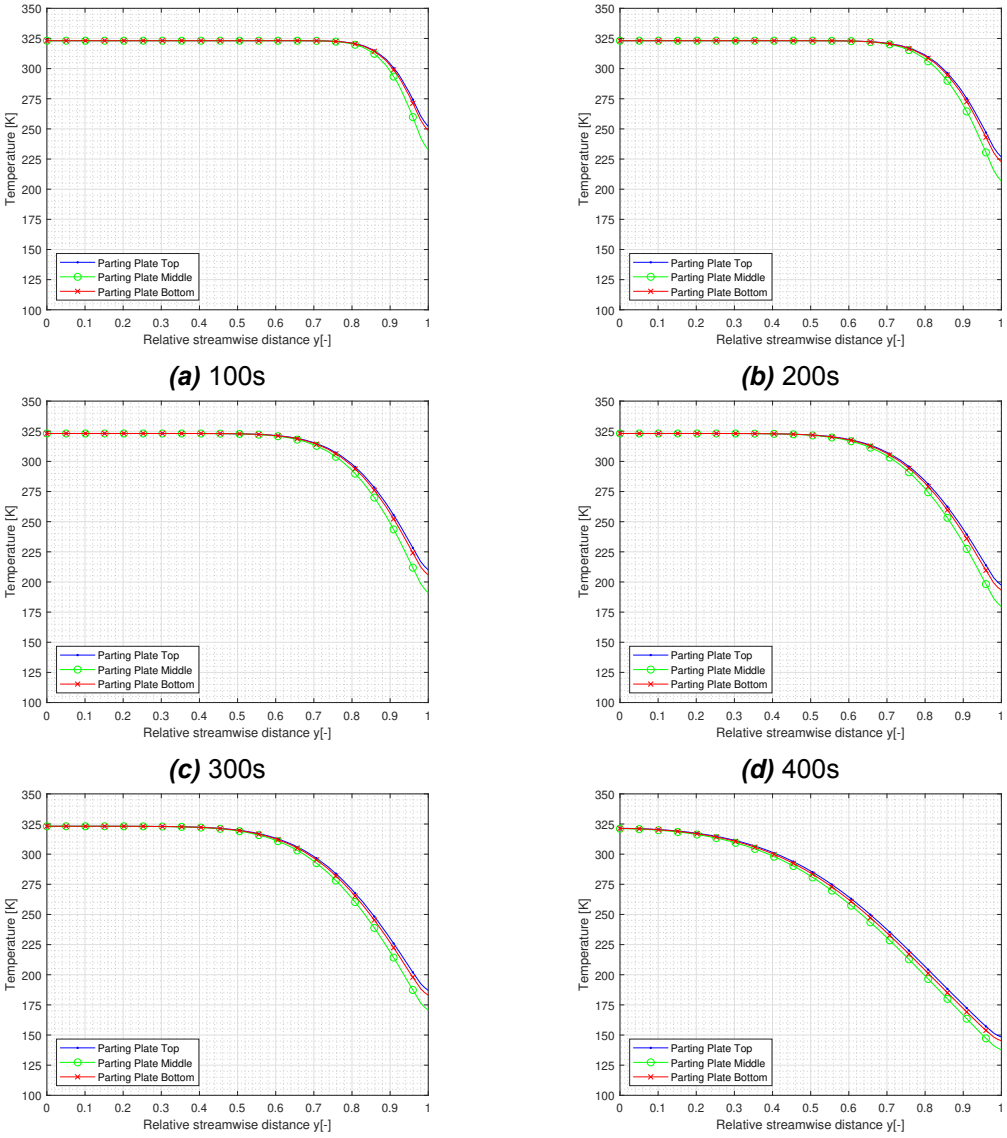

(a) 100s ***(b)*** 200s

(c) 300s ***(d)*** 400s

(e) 500s ***(f)*** 1000s

Figure E.2: Observed temperature difference between parting plates at different locations in the heat exchanger block.

E.3. Transverse Temperatures

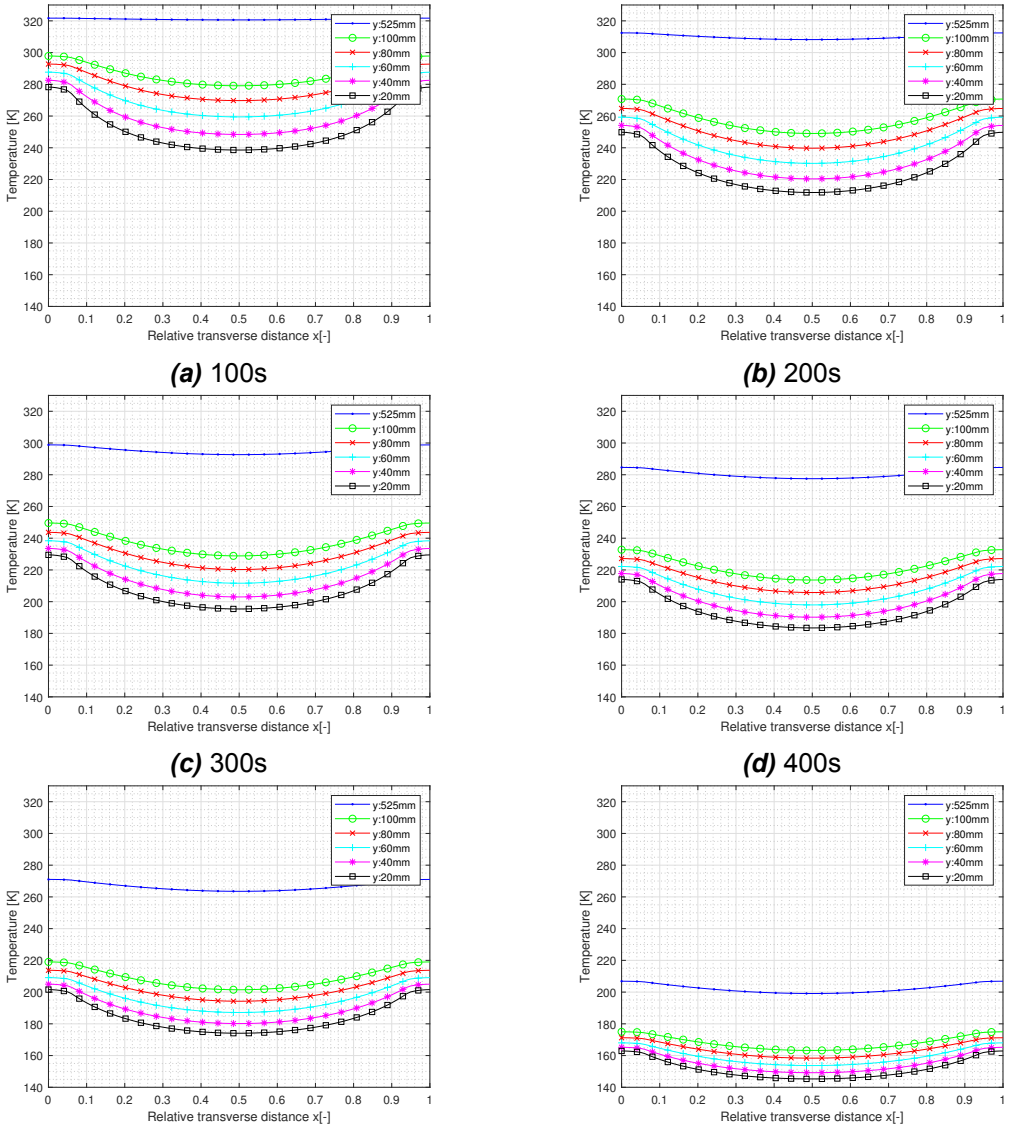

(a) 100s

(b) 200s

(c) 300s

(d) 400s

(e) 500s

(f) 1000s

Figure E.3: Transverse temperatures at varying streamwise locations in PFHE block. The vertical line represents where the sidebars begin.

F

Boundary Conditions Submodel

F.1. LES Model

Table F.1: Boundary conditions and numerical setup of LES.

Location	***Boundary Condition***	***Value***	***Units***
Cold Inlet (Fluid)	Velocity-Inlet	From Mass Flow	m/s
	Temperature-Inlet	96.15	K
Cold Outlet (Fluid)	Pressure-Outlet	0	Pa
Cold Flow Wall (Fluid)	Wall	No-slip (Dirichlet)	m/s
		Temperature 323.15	K
Numerical Model			
Turbulence Model	LES: Wall adapted local eddy viscosity (WALE) model		
Equation of State	Redlich-Kwong (As defined in CFX)		
Solver	Pressure Based		
Spatial Discritization	Central Difference		
Temporal Discritization	Backward Euler		
Pressure-Velocity Coupling	Coupled		

F.2. RANS Model

Table F.2: Boundary conditions and numerical setup for RANS simulation.

Location	***Boundary Condition***	***Value***	***Units***
Cold Inlet (Fluid)	Velocity-Inlet	From Mass Flow	m/s
	Temperature-Inlet	96.15	K
Cold Outlet (Fluid)	Pressure-Outlet	0	Pa
Cold Flow Wall (Fluid)	Wall	No-slip (Dirichlet): 0 Temperature: 323.15	m/s K
	Numerical Model		
Turbulence Model	k-omega model		
Equation of State	Redlich-Kwong (As defined in CFX)		
Solver	Pressure Based		
Spatial Discritization	Second Order Upwind		
Temporal Discritization	Backward Euler		
Pressure-Velocity Coupling	Coupled		

F.3. CHT Submodel

Table F.3: Boundary conditions and numerical setup for CHT submodel.

Location	***Boundary Condition***	***Value***	***Units***
Cold Inlet (Fluid)	Velocity-Inlet	From Mass Flow	m/s
	Temperature-Inlet	96.15	K
Cold Outlet (Fluid)	Pressure-Outlet	0	Pa
Cold Flow Wall (Fluid)	Fluid – Solid Interface	No-slip (Dirichlet): 0	m/s
		Conservative Heat Flux	W/m^2
Inner Fin Surface (Solid)	Solid – Fluid Interface	Conservative Heat Flux	W/m^2
Outer Fin Surface (Solid)	Solid –Solid Interface	Conservative Heat Flux	W/m^2
Top Parting Plate Surface	Solid – Solid Interface	Thermal Periodic	W/m^2
Bottom Parting Plate Surface	Solid – Solid Interface	Thermal Periodic	W/m^2
Side + Front + Back Plates Surfaces	Wall	Adiabatic	[-]
	Numerical Model		
Turbulence Model	k-omega model		
Equation of State	Redlich-Kwong (As defined in CFX)		
Solver	Pressure Based		
Spatial Discritization	Second Order Upwind		
Temporal Discritization	Backward Euler		
Pressure-Velocity Coupling	Coupled		

G

Bulk Temperature Surfaces

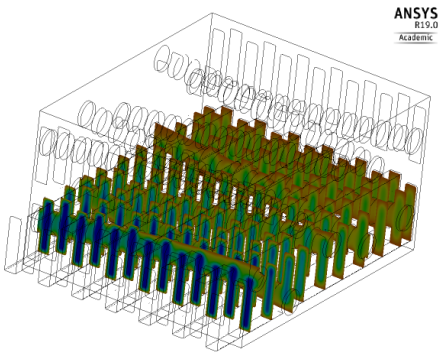

(a) Cross flow temperature planes

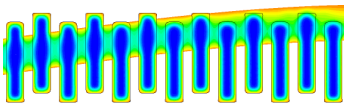

(b) Cross-section 1

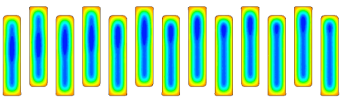

(c) Cross-section 2

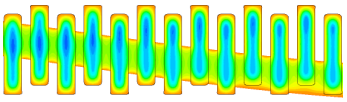

(d) Cross-section 3

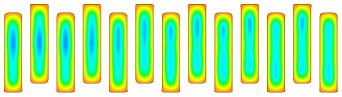

(e) Cross-section 4

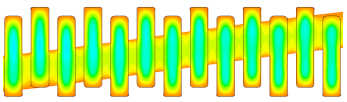

(f) Cross-section 5

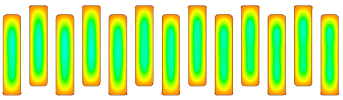

(g) Cross-section 6

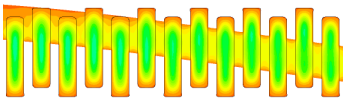

(h) Cross-section 7

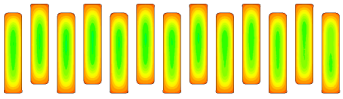

(i) Cross-section 8

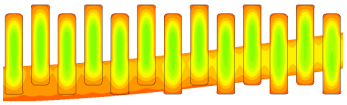

(j) Cross-section 9

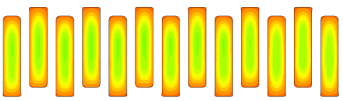

(k) Cross-section 10

Figure G.1: Temperature contours at 10 cross-sections in the flow domain

Bibliography

[1] M. Abdollahzadeh, M. Esmaeilpour, R. Vizinho, A. Younesi, and J. C. Pàscoa. Assessment of RANS turbulence models for numerical study of laminar-turbulent transition in convection heat transfer. *International Journal of Heat and Mass Transfer*, 115:1288–1308, 2017. ISSN 00179310. doi: 10.1016/j.ijheatmasstransfer.2017.08.114. URL https://doi.org/10.1016/j.ijheatmasstransfer.2017.08.114.

[2] ALPEMA. *The Standards of the Brazed Aluminium Plate-Fin Heat Exchanger Manufacturers ' Association*. Number February. The Brazed Aluminium Plate-Fin Heat Exchanger Manufacturers' Association (ALPEMA), 2010. URL www.alpema.org.

[3] Ansys. ANSYS Elements Reference, 2007.

[4] ANSYS Inc. *ANSYS Manual*. ANSYS.Inc., Canonsburg, 2007.

[5] Christophe Bailly. *Turbulence*. Springer, Lyon, 1st edition, 2015. ISBN 9783319161594. doi: 10.1007/978-3-319-16160-0.

[6] H. Bhowmik and Kwan Soo Lee. Analysis of heat transfer and pressure drop characteristics in an offset strip fin heat exchanger. *International Communications in Heat and Mass Transfer*, 36 (3):259–263, 2009. ISSN 07351933. doi: 10.1016/j.icheatmasstransfer.2008.11.001. URL http://dx.doi.org/10.1016/j.icheatmasstransfer.2008.11.001.

[7] BMBF. Kopernikus-Projekt SynErgie, . URL https://www.kopernikus-projekte.de/projekte/industrieprozesse.

[8] BMBF. Kopernikus-Projekte für die Energiewende, . URL https://www.kopernikus-projekte.de/start.

[9] Allan Bower. *Applied Mechanics of Solids*. CRC Press, Boca Raton, 1st edition, 2009. ISBN 9781439802472.

[10] Hans Joachim Bungartz, Florian Lindner, Bernhard Gatzhammer, Miriam Mehl, Klaudius Scheufele, Alexander Shukaev, and Benjamin Uekermann. preCICE – A fully parallel library for multi-physics surface coupling. *Computers and Fluids*, 141:250–258, 2016. ISSN 00457930. doi: 10.1016/j.compfluid.2016.04.003. URL http://dx.doi.org/10.1016/j.compfluid.2016.04.003.

[11] Barbaros Cetin and Mehmet Aksel. Simulation of Thermal Characteristics of Radiators using a Porous Model. In *Proceedings of CONV-14:Int. Symp. on Convection Heat and Mass Transfer*, number June, Kusadasi, 2014. Int. Symp. on Convection Heat and Mass Transfer. doi: 10.13140/2.1.4853.0566.

[12] Tao Chen, Jie Wang, and Wei Peng. Flow and heat transfer analyses of a plate-fin heat exchanger in an HTGR. *Annals of Nuclear Energy*, 108:316–328, 2017. ISSN 18732100. doi: 10.1016/j.anucene.2017.05.008. URL http://dx.doi.org/10.1016/j.anucene.2017.05.008.

[13] Rene de Borst, Mike Crisfield, Joris Remmers, and Clemens Verhoosel. *Non-Linear Finite Element Analsyis of Solids and Structures*. John Wiley & Sons Inc, West Sussex, 2nd edition, 2012. ISBN 9780470666449.

[14] Yu Du. *Numerical Simulation Of Mechanical and Thermal Fluid–Structure Interaction in Labyrinth Seals*. PhD thesis, Technnische Universität Darmstadt, 2010.

[15] A. Eken and M. Sahin. The Numerical Simulation of Large-Scale Fluid-Structure Interaction Problems in A Fully Coupled Form. In *10th World Congress on Computational Mechanics*, number May 2014, pages 2559–2577, Istanbul, 2014. doi: 10.5151/meceng-wccm2012-18908. URL http://www.proceedings.blucher.com.br/article-details/9181.

[16] Fraunhofer Institute for Algorithms and Scienti c Computing SCAI. MpCCI CouplingEnvironment, 2011.

[17] P Freko, I Thomas, R Hölzl, A Lehmacher, and A Woitalka. Optimization of lifetime expectance for heat exchangers with special requirements. In *Proceedings of the 15th International Heat Transfer Conference, IHTC 2014*, pages 1–11, Kyoto, 2014. URL https://www.scopus.com/inward/record.uri?eid=2-s2.0-84964478773{&}partnerID=40{&}md5=251a0b433923c3f0dc0aee24be440472.

[18] Patrick Haider, Pascal Freko, Stefan Lochner, Thomas Reiter, and Harald Klein. Design of a test rig for the simulation of startup procedures in main heat exchangers of air separation plants. *Chemical engineering transactions*, 69, 2018.

[19] Gerhard A. Holzapfel. *Nonlinear Solid Mechanics: A Continuum Approach for Engineering*. John Wiley & Sons, West Sussex, 1st edition, 2000. ISBN 9780471823193. doi: 10.1023/A:1020843529530. URL http://eu.wiley.com/WileyCDA/WileyTitle/productCd-0471823198.html.

[20] Reinhold Hölzl. Processes for Determining the Strength of Plate-Type Heat Exchanger, for Producing a Plate-Type Heat Exchanger, and for Producing a Process Engineering System, 2010.

[21] Reinhold Hölzl and Rainer Flüggen. Experimental Fatigue Evaluation of Aluminum Brazed Plate Fin Heat Exchangers. In *ASME 2013 Pressure Vessels and Piping Conference*, Paris, 2013. ASME.

[22] Reinhold Hölzl, Thomas Hecht, and Pascal Freko. Damage Analysis and Fatigue Evaluation of an Aluminium Brazed Plate Fin Heat Exchanger. In *Proceedings of the ASME 2014 Pressure Vessels & Piping Division Conference*, Anaheim, 2014. ASME.

[23] Junling Hu and Xingguo Xiong. Modeling of a Counter Flow Plate Fin Heat Exchanger. In *Proceedings of the 2014 COMSOL Conference in Boston*, number November, Boston, 2014.

[24] Frank P. Incropera, David P. DeWitt, Theodore L. Bergman, and Adrienne S. Lavine. *Fundamentals of Heat and Mass Transfer*. John Wiley & Sons, Inc., Danvers, 6th edition, 2007. ISBN 9780471457282. doi: 10.1073/pnas.0703993104. URL http://www.google.com/patents?hl=en{&}lr={&}vid=USPAT5328671{&}id=rb8lAAAAEBAJ{&}oi=fnd{&}dq=Heat+and+Mass+Transfer{&}printsec=abstract{%}5Cnhttp://www.google.com/patents?hl=en{&}lr={&}vid=USPAT5328671{&}id=rb8lAAAAEBAJ{&}oi=fnd{&}dq=Heat+and+mass+transfer{&}printsec=abstract{%}5Cnh.

[25] Morteza Khoshvaght-Aliabadi. Thermal performance of plate-fin heat exchanger using passive techniques: vortex-generator and nanofluid. *Heat and Mass Transfer/Waerme- und Stoffuebertragung*, 52(4):819–828, 2015. ISSN 14321181. doi: 10.1007/s00231-015-1603-6.

[26] Sun Hye Kim, Jae Boong Choi, Jung Soon Park, Young Hwan Choi, and Jin Ho Lee. A coupled CFD-FEM analysis on the safety injection piping subjected to thermal stratification. *Nuclear Engineering and Technology*, 45(2):237–248, 2013. ISSN 2234358X. doi: 10.5516/NET.09.2012.038. URL http://dx.doi.org/10.5516/NET.09.2012.038.

[27] K Knothe and H Wessels. *Finite Elemente*. Springer, Berlin, 1st edition, 1991. ISBN 3-540-53696-5.

[28] Pijush Kundu, Ira Cohen, and David Dowling. *Fluid Mechanics*. Academic Press, Amsterdam, 6th edition, 2015. ISBN 9780124059351.

[29] R. B. Langtry. Transition Modeling for General CFD Applications in Aeronautics. *American Institute of Aeronautics and Astronautics*, 21(3):437–465, 2005. ISSN 18607349. doi: 10.1515/text.2001.007.

[30] R. B. Langtry and F. R. Menter. A Correlation-Based Transition Model Using Local Variables: Part II — Test Cases and Industrial Applications. *Volume 4: Turbo Expo 2004*, (July):69–79, 2004. ISSN 0889504X. doi: 10.1115/GT2004-53454. URL http://proceedings.asmedigitalcollection.asme.org/proceeding.aspx?articleid=1638720.

[31] Ming-Jian Li, Jun-Hua Pan, Ming-Jiu Ni, and Nian-Mei Zhang. Heat transfer and thermal stress analysis in fluid-structure coupled field. *Applied Thermal Engineering*, 88:473–479, 2015. ISSN 13594311. doi: 10.1016/j.applthermaleng.2014.09.071. URL http://linkinghub.elsevier.com/retrieve/pii/S1359431114008436.

[32] Linde. Brochure on Aluminium Plate-Fin Heat Exchangers, 2008.

[33] M Link. *Finite Elemente in der Statik und Dynamik*. B. G. Teubner, Stuttgart, 2nd edition, 1989. ISBN 3-519-12953-1.

[34] F. R. Menter and R. B. Langtry. A Correlation-Based Transition Model Using Local Variables—Part I: Model Formulation. *Journal of Turbomachinery*, 128(3):413, 2006. ISSN 0889504X. doi: 10.1115/1.2184352. URL http://turbomachinery.asmedigitalcollection.asme.org/article.aspx?articleid=1467239.

[35] Pablo Mosquera Michaelsen. *A fluid-structure-interaction and simulation tool for application in rotating machinery*. PhD thesis, Karlsruher Institute für Technologie, 2015.

[36] A Mills. *Basic Heat and Mass Transfer*. Pearson Education Limited, Essex, 2nd edition, 2014. ISBN 10: 1-29204248-6.

[37] F Moukalled, L Mangani, and M Darwish. *The Finite Volume Method in Computational Fluid Dynamics - An Advanced Introduction with OpenFOAM and Matlab*, volume M. Springer, Heidelberg, 1st edition, 2016. ISBN 9783319168739. doi: DOI10.1007/978-3-319-16874-6.

[38] F Nicoud and F Ducros. Subgrid-Scale Stress Modelling Based on the Square of the Velocity Gradient Tensor. *Flow, Turbulence and Combustion*, 62(3):183–200, 1999. ISSN 00219991. doi: 10.1016/j.jcp.2004.10.018.

[39] Donald a Nield and Adrian Bejan. *Convection in Porous Media*, volume 24. Springer Science+Business Media, Inc., New York, 3rd edition, 2006. ISBN 9780387290966. URL http://www.springerlink.com/content/x30210/{#}section=471823{&}page=1.

[40] Frans T M Nieuwstadt, Bendiks J Boersma, and Jerry Westerweel. *Turbulence: Introduction to Theory and Applications of Turbulent Flows*. Springer, Delft, 1st edition, 2016. ISBN 9783319315973. doi: 10.1007/978-3-319-31599-7.

[41] J Pei, H Dohmen, S Yuan, and F Benra. Investigation of unsteady flow-induced impeller oscillations of a single-blade pump under off-design conditions. *Journal of Fluids and Structures*, 35: 89–104, 2012.

[42] Stephen B Pope. *Turbulent Flows*, volume 12. Cambridge University Press, New York, 1st edition, 2000. ISBN 9780511840531. doi: 10.1088/0957-0233/12/11/705. URL http://stacks.iop.org/0957-0233/12/i=11/a=705?key=crossref.71804963fd6eca6048b82cb2b9527350.

[43] H Richard and M Sander. *Ermüdungsrisse*. Springer Vieweg, Wiesbaden, 3rd edition, 2012. ISBN 978-3-658-00086-8. doi: 10.1007/978-3-658-00087-5.

[44] H Schlichting and K Gersten. *Grenzschicht-Theorie*. Springer, Berlin, 9th edition, 1997. ISBN 3-540-55744-x 9.

[45] X Schuler, E Laurien, R Kulenovic, and M Kuschewski. Thermal fatigue : Fluid-structure interaction at thermal mixing events. In *38th MPA-Seminar*, number 1, pages 82–105, Stuttgart, 2012.

[46] D Seader and Ernest J Henley. *Separation Process Principles*, volume 1. John Wiley & Sons Inc, Hoboken, 2nd edition, 2006. ISBN 0470481838. doi: 10.5860/CHOICE.36-5112.

[47] L. Sheik Ismail, C. Ranganayakulu, and Ramesh K. Shah. Numerical study of flow patterns of compact plate-fin heat exchangers and generation of design data for offset and wavy fins. *International Journal of Heat and Mass Transfer*, 52(17-18):3972–3983, 2009. ISSN 00179310. doi: 10.1016/j.ijheatmasstransfer.2009.03.026. URL http://dx.doi.org/10.1016/j.ijheatmasstransfer.2009.03.026.

[48] J Smagorinsky. Smagorinsky_1963_General_circulation_experiments_with_the_primitive_equations. *Monthly Weather Review*, 91(3):99–164, 1963. ISSN 0027-0644. doi: 10.1175/1520-0493(1963)091<0099:GCEWTP>2.3.CO;2.

[49] Morel Thierry, Florent Duchaine, Anthony Thévenin, Andrea Piacentini, Moritz Kirmse, and Eric Quémerais. Open-PALM coupler version 4.1.4 User guide and training manual, 2013. URL http://www.cerfacs.fr/globc/PALM{_}WEB/pdfs/user{_}guide.pdf.

[50] Gavin Towler and Ray Sinnott. *Chemcial Engineering Design*. Elsvier, Oxford, 5th edition, 2009. ISBN 9780080966595.

[51] B Uekermann and Hj Bungartz. A parallel, black-box coupling algorithm for fluid-structure interaction. In *International Conference on Computational Methods for Coupled Problems in Science and Engineering*, pages 1–12, München, 2013. ISBN 9788494140761. URL http://congress.cimne.com/coupled2013/proceedings/full/p559.pdf.

[52] Milton Van Dyke. *An Album of Fluid Motion*. The Parabolic Press, San Mateo, 4th edition, 1982.

[53] W Wagner. *Wärmeaustauscher*. Vogel Industrie Medien GmbH & Co. KG, Würzburg, 4th edition, 2009. ISBN 978-3-8343-3161-8.

[54] Liang Wang, Chuanxiang Zheng, Shuang Wei, Baicun Wang, and Zongxin Wei. Thermo-mechanical investigation of composite high-pressure hydrogen storage cylinder during fast filling. *International Journal of Hydrogen Energy*, 40(21):6853–6859, 2015. ISSN 03603199. doi: 10.1016/j.ijhydene.2015.04.018. URL http://dx.doi.org/10.1016/j.ijhydene.2015.04.018.

[55] Lin Wang, Robin Quant, and Athanasios Kolios. Fluid structure interaction modelling of horizontal-axis wind turbine blades based on CFD and FEA. *Journal of Wind Engineering and Industrial Aerodynamics*, 158:11–25, 2016. ISSN 01676105. doi: 10.1016/j.jweia.2016.09.006. URL http://dx.doi.org/10.1016/j.jweia.2016.09.006.

[56] Weiping Wang, Jinxing Guo, Shuwen Zhang, Jian Yang, Xianting Ding, and Xuehua Zhan. Numerical study on hydrodynamic characteristics of plate-fin heat exchanger using porous media approach. *Computers and Chemical Engineering*, 61:30–37, 2014. ISSN 00981354. doi: 10.1016/j.compchemeng.2013.10.010. URL http://dx.doi.org/10.1016/j.compchemeng.2013.10.010.

[57] V Widak, P Norajitra, and J Reiser. Helium-Cooled Divertor Development: Thermo Hydraulic and Thermo Mechanical Analysis Studies of a Single Jet Design. *Fusion Science and Technology*, 56: 1028–1032, 2009.

[58] D. Wilcox. Multiscale model for turbulent flows. In D. Wilcox, editor, *24th Aerospace Sciences Meeting*, volume 29, pages 4471–4480, Reston, Virigina, jan 1986. American Institute of Aeronautics and Astronautics. doi: 10.2514/6.1986-29. URL http://arc.aiaa.org/doi/10.2514/6.1986-29.

[59] Alexander Woitalka, Ingo Thomas, Pascal Freko, and Axel Lehmacher. DYNAMIC SIMULATION OF HEAT EXCHANGERS USING Linde's In-House Process Simulator Optisim. In *ICHMT International Symposium on Advances in Computational Heat Transfer*, pages 1–10, Piscataway, 2015.

[60] Huizhu Yang, Jian Wen, Xin Gu, Yuce Liu, Simin Wang, Wenjian Cai, and Yanzhong Li. A mathematical model for flow maldistribution study in a parallel plate-fin heat exchanger. *Applied Thermal Engineering*, 121:462–472, 2017. ISSN 13594311. doi: 10.1016/j.applthermaleng.2017.03.130. URL http://dx.doi.org/10.1016/j.applthermaleng.2017.03.130.

[61] P. Yuan, G. B. Jiang, Y. L. He, and W. Q. Tao. Performance simulation of a two-phase flow distributor for plate-fin heat exchanger. *Applied Thermal Engineering*, 99:1236–1245, 2016. ISSN 13594311. doi: 10.1016/j.applthermaleng.2016.01.096.

[62] Yan Yunju, Xi Zhuyou, and Zhang Shanzhi. Numerical simulation and transonic wind-tunnel test for elastic thin-shell structure considering fluid-structure interaction. *Chinese Journal of Aeronautics*, 28(1):141–151, 2014.

[63] Bing Zhang, Gang Fan, Jian Yang, Chuangui Liu, and Shan Tang. Numerical Analysis of Header Structure Improvement in a Plate-Fin Heat Exchanger. *Chemical Engineering and Technology*, 39 (10):1813–1820, 2016. ISSN 15214125. doi: 10.1002/ceat.201500728.

[64] Lingjie Zhang, Zuoqin Qian, Jun Deng, and Yuting Yin. Fluid–structure interaction numerical simulation of thermal performance and mechanical property on plate-fins heat exchanger. *Heat and Mass Transfer*, 51(5):749–749, 2015. ISSN 0947-7411. doi: 10.1007/s00231-015-1507-5. URL http://link.springer.com/10.1007/s00231-015-1507-5.

[65] Y. Zhang and T. Lu. Unsteady-state thermal stress and thermal deformation analysis for a pressurizer surge line subjected to thermal stratification based on a coupled CFD-FEM method. *Annals of Nuclear Energy*, 108:253–267, 2017. ISSN 18732100. doi: 10.1016/j.anucene.2017.04.034.

[66] Y. Zhang, T. Lu, P. X. Jiang, Y. H. Zhu, J. Wu, and C. L. Liu. Investigation on thermal stratification and turbulent penetration in a pressurizer surge line with an overall out-surge flow. *Annals of Nuclear Energy*, 90:212–233, 2016. ISSN 18732100. doi: 10.1016/j.anucene.2015.12.006.

[67] Xiang Zhao, Yongfeng Zhu, and Sijun Zhang. Transonic wing flutter preditions by a loosely-coupled method. *Computers & Fluids*, 58:45–62, 2012.